UNIVERSIDAD NACIONAL AUTÓNOMA DE MÉXICO

PROGRAMA DE POSGRADO EN ASTROFÍSICA

INSTITUTO DE RADIOASTRONOMÍA Y ASTROFÍSICA

SIMULACIONES MHD DE GALAXIAS MEDUSA

TESIS
PARA OPTAR POR EL GRADO DE
DOCTORA EN CIENCIAS (ASTROFÍSICA)

PRESENTA
MARIANA VIOLETA RAMOS MARTÍNEZ

TUTOR
DR. GILBERTO C. GÓMEZ REYES
INSTITUTO DE RADIOASTRONOMÍA Y ASTROFÍSICA

MORELIA, MICHOACÁN, MAYO 2019

Universidad Nacional Autónoma de México
UNAM
Biblioteca Central
Dirección General de Bibliotecas de la UNAM

UNAM – Dirección General de Bibliotecas
Tesis Digitales
Restricciones de uso

DERECHOS RESERVADOS ©
PROHIBIDA SU REPRODUCCIÓN TOTAL O PARCIAL

Todo el material contenido en esta tesis esta protegido por la Ley Federal del Derecho de Autor (LFDA) de los Estados Unidos Mexicanos (México).

El uso de imágenes, fragmentos de videos, y demás material que sea objeto de protección de los derechos de autor, será exclusivamente para fines educativos e informativos y deberá citar la fuente donde la obtuvo mencionando el autor o autores. Cualquier uso distinto como el lucro, reproducción, edición o modificación, será perseguido y sancionado por el respectivo titular de los Derechos de Autor.

Dedicado a la memoria de mi padre
porque habría disfrutado este momento.

A mi madre
por todo su cariño y dedicación.

Agradecimientos

En primer lugar, quiero expresar mi agradecimiento a mi director de tesis Gilberto C. Gómez por depositar su confianza en mí y permitirme desarrollar el trabajo de investigación que se presenta en esta tesis. Gracias a su dedicación y paciencia pude lograr este trabajo. Agradezco profundamente su apoyo incondicional y compresión durante los momentos más difíciles de mi vida.

A mis padres, Carmen y Mariano, por todo su amor, esfuerzo y sacrificio que me permitieron llegar tan lejos. A mis hermanos, Froyla y Andrés, y sobrinos Maximiliano, Aixa y Santiago por acompañarme en este camino.

A mis tutores Rosa A. González y Stan Kurtz por que su interés y preocupación en el buen desarrollo de este trabajo.

A mis sinodales: Verónica Lora, Jacopo Fritz, Ivânio Puerari, Javier Sánchez y Vicente Rodríguez, ya que sus valiosos comentarios y sugerencias ayudaron a mejorar esta tesis.

A mis amigos y compañeros del IRyA, especialmente a Carolina, Gisela, Antonio, Tere e Iveth, ya que sin su amistad mi estancia en el instituto y en Morelia no habría sido tan placentera y divertida.

Al personal del IRyA por facilitarme mi estancia en el instituto así como por su apoyo y guía para realizar trámites académicos y planificar la asistencia a congresos.

Finalmente, al Consejo Nacional de Ciencia y Tecnología (CONACYT) por el apoyo económico brindado mediante la beca No. 379726 para poder realizar mis estudios de doctorado. Al proyecto PAPIIT IN100916 de UNAM-DGAPA por el apoyo financiero.

Contents

List of Figures

Resumen

Desde la clasificación de galaxias de Hubble, las galaxias lenticulares o S0s han representado una incógnita en los modelos de formación y evolución de galaxias. Dado que las S0s comparten propiedades con las galaxias elípticas (población estelar vieja) y las galaxias espirales (disco estelar en rotación), se ha manejado la idea de que las S0s pudieran haber evolucionado a partir de las galaxias espirales. Desde hace varias décadas se han propuesto diversos mecanismos mediante los cuales una galaxia espiral pudiera transformarse en una S0. Uno de ellos es conocido como "ram pressure stripping" (RPS). El RPS es un proceso en el que una espiral que viaja a través de un cúmulo de galaxias experimenta la presión hidrodinámica del medio intracúmulo (ICM), de manera que esta presión arranca el gas del disco al vencer la gravedad de la galaxia. A través de observaciones en varias longitudes de onda se han logrado observar galaxias en cúmulos que muestran signos de RPS ya que exhiben una distribución de gas asimétrica, es decir, el medio interestelar (ISM) de la galaxia está desplazado con respecto al disco estelar y/o forma una cola de gas. A este tipo de galaxias se les ha denominado "galaxias medusa" ya que frecuentemente presentan largos filamentos brillantes de gas y polvo similares los tentáculos de las medusas marinas. Para entender más sobre la posible evolución de una espiral en una S0 se han realizado una gran variedad de simulaciones con diferentes métodos y técnicas sobre el RPS, incluyendo la inclusión de diversos fenómenos físicos. Sin embargo, poco se ha tomado en cuenta la contribución que pueda tener el campo magnético presente en el disco galáctico, por lo que esta tesis se enfoca a explorar este caso.

El principal objetivo ha sido mostrar el impacto que tiene el campo magnético en la dinámica del gas durante el RPS. Para ello, se realizaron simulaciones magnetohidrodinámicas (MHD) de una galaxia de disco en un túnel de viento para modelar su paso a través del ICM. También se presenta un modelo puramente hidrodinámico (HD), es decir sin campo magnético, para comparar las diferencias entre modelos con y sin campo magnético, lo que ha constituido la primera parte de esta tesis. **Los principales resultados que se obtuvieron aquí son que el campo magnético modifica la dinámica de la interacción del**

gas con el viento del ICM ya que el primero incrementa el grosor del disco galáctico al aumentar la densidad superficial del gas, además de producir un *flaring* en la galaxia, es decir, que el disco se ensancha conforme aumenta el radio galactocéntrico. Este *flaring* genera choques oblícuos cuando el ICM choca contra el disco, produciendo un flujo de gas desde las partes externas de la galaxia hacia el centro durante unos ∼150 Myr. Este movimiento de gas hacia el centro genera la posibilidad de tener material disponible para la formación estelar o actividad nuclear en la galaxia antes de que el ICM termine por remover el gas del disco, lo cual se ha observado en algunas galaxias medusa. Otro efecto que tiene el campo magnético en el RPS es que modifica la estructura y morfología de las colas de gas: en el caso MHD, las colas de gas muestran una estructura suave en forma de filamentos horizontales ya que el gas se desplaza en forma de anillos afuera del disco, mientras que en el HD el gas es comprimido más fácilmente por lo que el gas desplazado tiene forma de grumos y filamentos a lo largo de la dirección del viento.

La segunda parte de la tesis se ha enfocado en modelos MHD variando el ángulo de inclinación del disco con respecto a la dirección del viento del ICM para estudiar los efectos que tiene en la distribución del gas barrido, así como en el campo magnético. Se presentan 4 modelos con ángulos de inclinación (0, 20, 70 y 90º) entre el disco y el viento del ICM. Se encuentra que en discos poco inclinados (0 y 20º) se desarrollan colas de gas más extensas que magnetizan más el ambiente, en contraste con los casos muy inclinados (70 y 90º). Además, en los casos poco inclinados se observa que el gas es desplazado en forma de anillos que, al ser impulsados por el viento cada vez más lejos de la galaxia, se perturban en la dirección de su movimiento formando filamentos que se alinean con el campo magnético. En cambio, en los casos muy inclinados, el campo ligado al gas muestra una estructura elongada, esto es, que se comprime en la parte del disco que choca con el ICM mientras que en el lado opuesto el gas y las líneas del campo se expanden. También se realizaron observaciones sintéticas de estos modelos para obtener mapas de emisión y la dirección de la polarización sincrotrón. La emisión sincrotrón de los modelos está truncada en el disco mientras que en la dirección del viento se extiende siguiendo al gas, similar a algunas galaxias en el cúmulo de Virgo. En el caso de la polarización, se recupera información del campo magnético, ya que los vectores de campo magnético B inferidos mediante la polarización de la emisión sincrotrón trazan de forma correcta la estructura del campo magnético.

Estos resultados muestran la relevancia que tienen los modelos MHD en el proceso de RPS. Además de modificar la dinámica del gas, el campo magnético también abre ventanas de observación que no son accesibles a modelos HD.

Summary

Since the Hubble classification of galaxies, lenticular galaxies or S0s have represented a mystery in the models of formation and evolution of galaxies. Since S0s have common properties with ellipticals (old stellar population) and spirals (rotating stellar disc) it has been proposed that S0s could have evolved from spirals. Over several decades, several mechanisms have been proposed by which a spiral galaxy could be transformed into an S0. One of these mechanisms is known as "ram pressure stripping" (RPS). The RPS is a process in which a spiral travels through a cluster of galaxies and experiences the ram pressure of the intracluster medium (ICM), such that the pressure removes the gas of the disc when it overcomes the gravity of the galaxy. Multiwavelength observations have detected galaxies in clusters that show signs of RPS since they exhibit an asymmetric gas distribution, i.e., the interstellar medium (ISM) of the galaxy is displaced with respect to the stellar disc and/or forms a gas tail. This type of galaxies have been called "jellyfish galaxies", since they frequently present long and bright filaments of gas and dust resembling the tentacles of marine jellyfish. To understand more about the possible evolution of a spiral into an S0, a wide variety of simulations have been performed with different methods and techniques. However, the contribution of the magnetic field present in the galactic disc has hardly been taken into account.

The main goal of this thesis has been to show the impact of the magnetic field in the gas dynamics during the RPS. With this in mind, magnetohydrodynamical (MHD) simulations of a disc galaxy in a wind-tunnel to model its way through the ICM were performed. Also is presented a pure hydrodynamic (HD) model, that is without magnetic field, to compare the differences between models with and without magnetic field, which consists of the first part of this thesis. **The main results obtained here are that the magnetic field modifies the dynamics of the interaction of the gas with the ICM wind since the first one increases the thickness of the galactic disc by increasing the gas surface density, in addition to producing a flaring in the galaxy**, i.e. the disc becomes thicker with increasing the galactocentric radius. The flaring generates oblique shocks when the ICM hits the disc, producing an inflow of gas from the out-

skirts of the galaxy towards the central regions that lasts $\sim 150\,\mathrm{Myr}$. This inward motion of gas raises the possibility of having material for the star formation or to trigger nuclear activity in the galaxy before the ICM removes the gas in the disc, which has been observed in some jellyfish galaxies. Another effect of the magnetic field in the RPS is that it modifies the structure and morphology of the gas tails: in the MHD case, the tails present a smooth structure with horizontal filaments since the gas is displaced in the form of rings outside of the disc, while in the HD case the gas is compressed easier hence the displaced gas is shaped-like clumps and filaments along the wind direction.

The second part of the thesis is focused on MHD models varying the disc inclination angle with respect to the ICM-wind direction to study how the inclination affects the distribution of the swept gas, as well as in the magnetic field. Four models with inclination angles (0, 20, 70 and 90°) between the disc and the ICM wind are presented. It is found that discs with low inclinations (0 and 20°) develop more extended gas tails and magnetize more the environment, contrary to the highly tilted cases (70 and 90°). Additionally, in the low inclination cases it is observed that the gas is swept in the form of rings, and when they are pushed farther away from the galaxy by the wind, the rings are perturbed in the direction of the wind motion forming filaments that line up with the magnetic field. In contrast, in the highly inclined models, the magnetic field bound to the gas shows an elongated structure, i.e., is compressed in the side of the disc that hits the wind while in the downstream side the gas and the magnetic field lines expand. Also, synthetic observations were carried out for these models to obtain maps of the synchrotron emission and the direction of polarization. The synchrotron emission from the models is truncated in the disc while in the direction of the wind it is extended following the gas, similar to some galaxies in the Virgo Cluster. In the case of the polarization, it is recovered the information of the magnetic field, since the magnetic field B vectors inferred from the polarization of the synchrotron emission draw the magnetic field structure correctly.

These results show the importance of the MHD models in the RPS process. In addition to modifying the gas dynamics, the magnetic field opens observation windows that are not available with HD models.

Chapter 1

Introduction

1.1 Galaxy classification and the Hubble sequence

Edwin Hubble proposed to categorize the galaxies in groups according to their optical appareance observed from photographic plates. In his work, Hubble (1926, 1936) classifed the galaxies as ellipticals (E), spirals (S), and lenticulars (S0) in the famously known "Hubble sequence" or "Tuning Fork diagram" (fig. 1.1). Galaxies that would not fit any of the listed criteria were labeled as irregulars (Irr). Throughout the years, this classification scheme has been expanded and modified (de Vaucouleurs 1959; Sandage 1975) but Hubble's system is currently in use by astronomers.

Elliptical galaxies are round, smooth systems with elliptical isophotes, old stellar populations with few young blue stars, low gas and dust content, and lack of rotation, i.e., the stars show more disordered or random motions. These galaxies have the designation En based on their ellipticity: $n = 10e = 10(1 - b/a)$, where b and a are semiminor and semimajor axes, respectively.

Spiral galaxies are composed of a disc and a central bulge and, as its name suggests, they show a spiral pattern of stars, dust and gas. Some spirals show a bar that emerges from its center and for this reason they were subdivided into another class: barred-spirals (SB). Additionally, the spiral galaxies follow a sequence based on the bulge-to-disc ratio, their gas content, and how tightly wound their arms are, going from S(SB)a for galaxies with the tightest arms, lower gas content, and more prominent bulges, to S(SB)c/d galaxies with more open arms, higher gas fraction, and less dominant bulges.

The lenticular galaxies lie between the elliptical and spiral galaxies in the Hubble sequence and consist of a disc and prominent bulge. The S0s share properties

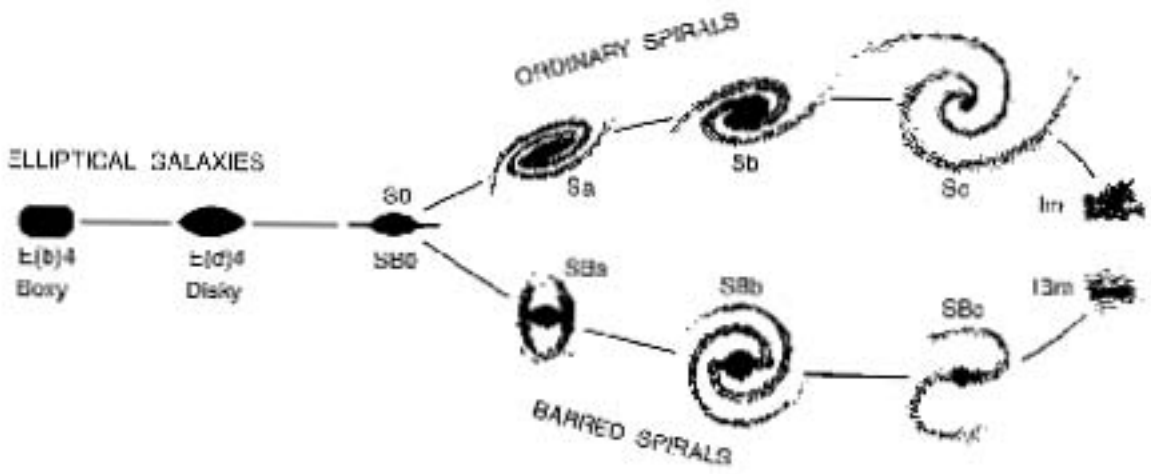

Figure 1.1: Tuning fork diagram of Hubble from Kormendy & Bender (1996).

with both types of galaxies, that is, an old stellar population like ellipticals and a rotating stellar disc like spirals.

At the time Hubble created this scheme of galaxies, it was believed that the diagram was a reflection of an evolutionary path, that the elliptical galaxies would evolve into flattened, disc-like structures, passing through the S0s, until they transform into spiral galaxies. Thus, ellipticals and lenticulars were designated as early-type galaxies and the spirals as late-type. Simultaneously, spiral galaxies were also divided as early-type spirals [S(SB)a] and late-type spirals for [S(SB)c galaxies].

For a long time, S0 galaxies were labeled as a transitional state between ellipticals and spirals. Originally, the S0s were classified as E7 by Hubble (1926), belonging to the elliptical galaxies, where the E7 were at the final phase of the elliptical branch and the union with the spirals. Later, Hubble (1936) introduced the term S0 to define a pure hypothetical state between the ellipticals E7 and the spirals Sa (SBa), but the transition of these types of galaxies would involve a violent event since it is observed a very well defined spiral structure in the Sa galaxies. The definition of S0s has been updated and refined by Sandage (1975); Sandage & Tammann (1981); Sandage & Bedke (1994).

1.2 Galaxies and their environment

Galaxies can be found in clusters, groups or in the field (isolated). Clusters and groups are concentrations of galaxies, where the distinction between one or another

is not abrupt. A cluster of galaxies consists of $N \gtrsim 50$ galaxies within a sphere of diameter $D \gtrsim 1.5h^{-1}\,\mathrm{Mpc}$, a mass range of $10^{14}\mathrm{M}_\odot < M < 10^{15}\mathrm{M}_\odot$, and their galaxies move with velocities of $800 - 1000\,\mathrm{km\ s^{-1}}$. George Abell (1958) created a catalog of rich galaxy clusters, where he identified an overdensity of galaxies in plates of the Palomar Observatory Sky Survey (POSS). For this, Abell aplied some criteria for a cluster to be included in the catalog: a cluster most have $\gtrsim 50$ galaxies with magnitudes between m_3 and $m_3 + 2$, where m_3 is the magnitude of the third brightest galaxy in the cluster, inside an angular radius of size $\theta_A = 1.7/z$ arc min, where z is the redshift and θ_A is now known as the Abell radius (equivalent to $R_A \approx 1.5h^{-1}\,\mathrm{Mpc}$), and within a redshift range of $0.02 \leq z \leq 0.2$. The redshift limits were chosen so that a cluster can be found on a single plate and due to the sensitivity limit of the plates. The catalog first contained clusters in the Nothern sky, corresponding to the POSS limits, and then it was expanded to the Southern sky (Abell et al. 1989). The catalog contains a total of 4076 clusters from both surveys and the clusters are denoted as Abell X or AX, where X is a number between 1 and 4076 and refers to the entry in the catalog.

Groups are composed of $N \lesssim 50$ objects in a sphere of diameter $D \lesssim 1.5h^{-1}\,\mathrm{Mpc}$, with a range of masses $10^{12} - 10^{13}\mathrm{M}_\odot$ and the velocity of the individual galaxies is $\sim 150 - 300\,\mathrm{km\ s^{-1}}$. Through X-ray observations it was discovered that clusters contain hot gas that permeates the space between the galaxies, the intracluster medium (ICM), with temperatures $10^7 - 10^8\,\mathrm{K}$ and a mass fraction higher than the mass in galaxies, that is $10 - 20\%$ corresponds to the ICM, $1 - 5\%$ to stars and the rest for the dark matter (Mohr et al. 1999; Vikhlinin et al. 2006; Budzynski et al. 2014; Chiu et al. 2018). The presence of a warm-hot intergalactic medium in groups has been also detected in X-ray observations and predicted in simulations, with temperatures of $10^5 - 10^7\,\mathrm{K}$ (Cen & Ostriker 2006).

Field galaxies are objects that do not belong to clusters nor have close luminous neighbours, although some of them may appear as pairs or loose/compact groups (Xu & Sulentic 1991; Karachentseva et al. 2011). According to Verdes-Montenegro et al. (2005), an isolated galaxy is an object that has not been affected by the interaction with its closest neighbour in a crossing time of $t_c \sim 3\,\mathrm{Gyr}$.

From the morphology-density relation in clusters of galaxies (Oemler 1974; Dressler 1980), it has been shown that spiral galaxies are more frequently observed in the outskirts of clusters, which is a low density environment, while S0s and ellipticals tend to lie in the central part of cluster. Postman & Geller (1984) observed that galaxies in groups follow a similar trend as the clusters, although at low densities (less than 5%) there is little dependence on the density for all population fractions (Es, S0s, spirals). The morphology-density relation suggests a dependence of galaxy evolution with the environment. On the other hand, the position of the lenticular galaxies in the Hubble diagram makes them of special interest to understand the

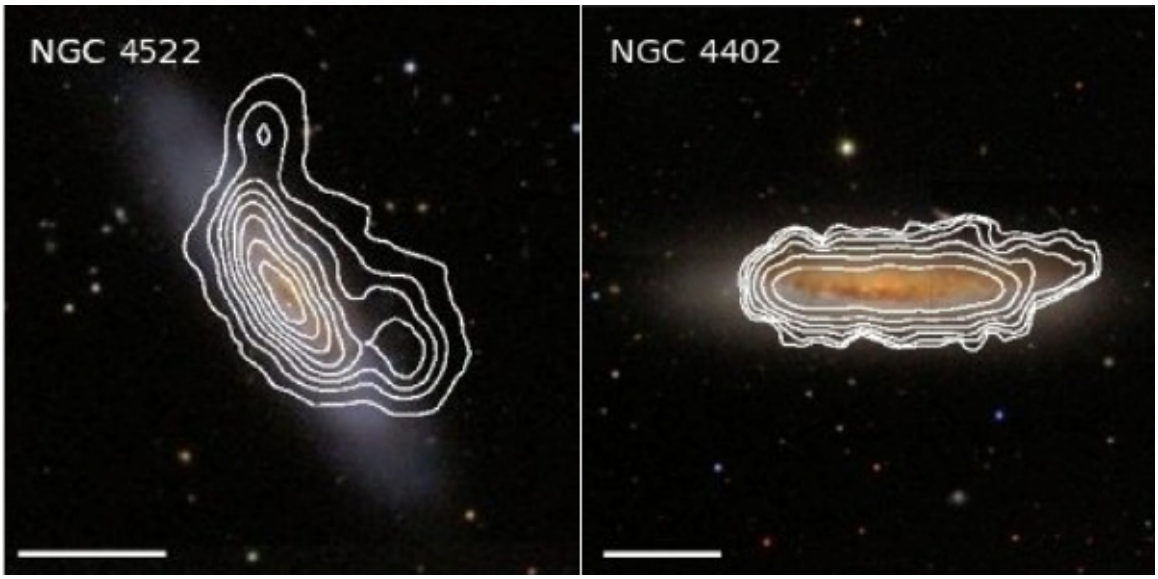

Figure 1.2: Textbook examples of spiral galaxies undergoing ram pressure stripping in the Virgo Cluster. The white contours show the HI distribution overlaid on an optical stellar images from Chung et al. (2009b).

formation and evolution of galaxies. The first authors to propose a mechanism for the formation of the S0s were Spitzer & Baade (1951), who suggested that the S0 emerged from the collisions of galaxies in a rich cluster, where they lost their gas. Nevertheless, Gunn & Gott (1972) pointed out that the conditions observed in clusters of galaxies are unfavorable to have enough collisions to produce the observed fraction of S0s.

1.2.1 Transformation processes of disc galaxies

Several mechanisms have been proposed to explain the morphological transformation of a spiral galaxy into an S0.

- *Ram pressure stripping (RPS).* Gunn & Gott (1972) suggested that S0s in clusters are the descendants of spiral galaxies that lost their interstellar medium (ISM) through the ram pressure exerted by the hot intracluster medium (ICM) when the galaxies travel within the cluster. The ram pressure of the ICM on a moving galaxy is given by

$$P_{\rm ram} = \rho_{\rm ICM} v_{\rm gal}^2 \,, \tag{1.1}$$

where $\rho_{\rm ICM}$ is the ICM density and $v_{\rm gal}$ is the velocity at which the galaxy is moving in the cluster. On the other hand, the ISM is bound to the galaxy through its gravitational potential which would retain the gas of the disc, acting as a restoring force per unit area,

$$F(r) = -\frac{\partial \Phi(r, z_{\rm max})}{\partial z}\, \Sigma_g(r)\,, \tag{1.2}$$

where $z_{\rm max}$ is the height of the disc at which the gravitational force in the z-direction is maximum, for a disc moving face-on into the ICM. If the ram pressure surpasses the galaxy's gravitational force ($P_{\rm ram} > F(r)$), then the gas would be swept away from the disc (Gunn-Gott criterion). The radius at which both forces are equal is known as the truncation or stripping radius and is the size of the remnant gaseous disc after a galaxy has experienced the RPS.

Since this mechanism was proposed, several models have been carried out to explore the role of RPS in galaxy transformation, e.g. spirals into lenticulars or dwarf irregulars into dwarf spheroidals. Different methods and techniques have been employed to study this phenomenon, with SPH or grid codes, varying the parameters of the ICM (density, temperature, velocity) and galaxy inclination, orbits or masses; some include star formation and/or a multiphase ISM (Abadi et al. 1999; Quilis et al. 2000; Roediger & Hensler 2005; Roediger & Brüggen 2006; Vollmer et al. 2006; Kronberger et al. 2008; Tonnesen & Bryan 2012, and Roediger 2009 for a review). Good examples of galaxies affected by the RPS are NGC 4522 and NGC 4402 (fig. 1.2) in the Virgo Cluster, since they exhibit an asymmetric or perturbed distribution of gas with an unperturbed stellar disc. There are extreme cases of stripped galaxies that exhibit long "tentacles" of debris material: these are called "jellyfish" galaxies (Smith et al. 2010a). Many multiwavelength observations in the last decades have been used to study RPS in spirals: Cayatte et al. (1990); Kenney & Koopmann (1999); Kenney et al. (2004); Sun et al. (2006); Zhang et al. (2013); Jáchym et al. (2014); Poggianti et al. (2016), to name a few.

- *Galaxy harassment.* According to Moore et al. (1996), a bright galaxy, with a luminosity $\sim 2 \times 10^{10} \mathrm{L}_{\odot}$[1] would experience close and frequent encounters with other galaxies of similar masses moving at high velocities $\gtrsim 1000\,\mathrm{km\ s^{-1}}$, where each fly-by occurs once every $\sim 1\,\mathrm{Gyr}$ within a distance of $\sim 50\,\mathrm{kpc}$. Moore et al. (1996, 1998), through N-body simulations, found that disc galaxies orbiting a dense cluster (e.g. Coma cluster) were transformed into dwarf ellipticals or spheroidals (dE/Sph) and in some cases the galaxies retain a thick

[1] This value corresponds to L_*, the characteristic break in the luminosity function in the B-band (Schechter 1976).

stellar disc resembling a dwarf lenticular (dS0). These interactions can change the morphology of the galaxies without mergers or fusions taking place. Smith et al. (2010b, 2013) presented simulations of galaxy harassment in dwarf disc galaxies (masses of $\sim 1 \times 10^8 M_\odot$ in stars) infalling towards the cluster centre. In these models, the stellar component is mildly affected by the interactions with losses of $\sim 10\%$ while the dark matter have losses of $50 - 90\%$, where the disc component is mostly preserved, dominated by rotation, and with an induced spiral structure. The mass in these dwarf galaxies is more concentrated, therefore they are less susceptible to such interactions and the initial dark matter distribution is more extended.

- *Starvation* or *strangulation*. From studies of the star formation rate in spiral galaxies, it is expected for the ISM to be consumed within time scales shorter than the Hubble time (Larson et al. 1980; Kennicut 1983). However, it is known that spiral galaxies are accreting gas from gas-rich envelopes, streams, satellite galaxies, tidal debris or primordial gas (Oort 1970; Haynes 1979; Lacey & Cole 1993; Sancisi et al. 2008) at a rate similar to what is consumed in the star formation activity (Larson et al. 1980; Sancisi et al. 2008). Through the starvation or strangulation (Larson et al. 1980) spirals would lose their gas reservoir, so that no more fuel is replenished to the disc and the ISM consumption would lead to a change in colour produced by the quenching of the star formation. From this process, spirals end up as gas-poor galaxies similar to the S0s. Simulations by Bekki et al. (2002) of this process showed that a spiral orbiting a cluster could lose up to 80% of its halo gas in a few gigayears by the interaction with the hot ICM and the global tidal field of the cluster and, therefore, the stripped halo gas could not fall back into the galaxy. Under this scheme, the starvation happens over a long time scale since the gas reservoir should be removed from the galaxy first, and then, the star formation shuts down when its fuel runs out (in a time scale of gigayears).

- *Thermal evaporation*: the high temperature of the ICM heats up the cold ISM at the interface between the two media, so that the ISM evaporates off the galaxy since it is no longer bound by the galaxy gravitational potential well (Cowie & Songaila 1977). The evaporation depends mostly on the ICM temperature but also its efficiency can be reduced in the presence of the magnetic field (Vikhlinin et al. 1997). It has been estimated that this mechanism has a time scale of 10^8 to 10^9 yr (Boselli & Gavazzi 2006).

- *Tidal interactions between the galaxy and the cluster gravitational potential well*: Due to the difference in the masses of the clusters ($\gtrsim 10^{14} M_\odot$) and the galaxies ($10^9 - 10^{11} M_\odot$), the cluster gravitational potential might perturb a galaxy inducing gas inflow, bar formation, nuclear and disc star formation

(Merritt 1984; Miller 1986; Byrd & Valtonen 1990).

- *Tidal interactions between pairs of galaxies.* Although some of the previously described processes could be very efficient in transforming spiral galaxies into S0s, they can only account for S0s in clusters. But lenticulars have also been found in groups and in the field, such as the case of NGC 3115 which is a relatively isolated S0 with a dwarf elliptical galaxy (dE,N) as a companion (NGC 3115 DW1, Puzia et al. 2000). Tidal interactions can have an impact on various galaxy components: gas, dust, stars and even in the dark matter. Also, they may produce shocks in the gaseous disc that would lead to radial transport of the gas in the perturbed galaxy and/or increased consumption of gas by star formation (Icke 1985). Observations (Condon et al. 1982; Keel et al. 1985; Kennicutt et al. 1987; Hummel et al. 1990) and simulations (Mihos et al. 1992; Iono et al. 2004) showed that interacting pairs of galaxies have an increase in the nuclear activity. Also, these interactions can easily remove the HI gas from the outskirts of the galaxy which is less bound than the molecular gas located in the inner parts of the galaxy (Valluri & Jog 1990). An example of a pair of interacting galaxies can be observed in the Virgo Cluster between the galaxies NGC 4435 and NGC 4438.

- *Mergers.* Fusions or mergers between galaxies can induce an increased star formation rate producing starbursts that rapidly modify the appearance of the galaxy. Depending on the mass ratio between the galaxies, these fusions can be classified as *major* (Toomre & Toomre 1972; Borlaff et al. 2014; Tapia et al. 2017) when the mass ratio is $> 1/3$, and *minor* mergers (Aguerri et al. 2001; Tapia et al. 2014) for ratios $< 1/3$. Mergers are most likely to occur in the ambients of groups, since they have shorter duration times than in clusters (10^8 yr) due to the lower relative velocity of the galaxies (Toomre 1977).

To better understand which is the appropiate mechanism of S0s formation and determine whether spirals are S0s progenitors, it is necessary to study and compare the different components of these galaxies.

1.3 Components of disc galaxies: S0s and spirals

Even though spirals and S0 galaxies have a stellar disc in common, the later have lower gas content (Gallagher, Faber & Balick 1975) and some observations indicate that the last star formation episode took place at the bulge (Prochaska Chamberlain et al. 2011; Sil'chenko 2006; Sil'chenko et al. 2012; Bedregal 2012; Johnston et al. 2012, 2014, but see Katkov et al. 2015), while in spiral galaxies

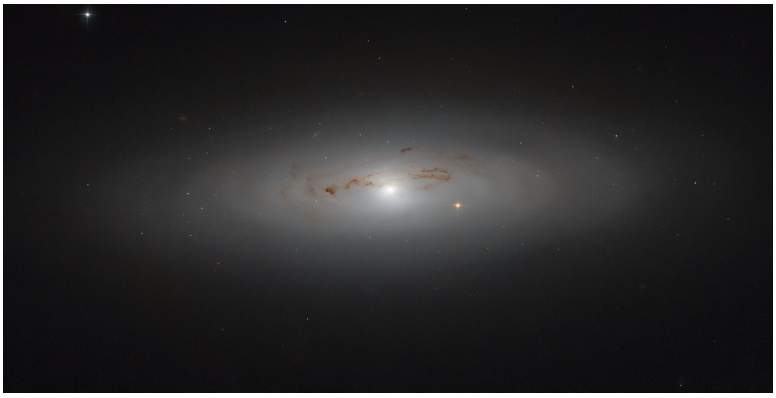

Figure 1.3: Lenticular galaxy NGC 4036. Credit: ESA/Hubble & NASA.

the star formation is on-going throughout the disc. Fig. 1.3 shows NGC 4036, an example of an S0 galaxy with a tenuous dusty disc.

Galaxies are systems that can be composed of different elements: discs, spheroids, spiral arms, bars. The stellar surface brightness of each structural component of a galaxy may be modeled with a mathematical law. Given that the total surface brightness of a galaxy is the sum of all the components, then the analysis and comparison of each component with galaxies of different morphological type and at different redshift can help to understand more of the formation and evolution of galaxies. Bars, ovals, lenses, bulge and disc have been identified and characterized in recent studies of disc galaxies.

Bulge The bulges are spheroidal concentrations of stars, moving predominantly in random orbits, and located in the central region of most of disc galaxies, spirals and lenticulars, with low gas content and old stellar population resembling the elliptical galaxies. The first models proposed to fit the surface brightness of the bulges were the ones for elliptical galaxies, being the first objects of this kind to be analysed (Reynolds 1913; Hubble 1930; King 1962; Rood et al. 1972; Oemler 1976; see also Graham 2013). Probably the most popular model used to fit the distribution of E's and bulges of S0s and spirals was the de Vaucouleurs (1948, 1953) $r^{1/4}$ profile. In this model, the intensity of the surface brightness is given by the radial function:

$$I_b(r) = I_{b,e} 10^{-7.669\left[(r/r_e)^{1/4}-1\right]}, \tag{1.3}$$

where $I_{b,e}$ is the effective surface density and r_e is the effective radius that contains half of the total intensity of the galaxy. Although the de Vaucouleurs

profile has been widely used, it was later replaced by the Sérsic (1968) law since Andredakis & Sanders (1994) determined that the bulges of late-type spirals were better fitted with a Sérsic profile. The Sérsic law was later extended to other morphological types of galaxies (Andredakis et al. 1995) and for optical and near-IR observations (Prieto et al. 2001; Aguerri et al. 2005; Laurikainen et al. 2010; Méndez-Abreu et al. 2010). The radial surface intensity of the Sérsic law is given by

$$I_b(r) = I_{b,e} e^{-b_n\left[(r/r_e)^{1/n}-1\right]}, \tag{1.4}$$

where $I_{b,e}$ is the intensity at the effective radius r_e, which contains the half of the total light distribution, the coefficient $b_n \sim 1.9992n - 0.327$ (Capaccioli 1989), and n is the parameter that describes the shape of the profile. The Sérsic model is a generalization of the de Vaucouleurs ($n = 4$) and the exponential ($n = 1$) fitting models.

Disc The disc is composed of stars and gas moving in nearly circular orbits with very little random motion. Most of the stars of the galaxies lie in the disc. For the stellar component, the surface brightness intensity can be modelled with an exponential function (Freeman 1970):

$$I_d(r) = I_{d,0} e^{-(r/h)}, \tag{1.5}$$

where $I_{d,0}$ is the central intensity of the disc and h is the profile scale length. Even when this function fits very well the disc stellar distribution, it has been recently shown that the stars in the external parts of the disc do not follow an exponential law: in $\sim 60\%$ of disc galaxies the exponential law drops faster after a certain break radius, i.e. the disc is truncated, whereas $\sim 30\%$ of the discs present a slow decline at the break radius, that is they are anti-truncated (Pohlen & Trujillo 2006). The shape of the brightness profile is related to the Hubble type, where anti-truncated discs are more frecuent in early-type galaxies and late-type discs are truncated (Pohlen & Trujillo 2006).

In the case of the spirals, the gaseous disc is approximately 10% of the stellar mass. The gas fills the space between the stars in the disc and is called the interstellar medium (ISM) and consists of atomic hydrogen, warm ionized, warm and cold neutral, and molecular gas (H_2) which serves as fuel for the star formation in the disc. The 21cm emission of the HI can trace its distribution in the disc reveling structures like the spiral arms or flaring. It has also been a good tool to measure the galactic rotation curve. Lenticular galaxies, as it was mentioned earlier, have very little or null fraction of gas (Gallagher, Faber & Balick 1975) so the study of the kinematics depends on the stars.

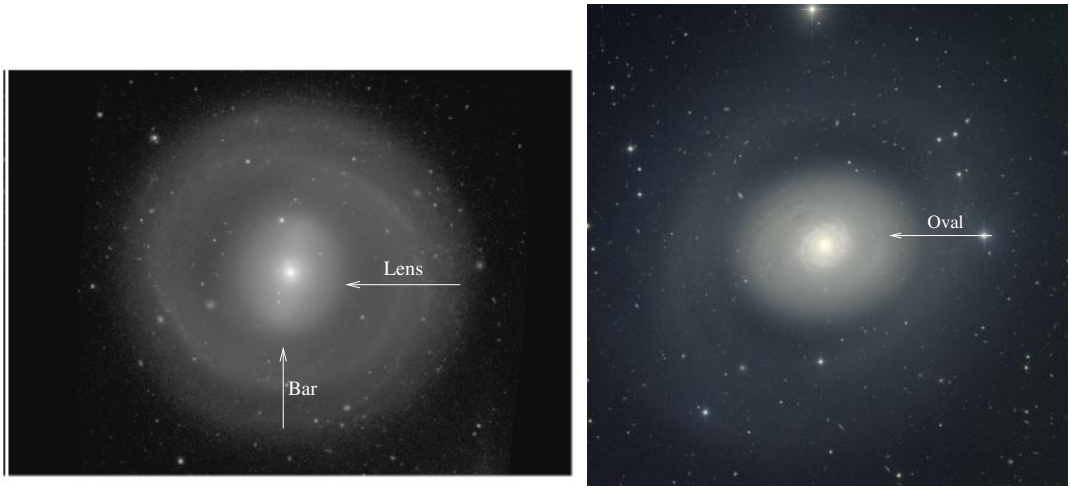

Figure 1.4: Examples of disc galaxies where structural components are observed. *Left*: Image in *B*-band of the lenticular barred galaxy NGC 1291 (SB0) with a lens (from Buta et al. 2010). *Right*: Spiral galaxy M94 (Sab) with an oval component (Credit: Hillary Mathis, N.A.Sharp/NOAO/AURA/NSF).

Bar The bars are linear structures of stars, with gas and dust in the case of spirals (see fig. 1.4). Most of the bars can be easy to identify visually when they are very dominant, or they can be observed in residual maps when the bar is weak. The first studies of bars surface brightness showed that bars in early-type discs have constant profile while late-type discs present bars following an exponential law (Elmegreen & Elmegreen 1985). Despite the difficulty of establishing the best fit for the bars, since there are several free parameters to consider, further photometric analysis of bars have provided more models for its radial surface intensity. One proposed model is the Ferrers bar (see Laurikainen et al. 2005, 2007):

$$I_B(r) = I_{B,0}\left[1-\left(\frac{r}{r_B}\right)^2\right]^{(n_B+0.5)}, \tag{1.6}$$

where $I_{B,0}$, r_B and n_B are the central intensity, the length and the shape parameter of the bar, respectively. Although the Ferrers bar has been widely used, other proposed models are from Freeman (1966); Prieto et al. (1997, 2001); Aguerri et al. (2003, 2005).

Lens These are components with a nearly constant surface brigthness profile and a sharp outer edge (Kormendy & Kennicutt 2004). These axisymmetric structures cannot be identified as easy as the bars when the bulge is prominent,

but they appear in residual maps. Lenses are common elements of S0s and early-type spirals, given that they appear in $> 50\%$ of the S0, SB0 and Sa galaxies (Kormendy 1979; Laurikainen et al. 2005, 2007, 2009), although they can be found more frequently in barred galaxies, where the bar lies inside the lens (fig. 1.4), then in unbarred galaxies. In face-on S0s, they appear as exponential subsections in the surface brightness profile (Burstein 1979b; Tsikoudi 1980; Kormendy 1979, 1982; Laurikainen et al. 2005, 2006, 2009). Duval & Athanassoula (1983) fitted a model for a lens based on the observations of the galaxy NGC 5383:

$$I_l(r) = I_{l,0}\left[1 - \left(\frac{r}{r_l}\right)^2\right], \tag{1.7}$$

for $r < r_l$, where $I_{l,0}$ and r_l are the central surface brightness and the length of the lens. This function has been used for lenses found in S0s (Prieto et al. 2001; Aguerri et al. 2005). Some studies suggest that the lenses may be anti-truncated discs inside bulges or halos (Erwin et al. 2005), however, in some galaxies, the lenses appear several times throughout the disc (Laurikainen et al. 2010).

Oval Finally, the ovals are global deviations of the axisymmetric shape of the discs and they appear in isophotal analysis similarly to bars but have low ellipticities compared to bars (minor-to-major axis ratio $b/a > 0.85$, see Kormendy & Kennicutt 2004). Ovals are mostly present in unbarred galaxies (Kormendy 2013) as seen in the galaxy M94 (fig. 1.4).

The study of the different galaxy components may help characterize its global parameters like length scale, effective surface brightness, bulge-to-disc or bulge-to-total luminosity ratio, and to establish relations within these parameters to obtain a better idea about the formation and evolution of each component or the galaxies. Laurikainen et al. (2010) analysed the relations between the photometric components from a sample of 175 lenticular galaxies from the Near-Infrared Survey of S0s (NIRSOS) and nearly 200 spirals of the Ohio State University Bright Spiral Galaxy Survey (OSUBSGS), through a 2D multi-component decomposition with K_s band images. From this sample, it was found from the photometric plane (r_{eff}, μ_{ob} and n) and in the M_K^0(bulge) versus r_{eff} diagram that the bulges of S0s are more related to the bulges of spiral galaxies than to ellipticals, and only the brightest bulges of S0-Sa are in the same region of the ellipticals in the Kormendy relation (r_{eff} versus $< \mu >_{eff}$). S0 galaxies with similar size to dwarf ellipticals (dEs) present higher surface brightness than the dEs which means that not all S0s would evolve into dwarfs galaxies through galaxy harassment (Moore et al. 1996).

It has been traditionally seen that lenticular galaxies have more prominent bulges than spirals (Simien & de Vaucouleurs 1986), with bulge-to-disc luminosity ratio $B/D \gtrsim 0.3$ (or bulge-to-total luminosity $B/T \gtrsim 0.7$; Burstein 1979a). More recent studies on the surface brightness have shown that S0s have on average $B/T \sim 0.2-0.3$ (Weinzirl et al. 2009; Balcells et al. 2007; Laurikainen et al. 2007) although it covers a wide range of values spreading through the Hubble sequence, so that even late-type spirals could evolve into S0s although the percentage of S0s with B/T similar to late-type spirals (< 0.15) is 13% (Laurikainen et al. 2010).

Correlations between the bulges and disc are expected if the discs formed first and the bulges later through secular evolution. Such a correlation between the effective radius r_{eff} of the bulge and the length scale h_r of the disc for spiral galaxies has been found by Courteau et al. (1996); de Jong (1996); Graham & Prieto (1999); Carollo et al. (2007), to name a few, and also for S0 galaxies by Aguerri et al. (2005); Laurikainen et al. (2009), and Méndez-Abreu et al. (2008), for S0-Sb. From the NIRSOS and OSUBSGS sample (Laurikainen et al. 2010) the average values of r_{eff}/h_r are ~ 0.2, ~ 0.15 and ~ 0.1 for S0, S0a-Sa and Sb-Sc galaxies, respectively, and the range of h_r is similar for S0s and spiral galaxies ($h_r = 1-10\,\mathrm{kpc}$). Additionally, in these galaxies has been found that the disc luminosity M_K^0(disc) increases with increasing scale length h_r and that the central surface brightness μ_0 becomes weaker, which has been previously shown by Méndez-Abreu et al. (2008) for S0s and Graham & de Blok (2001); Balcells et al. (2007); Graham & Worley (2008) for spirals.

An indication of the similarity or differences of the bulges and discs of spirals and S0s is the correlation between the absolute brightness of the bulge M_K^0(bulge) and the disc M_K^0(disc)[2] (de Jong 1996; Hunt et al. 2004; Noordermeer & van der Hulst 2007). Laurikainen et al. (2010) found that S0 and S0/a-Sa galaxies with M_K^0(bulge) brighter than $-22\,\mathrm{mag}$ have bulges and discs with similar luminosity, in the case of S0 and Sbc galaxies, their luminosities are similar when they lie within the range of M_K^0(bulge) ~ -19 to $\sim -25\,\mathrm{mag}$, and for S0/a and Scd when $M_K^0(bulge) \sim -16$ to $\sim -22\,\mathrm{mag}$, that is, spiral galaxies with bulges brighter than $M_K^0(bulge) \sim -20\,\mathrm{mag}$ can evolve into S0s by the stripping of their ISM.

The Tully-Fisher relation (TFR) correlates the circular velocity with the stellar luminosity of disc galaxies. For S0s, the analysis of the TF relation has not been an easy task since the lack of gas in these galaxies makes it difficult to obtain its circular velocity. So, instead of using gas emission linewidth, the rotation curve is obtained with stellar absorption lines (Neistein et al. 1999; Hinz et al. 2001, 2003; Bedregal et al. 2006), emission lines of planetary nebula (Noordermeer et al. 2008), or with the construction of dynamical models (Mathieu et al. 2002). These studies

[2] M_K^0(bulge/disc) is the absolute brightness of the bulge/disc in the K-band.

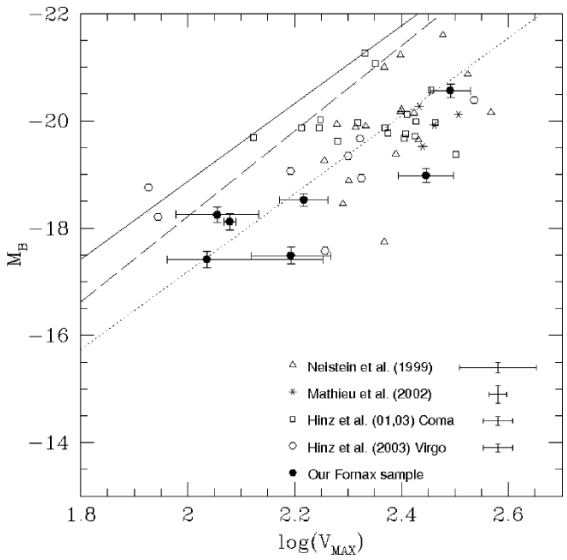

Figure 1.5: Tully-Fisher relation in the B-band for a sample of spiral (solid and dashed lines) and S0 (dotted line) galaxies (Bedregal et al. 2006).

have found that the slope in the TFR for S0s is similar to that of late-type spirals with an offset in the luminosity for a given circular velocity (see fig. 1.5); the S0s are below the spirals in the TFR (S0s are fainter). The offset in the TFR between S0s and spirals could arise from the stripping of gas followed by the truncation of the star formation within time-scales of a few Gyr, thus affecting the luminosisty of the galaxies. The TFR and the results from Laurikainen et al. (2010) suggest that S0s could evolve from late-type spirals where the star formation has been shut down $\sim 1\,\mathrm{Gyr}$ ago through the RPS of the interstellar medium.

Further evidence for the transformation of spirals into S0s can be found in their globular clusters. If a galaxy is subject to the RPS, the number of globular clusters would not be affected by this process, which has been found by Aragón-Salamanca et al. (2006) and Barr et al. (2007).

1.4 Comparison of cluster vs field galaxies

Several differences have been observed in cluster galaxies compared to field galaxies of the same morphological type (van den Bergh 1960), specifically the gas content as measured through the HI 21 cm line emission. The deficiency of HI (neutral hydrogen) gas in cluster spirals, as a possible effect of the RPS, has been

observed since the 70's (Haynes et al. 1984 and Boselli & Gavazzi 2006 for a review). The distribution of the HI is less extended in cluster galaxies than its counterparts in the field, for a given morphological type and luminosity (Warmels 1988; Cayatte et al. 1994; Boselli et al. 2002), where isolated galaxies have HI discs with diameters ~ 1.8 larger than the optical diameter (in the B-band 25 mag arcsec^{-2} isophote), while the galaxies closest to the Virgo cluster center present HI diameter up to 5 times smaller than the optical one. Spirals in the Virgo cluster have an average surface density of HI that is ~ 0.5 times the observed in non-cluster spirals of the similar morphological type (Davies & Lewis 1973). Additionally, the HI deficiency increases with decreasing (angular) distance to the center of the X-ray emission of the cluster (van Gorkom & Kotanyi 1985; Gavazzi 1989; Boselli 1994; Solanes et al. 2001).

Surveys of molecular gas (CO) in the Virgo Cluster (Stark et al. 1986; Kenney & Young 1988; Boselli et al. 1995) and in the Coma Cluster (Boselli et al. 1997; Casoli et al. 1991) have shown that cluster galaxies have on average normal molecular gas content. This is possible since the molecular clouds (containing CO) are more bound to the galactic potential well than the atomic gas, hence is more difficult to strip the molecular gas when a galaxy interacts with the ICM through the RPS (Zasov 1975).

Metals are produced by the stars during their evolution and ejected to the ISM through stellar winds or supernova explosions. Therefore, they can be used to constrain the star formation history of galaxies. Skillman et al. (1996) analyzed the metal content of 9 galaxies from the Virgo Cluster and compared them with isolated objects of similar type. They found that HI-deficient galaxies have on average higher metallicity than HI-normal galaxies in the outskirts of the cluster or isolated, and HI-normal galaxies from the periphery of the Virgo Cluster have similar abundances than isolated/field galaxies. On the other hand, Mouhcine et al. (2007) found that the gas-phase oxygen abundance vs. stellar mass is independent of the environment in a wide range of local galactic densities, although at a fixed stellar mass, galaxies in high density environments are slightly overabundant in oxygen. Additionally, the metallicity increases with decreasing stellar mass, given that less massive galaxies confined in a dense environment (e.g. the ICM) have a lower efficiency to expel metals and thus retain more gas to form new stars, while massive galaxies retain their gas independently if they are in a cluster or the field. According to Shields et al. (1991), the removal of the (outer) HI disc would prevent radial inflow of metal-poor gas and hence elevate the abundance. The reduction of the infalling metal-poor gas on cluster core spirals may account for some of the enhanced abundance (Skillman et al. 1996). However, no consensus has been reached whether or not the environment affects the chemical evolution of galaxies, since galaxies with both enhanced and reduced metallicities can be found at any environmental density, and

even though galaxies in clusters are slightly more abundant, this suggests that the metal enrichment is an intrinsic galaxy property (Ellison et al. 2009; Pilyugin et al. 2017, and references there in).

From $H\alpha$ emission of Virgo and isolated galaxies of similar Hubble type, Kennicutt (1983b) found that Virgo galaxies have on average lower star forming activity, redder colors and lower HI gas content than their counterparts in the field. This was later confirmed for other cluster galaxies from Virgo, Coma and A1367, where galaxies with normal HI content (HI-def<0.4) have higher Hα equivalent width (EW) than their HI deficient counterparts (HI-def>0.4) by a factor of 2. From Koopmann & Kenney (1998, 2004a,b) and Koopmann et al. (2006) the star formation also on Virgo Cluster galaxies is reduced in the outer disc, producing truncated Hα profiles, with normal o even enhanced activity in the inner disc. According to the Schmidt law, a decrease in the total gas column density leads to a decrease in the star formation, producing a radial truncation of this activity. Boselli et al. (2006b) reproduce different profiles for the anemic galaxy NGC 4569: total gas, star formation and various stellar populations, assuming an RPS event that took place ~ 400 Myr ago, which means that an HI-deficient cluster galaxy with a truncated Hα disc and an unperturbed stellar disc should have experienced RPS recently (a few 100 Myr ago) and close to the cluster centre. The star formation decreases with increasing galactic density (above $\sim 1 h_{75}^{-2}\,\mathrm{Mpc}^{-2}$) and decreasing cluster centric radii, between $1-2$ virial radii (Lewis et al. 2002; Gómez et al. 2003; Nichol 2004; Tanaka et al. 2004), in accordance to the HI-deficiency (for a review see Boselli & Gavazzi 2006).

The radio emission in late-type galaxies is dominated by the synchrotron emission of cosmic ray electrons gyrating around the magnetic field (MF) lines, so that this emission also reflects star formation activity given that the cosmic rays are accelerated in supernova explosions. Spiral galaxies from the Coma and A1367 Clusters show an enhanced radio continuum emission by a factor of ~ 5 compared to field galaxies (Gavazzi & Jaffe 1986) which was later confirmed by Andersen & Owen (1995); Rengarajan et al. (1997); Gavazzi & Boselli (1999). A marginal increase was observed in the Virgo and A262 Clusters and none in loose clusters like Cancer (Gavazzi & Boselli 1999). In the Coma and A1367 Clusters, the enhanced radio emission could be related to the conditions of the ICM, where it has been estimated from X-ray observations (X-ray luminosities L_X and temperature T_X) that these clusters have higher ICM densities n_{ICM} than the other ones (Trinchieri et al. 1997; White et al. 1997; Gavazzi & Boselli 1999). Since the star formation is similar or lower in cluster than in field galaxies, an enhancement in the radio emission implies an increase in the magnetic field density by a factor of $\sim 2-3$ possibly due to compression (Gavazzi & Boselli 1999) or shock-induced reaccelerated cosmic ray electrons (Völk & Xu 1994).

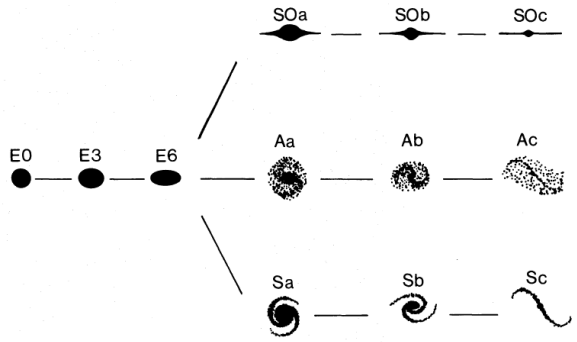

Figure 1.6: Modified Hubble sequence of galaxy clasification as proposed by van den Bergh (1976). The S0s and anemic galaxies run through a parallel sequence of the spirals.

1.4.1 Anemic spiral galaxies

van den Bergh (1976) identified another type of galaxies with a smooth spiral structure, HI-deficient, low star formation activity, and redder colors than normal spirals that are frequently found in clusters of galaxies. He called them *anemic galaxies* (A) and some examples of these type of galaxies are NGC 4548, NGC 4941, and NGC 4866 in the Virgo cluster, and NGC 4921 in the Coma cluster. These galaxies may have lost most of their gas by RPS when moving rapidly within the hot ICM. van den Bergh (1976) proposed a new classification system where S0 and anemic galaxies should follow a parallel sequence to the spirals in the Hubble diagram. According to van den Bergh's scheme, spirals with disc-to-bulge (D/B) ratios of 1 to 3 were classified as Sa, objects with D/B from 3 to 10 were classified as Sb and finally Sc galaxies have $D/B > 10$, and the same criterion was used to define the sequences Aa, Ab, Ac for anemic spirals, and S0a, S0b, S0c for lenticulars (fig. 1.6). Additionally, since the transition between the S0 and A galaxies is continous, galaxies with dust and dust-free but without evidence of Pop I stars were assigned to the S0a, S0b, S0c sequence, whilst flattened disc containing some Pop I stars form the Aa, Ab and Ac sequence. Although the anemics are HI deficient, Ab galaxies present CO fluxes similar to the Sbs, and the CO/HI ratio is larger in Ab than in Sb objects, that is A galaxies are deficient in HI gas but not in CO (van den Bergh 1991). Once the disc galaxies were formed, some of these would retain a fraction of gas in their discs. If during its evolution the discs keep the gas on it, then they will be normal star forming galaxies. On the other hand, if part of the gas is swept, they will be anemics or, if they lose all the gas, the discs will transform into lenticulars (van den Bergh 1976). Based on this idea, the anemic spiral galaxies could be an example of galaxies losing its ISM through the RPS and are on its way to become

S0s (van den Bergh 1991).

1.4.2 Jellyfish galaxies

Galaxies showing strong evidence of losing their ISM through the ram pressure of the ICM are the so-called "jellyfish" galaxies. Jellyfish galaxies exhibit long and filamentary tails of dust and ionized gas, similar to tentacles, given that this material has been removed from the galaxy main body resembling a jellyfish (fig. 1.7). This type of galaxies have been observed in clusters for years, but it was until Smith et al. (2010a) where the term jellyfish was used for the first time. Observations of jellyfish galaxies range from X-ray to radio wavelengths were tails of tens of kpc are detected. From UV and optical (Hα) images in the Coma Cluster, Smith et al. (2010a) identified galaxies undergoing RPS, since the galaxies showed large tails of UV bright debris associated with young stars, where the galaxies are located close to the cluster centre, with 40% in the central $\sim 500\,\mathrm{kpc}$ and $< 5\%$ beyond 1 Mpc, with the tails pointing away from the cluster centre indicating that they are on their first passage and free-falling into the cluster. In the Coma Cluster, more galaxies with long ionized gas tails were found at a distance between $0.2 - 1\,\mathrm{Mpc}$ from the cluster centre (Yagi et al. 2010).

The jellyfish galaxy ESO 137-001 is a late type spiral in the Norma Cluster (A3627) with a double X-ray tail of length $\sim 80\,\mathrm{kpc}$ (Sun et al. 2006, 2010) and an Hα tail that extends up to $\sim 40\,\mathrm{kpc}$ away from the galaxy main body aligned with the X-ray tail (Sun et al. 2007), where HII regions are located along the tail indicating that the star formation is still active in the stripped gas (see fig. 1.7). Also, molecular gas was detected in the tail extending to $\sim 40\,\mathrm{kpc}$ (Jáchym et al. 2014). ESO 137-002 is also a jellyfish galaxy in A3627 and has a long X-ray tail of length $\sim 40\,\mathrm{kpc}$ and an Hα tail of $\sim 20\,\mathrm{kpc}$ at the same position of the X-ray tail, however HII regions were not found along the tail (Sun et al. 2010). Zhang et al. (2013) observed a secondary Hα tail in ESO 137-002 with a lenght of $\sim 12\,\mathrm{kpc}$.

Other two examples of jellyfish galaxies, with extended tails of bright blue knots and filaments of young stars, were found in the A2667 and A1689 clusters, respectively (Cortese et al. 2007). The galaxy in A1689 has lost $\sim 80\%$ of its mass in neutral hydrogen since is less luminous ($L \sim 0.1L_*$) than that of A2667 ($L \sim L_*$), and given that both clusters have similar masses and ICM density profiles and the galaxies are located at similar projected distances from the cluster centre, thus the RPS most be the dominant process in the low-mass galaxy while in the high-mass galaxy could be a combitation of the interaction with the cluster gravitational potential well and RPS.

In a series of papers by the ESO large program GASP (GAs Stripping Phe-

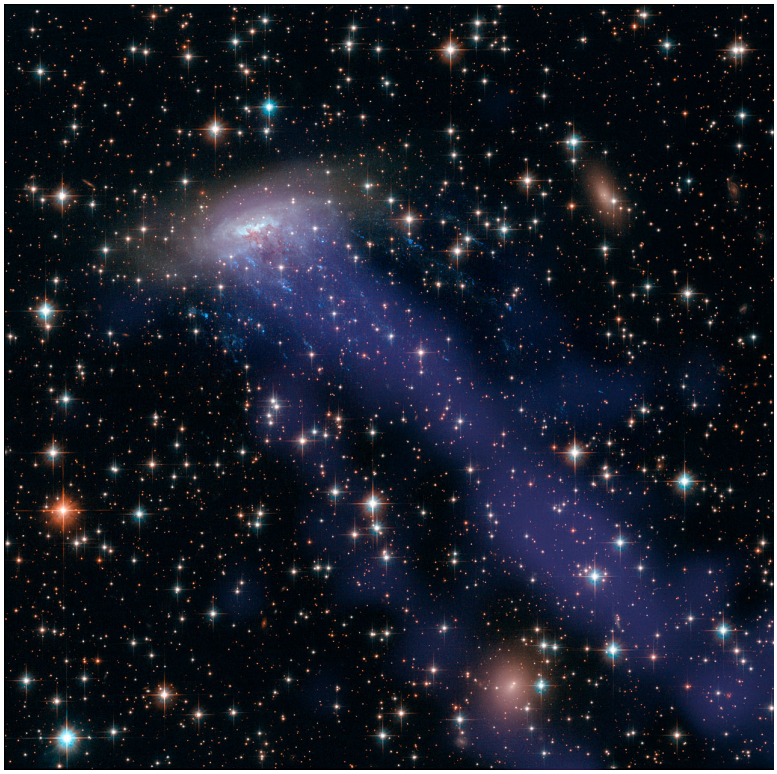

Figure 1.7: Jellyfish galaxy ESO 137-001 in the Norma Cluster. The X-ray emission from the stripped tail is shown in blue. Credit: NASA/ESA/CXC.

nomena in galaxies with MUSE), over 100 galaxies with signs of gas stripping have been observed (see Poggianti et al. 2017b, Paper I). This project has been able to analyse properties in the tails and in the main body of the jellyfish galaxies, such as gas and stellar kinematics, stellar populations, gas masses, star formation rates, gas metallicities; for a wide range of galaxy masses and different environments (clusters, groups and field galaxies) with the aim of study the gas removal through RPS as a function of the environment and how it affects the physics of the ISM.

After losing their gas, jellyfish galaxies would evolve into poor-gas objects by consuming the remaining gas through the star formation. Once the gas is consumed, the star formation will be quenched and these galaxies finally would become S0s, so jellyfish are possible on their way to transform into lenticulars.

This thesis is focused on the loss of the ISM through the ram pressure stripping by performing numerical simulations to follow the evolution of a gaseous disc with galactic MFs interacting with the ICM. For a better understanding on the matter, in Chapter 2 is presented a summary of what has been done in terms of numerical simulations and what it is known from observations of galaxies undergoing ram pressure stripping to compare with the models presented in this thesis followed by the description and analysis of the magnetohydrodynamical (MHD) simulations carried out in this work and a comparision with pure hydrodynamic models. In the MHD models, galactic magnetic fields are included, since this component has been hardly explored in RPS simulations and we consider that it should have an impact on the gas dynamics and the structure of the gas tails. Chapter 3 shows the evolution and structure of the MF in the simulations of RPS as a function of the galactic disc inclination and also the synthetic observations of synchrotron emission and polarization obtained from the models. The work in progress related to study the gas kinemtics and star formation in stripped tails, as well as the chemical enrichment of the ICM is presented in Chapter 4. Finally, in Chapter 5 the general conclusions of the work are presented.

Chapter 2

MHD simulations of ram pressure stripping of a disc galaxy

In this chapter, the first publication containing the results of this thesis is shown, entitled *MHD Simulations of ram pressure stripping of a disc galaxy*, which has been published in MNRAS (Ramos-Martínez et al. 2018).

Here, 3D numerical simulations were performed for a disc galaxy subject to the ram pressure exerted by the intracluster medium (ICM) when the galaxy travels towards the cluster centre. The magnetohydrodynamic code RAMSES (Teyssier 2002) was used, which is an adaptive mesh refinment (AMR) code. Given that the magnetic field (MF) in the ram pressure stripping (RPS) of disc galaxies has been barely studied (for models with MFs in the ICM see Pfrommer & Dursi 2010 and Ruszkowski et al. 2014, and for models with galactic MFs see Tonnesen & Stone 2014), to better understand the impact of the MF on the gas sweeping off a galaxy, simulations with galactic MF (MHD model) and a pure hydrodynamical model (HD) were performed. The setup consists of a late-type and low-luminosity spiral galaxy, similar to M33, and for this it used an axisymmetric gravitational potential similar to the Allen & Santillán (1991) model, but modified such that it adjust a rotation curve with maximum velocity of $v_{circ} = 110-120\,\mathrm{km\ s^{-1}}$ (Corbelli 2003, for M33). It was modeled an isothermal gaseous disc (with a constant sound speed $c_s \approx 8\,\mathrm{km\ s^{-1}}$) in rotational equilibrium with the gravitational potential, the total pressure gradient (thermal and magnetic pressure) and the magnetic tension, which results in an initial density distribution and $\beta = P_{\mathrm{th}}/(B^2/8\pi)$ parameter as shown in the fig. 2.1. In the HD model, the magnetic pressure and tension are not included. All the non-gaseous components of the galaxies are present in the gravitational potential and the gas is in hydrostatic equilibrium with it. The simulation is setup in a box of size 120 kpc in each direction, with 11 levels of refinement, equivalent to a resolution

of 2048^3 cells. Throughout the chapter, n is the number density ($n = \rho/(\mu m_{\rm H})$[1]). For the MHD model, the galactic magnetic field is initially divided in two regimes: in the central part of the galaxy it has a random distribution and in the disc the field is azimuthal. Finally, to represent the ICM, we worked under the wind-tunnel approximation, where the disc is at rest and the ICM flows as a wind with a constant density $n_{\rm ICM} = 10^{-5}\,{\rm cm}^{-3}$ and an initial velocity that increases linearly in time, from 300 to $\sim 760\,{\rm km\ s}^{-1}$ in a time of $t = 500\,{\rm Myr}$, when the simulations ended.

Including the galactic magnetic field increases the pressure in the vertical (z) direction such that the disc is thicker compared to the HD case (fig. 2.1). Additionally, the magnetized disc has a flaring, which changes the dynamics of the interaction with the wind since there is gas farther away from the galactic disc potential well. When the wind hits the galaxy, at the first 100 Myr, the MHD disc is barely perturbed by the interaction with the wind showing a layer of compressed gas in the disc-wind interface extending at all radii. These are oblique shocks generated due to the flared geometry of the magnetized disc. On the other hand, the HD disc is compressed and rapidly displaced out of the galactic midplane by the wind. As time goes by, at $t = 500\,{\rm Myr}$, the wind accelerates and overcomes the gravitational potential of the galaxy, displacing more and more material out of the disc from the outside-in, although the HD case shows a longest tail with a height of $z \sim 40\,{\rm kpc}$ compared to the MHD one with $z \sim 20\,{\rm kpc}$ and a truncated disc with a size of $r \sim 4\,{\rm kpc}$ and $r \sim 10\,{\rm kpc}$ for the HD and MHD cases, respectively, which means that the HD disc loses its gas faster and more efficiently than the MHD disc. Besides the difference in the stripping rate, it is also observed that the MF alters the morphology of the swept gas, where the MHD tail is smoother, denser and with a broader appearance while the HD one is clumpier and filamentary-like. This is due to the fact that the magnetized gas is less compressible than the pure HD case. The MF also prevents the mixing of the gas with the surroundings, which means that denser gas survives farther from the disc.

To better understand the relation of the stripping with the gas surface density Σ of a galaxy (in the z-direction), an HD model with a Σ similar to the MHD one was performed, which is called the heavy model. The MHD and HD cases have the same initial number density n in the galactic midplane and the same gravitational potential. When solving the equation of hydrostatic equilibrium, the MF changes the compressibility of the gas, thus increasing the surface density Σ that results in a thicker MHD disc. So, in the heavy model, an increase in Σ results in an increased number density ($n_{heavy} = 10 n_{\rm HD}$) at the galactic midplane (fig. 2.1). The evolution of the heavy model shares some properties with the MHD and HD ones, that is, its stripping rate and the truncation radius of its gaseous disc is similar to the MHD, but the shape and structure of its tail, although with a small height above the

[1] $\mu = 1.27$ is the mean particle mass and $m_{\rm H} = 1.67 \times 10^{-24}\,{\rm g}$ is the hydrogen mass

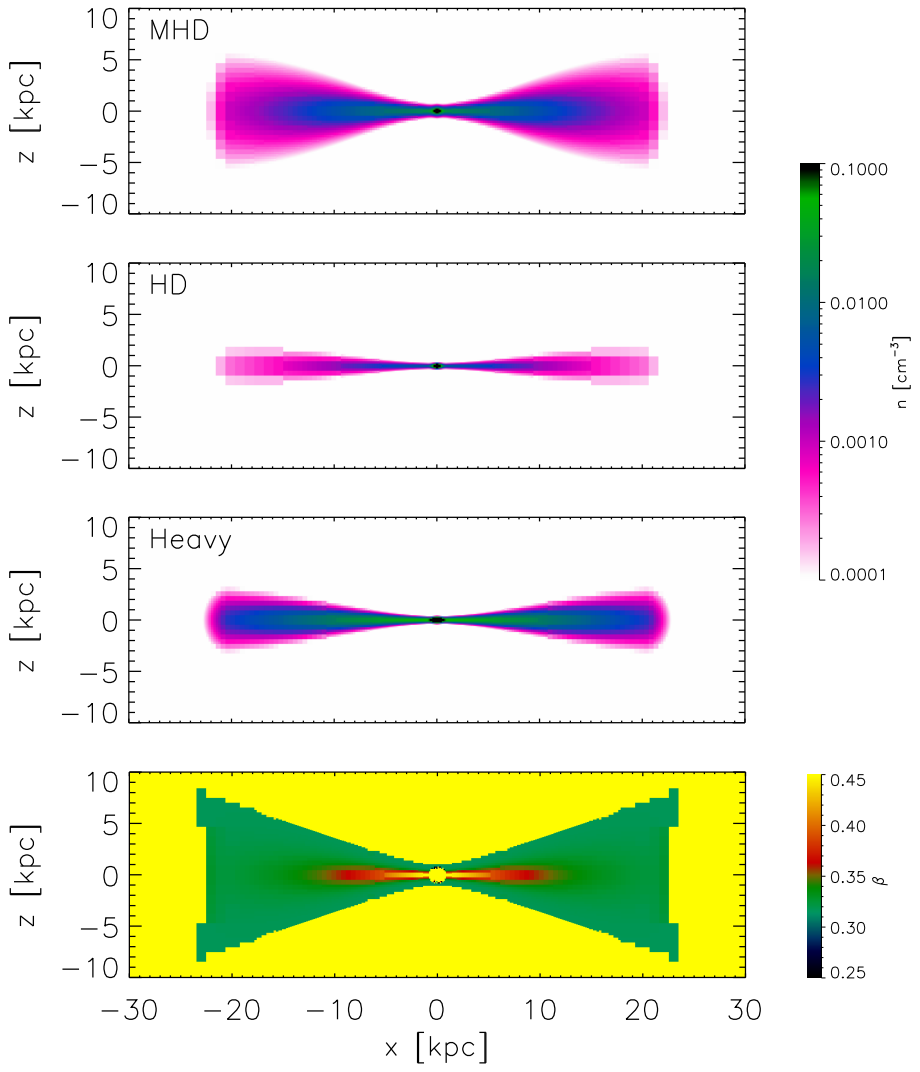

Figure 2.1: From top to bottom: density slices of the initial condition for the MHD (*first row*), HD (*second row*), and heavy (*third row*) models. Initial $\beta = P_{\rm th}/(B^2/8\pi)$ parameter (*bottom*). All images are slices at the $y = 0$ plane.

galactic disc, resembles the HD model.

Other feature observed in the MHD model is that when the ICM wind first hit the disc, at the disc-wind interface, the flared geometry of the galaxy produces oblique shocks which generate an inflow of gas from the outskirts towards the central parts of the galaxy. This motion of gas is present in the early stages of evolution of the simulation, lasting $\sim 150\,\mathrm{Myr}$. The inflow of gas derived from the oblique shocks may replenish the central parts of the galaxy with the material for star formation or to possibly ignite nuclear activity before the gas is removed by the ram pressure, since the estimated time of the inflow is comparable to the duty cycle of the active galactic nuclei (AGN) which is $10 - 100\,\mathrm{Myr}$ (Haehnelt & Rees 1993). However, other tests need to be performed to study the funnelling of gas towards the centre of the galaxy, such as different wind profiles and angles, disc surface densities and flare strengths.

Monthly Notices of the ROYAL ASTRONOMICAL SOCIETY

MNRAS **476,** 3781–3792 (2018) doi:10.1093/mnras/sty393
Advance Access publication 2018 February 16

MHD simulations of ram pressure stripping of a disc galaxy

Mariana Ramos-Martínez,[1]★ Gilberto C. Gómez[1] and Ángeles Pérez-Villegas[2,3]

[1] *Instituto de Radioastronomía y Astrofísica, Universidad Nacional Autónoma de México, Apdo. Postal 3-72, Morelia, Michoacan 58089, Mexico*
[2] *Max-Planck-Institut für Extraterrestrische Physik, Gießenbachstraße, D-85741, Garching, Germany*
[3] *Universidade de São Paulo, IAG, Rua do Matão 1226, Cidade Universitária, Sao Paulo 05508-900, Brazil*

Accepted 2018 February 12. Received 2018 February 12; in original form 2017 March 24

ABSTRACT

The removal of the interstellar medium (ISM) of disc galaxies through ram pressure stripping (RPS) has been extensively studied in numerous simulations. Nevertheless, the role of magnetic fields (MFs) on the gas dynamics in this process has been hardly studied, although the MF influence on the large-scale disc structure is well established. With this in mind, we present a 3D magnetohydrodynamic simulation of face-on RPS of a disc galaxy to study the impact of the galactic MF in the gas stripping. The main effect of including a galactic MF is a flared disc. When the intracluster medium wind hits this flared disc, oblique shocks are produced at the interaction interface, where the ISM is compressed, generating a gas inflow from large radii towards the central regions of the galaxy. This inflow is observed for ∼150 Myr and may supply the central parts of the galaxy with material for star formation while the outskirts of the disc are being stripped of gas, thus the oblique shocks can induce and enhance the star formation in the remaining disc. We also observed that the MF alters the shape and structure of the swept gas, giving a smooth appearance in the magnetized case and clumpier and filamentary-like morphology in the hydro case. Finally, we estimated the truncation radius expected for our models using the Gunn–Gott criterion and found that that is in agreement with the simulations.

Key words: MHD – galaxies: evolution – galaxies: individual: NGC 598 – galaxies: ISM – galaxies: magnetic fields.

1 INTRODUCTION

Lenticular galaxies (S0s) are objects that lie between the elliptical and spiral galaxies in the Hubble sequence. The S0s share properties with both types of galaxies, that is, an old stellar population like ellipticals and stellar discs like spirals. Lenticulars also have prominent bulges (Simien & de Vaucouleurs 1986), low gas content (Gallagher, Faber & Balick 1975), and some observations show that the last star formation episode took place at the bulge (Sil'chenko 2006; Prochaska Chamberlain et al. 2011; Bedregal 2012; Johnston et al. 2012; Sil'chenko et al. 2012; Johnston, Aragon-Salamanca & Merrifield 2014, but see Katkov, Kniazev & Sil'chenko 2015).

The well-studied environmental density–galactic morphology relationship in clusters of galaxies (Dressler 1980) states that late-type galaxies (spirals) are more frequently found in the outskirts of clusters, while early-type galaxies (ellipticals and S0s) are more abundant in the central regions. In the case of groups of galaxies, a similar trend has been observed (Postman & Geller 1984). Additionally, in cluster galaxies, the fraction of spirals increases with increasing redshift z, whilst the S0s fraction decreases (Dressler et al. 1997; Fasano et al. 2000). On the other hand, when properties of spiral galaxies in clusters and those in the field are compared (Boselli & Gavazzi 2006 and references therein), cluster spirals are H I deficient and such deficiency increases towards the cluster centre. Also, cluster galaxies show a lower star formation rate (SFR) associated with the lack of H I, and they are redder than field galaxies, which indicate the former form stars passively (Butcher & Oemler 1978). Late-type galaxies also follow more radially elongated orbits than early-type, suggesting they are free-falling into the cluster (Dressler 1986; Giraud 1986; Vollmer et al. 2001; Biviano & Katgert 2004; Aguerri et al. 2017). Lastly, cluster galaxies show an increase in radio-continuum emission, probably due to an enhancement in the magnetic field (MF) intensity, possibly caused by compression (Scodeggio & Gavazzi 1993; Rengarajan, Karnik & Iyengar 1997).

These observations point to one or more mechanisms that act in the environment of clusters and groups, stripping the galactic interstellar medium (ISM) from the discs or increasing its consumption rate so that the star formation shuts down and a change in disc colour is produced. Therefore, the idea that spirals are the progenitors of S0s has been proposed, suggesting that the study of S0s may help us understand the impact of environment on the evolution of disc galaxies.

★ E-mail: m.ramos@irya.unam.mx

© 2018 The Author(s)
Published by Oxford University Press on behalf of the Royal Astronomical Society

Downloaded from https://academic.oup.com/mnras/article-abstract/476/3/3781/4867983 by Universidad Nacional Autonoma de Mexico user on 14 September 2018

In clusters, the main mechanisms proposed to explain the transformation of a spiral galaxy into an S0 are as follows:

(i) Ram pressure stripping (RPS; Gunn & Gott 1972): When a galaxy falls into the cluster centre, the hot intracluster medium (ICM) exerts an hydrodynamic (HD) pressure on the ISM of the galaxy and, if this pressure exceeds the gravitational force of the disc [Gunn–Gott criterion (GG)], then the ISM is stripped off the galaxy.

(ii) Galaxy harassment (Moore et al. 1996): Close and frequent encounters between galaxies occurring at high velocities, at a rate of one encounter per 1 Gyr, may increase the SFR, rapidly exhausting the gas supply and eventually leading to a redder disc. These interactions will alter the galactic morphology by dynamically heating the disc.

(iii) Starvation (Larson, Tinsley & Caldwell 1980): The galaxy loses the envelope of hot gas that supplies the disc's gas reservoir, so the ISM is consumed and the star formation shuts down.

There are also other mechanisms that may act in groups of galaxies that can modify the galactic morphology, such as tidal interactions (Icke 1985) and major (Toomre & Toomre 1972; Borlaff et al. 2014) and minor mergers (Aguerri, Balcells & Peletier 2001; Tapia et al. 2014). Nevertheless, these processes are not exclusive, that is, more than one might operate at the same time. Comparing these mechanisms, Boselli & Gavazzi (2006) conclude that RPS is the most appropriate to explain the differences observed in between spirals of clusters and those in the field, since RPS removes the gas from the galaxies producing a change in the SFR and colour. Also, RPS is efficient and inevitable near the cluster centre and may alter indirectly the morphology of the discs (if a galaxy loses its gas, the stellar disc is dynamically heated, leading to a thicker disc, Farouki & Shapiro 1980; Sellwood & Carlberg 1984; Fuchs & von Linden 1998; Bekki, Couch & Shioya 2002; Elmegreen et al. 2002).

Multiwavelength observations have shown several cluster galaxies that are good candidates to be experiencing RPS (Koopmann & Kenney 2004; Chung et al. 2009; Yagi et al. 2010; Bekki 2014; Boselli et al. 2014; Kenney et al. 2014), since they show truncated gaseous discs and in some cases gas tails, while the stellar disc remains unperturbed. Cayatte et al. (1990) performed a survey of H I for spiral galaxies in the Virgo Cluster where they found that small H I discs lie almost exclusively in the cluster centre in galaxies with high velocities with respect to the cluster mean velocity, which makes it possible that they lost their gas through RPS. Moreover, they observed that galaxies affected by RPS have shown nuclear activity. This could be since the gas pushed to the centre of the galaxy and the compression exerted by the ICM enhances the star formation. Also, Poggianti et al. (2016) presented an atlas of galaxies at low redshift that are being stripped of their ISM, with candidates found at all cluster centric distances that showed an enhanced SFR compared to non-candidates of the same mass. This points to the idea that RPS can induce and enhance the star formation.

A good example of a galaxy subject to RPS is NGC 4522 in the Virgo cluster. This is the most studied case of a galaxy losing its ISM by this mechanism (Vollmer et al. 2000, 2004, 2006, 2008; Abramson & Kenney 2014; Abramson et al. 2016; Stein et al. 2017) and is possibly in the process of transforming into an S0, since it shows a truncated disc in H I with a 3 kpc radius and a ∼3 kpc-length gas tail observed in H I (Kenney, van Gorkom & Vollmer 2004) and Hα (Kenney & Koopmann 1999). Also, in the Abell 3627 cluster, the galaxy ESO 137-001 is stripped by the hot ICM (Sun, Jones & Forman 2006; Sun, Donahue & Voit 2007; Sivanandam, Rieke & Rieke 2010; Fumagalli et al. 2014; Jáchym et al. 2014; Fossati et al. 2016). ESO 137-001 presents an 80 kpc long, double X-ray gas tail (Sun et al. 2006), with some H II regions embedded within the tail (Sun et al. 2010), indicating that star formation can go on within the ISM stripped out of the galaxy. Later, in the same cluster, another X-ray gas tail was detected (ESO 137-002), with a double Hα tail (Zhang et al. 2013).

The ICM–ISM interaction through the RPS has been studied extensively for years. A wide variety of models have been developed with different methods and techniques. The first models were performed under the assumption of a constant ICM wind, using smoothed particle hydrodynamics (SPHs; Abadi, Moore & Bower 1999; Schulz & Struck 2001) and grid codes (Quilis, Moore & Bower 2000; Roediger & Hensler 2005; Roediger & Brüggen 2006; Roediger, Brüggen & Hoeft 2006). These models were in good agreement with the Gunn–Gott estimation for the disc truncation radius. Other simulations were done varying the inclination angle of the disc with respect to the wind direction (Roediger & Brüggen 2006; Vollmer et al. 2006; Jáchym et al. 2009). Yet other models added a variable ICM wind, so the RPS mechanism is not constant (Vollmer et al. 2001; Roediger & Brüggen 2007, 2008, with a sticky-particle code). Another extension to the RPS models included a multiphase gas disc (Quilis et al. 2000; Tonnesen & Bryan 2009, 2010), where the low-density gas is stripped more easily from the galaxy, but the mass loss of the ISM is not so different from homogeneous disc models. Some other works included star formation, which showed an increase in the star formation in central regions of the target galaxies (Schulz & Struck 2001; Vollmer et al. 2001) and sometimes stars were formed in the gas tails (Bekki & Couch 2003; Kapferer et al. 2008; Kronberger et al. 2008; Steinhauser et al. 2012; Tonnesen & Bryan 2012).

Despite the huge variety of RPS models, there are very few including MF. MFs have been observed in galaxies from polarized emission, mainly in radio frequencies and Faraday rotation. MFs in spirals have an ordered component, i.e. with a constant and coherent direction, and a random or turbulent component that has been amplified and tangled by turbulent gas flows (Beck 2005; Beck & Wielebinski 2013, and references therein). Combining information obtained with different techniques, it is possible to develop a model for the 3D structure of MF in galactic discs. In spirals, the average total field strength is ∼9 μG (Niklas 1995) and the regular field strength is 1–5 μG (Beck & Wielebinski 2013); in radio-faint galaxies like M31 and M33, the total field is 6 μG (Tabatabaei et al. 2008; Gießübel 2012); in gas-rich spiral galaxies, the total field is 20–30 μG (Fletcher et al. 2011; Frick et al. 2016); for bright galaxies, the total field is ∼17 μG (Fletcher 2010); in blue compact dwarf galaxies, the total field is 10–20 μG (Klein, Weiland & Brinks 1991); and the strongest total fields are found in starburst and barred galaxies with 50–100 μG (Chyży & Beck 2004; Beck et al. 2005; Adebahr et al. 2013). Since the degree of polarization on average is low in the spiral arms, the random field is assumed to be stronger, up to five times the intensity of the ordered field, whilst in the interarm region the degree of polarization is higher, hence the ordered field should dominate. Additionally, it has been observed that the ordered MF shows a spiral pattern that is offset from the spiral arms of gas and stars (Beck 2005).

Ruszkowski et al. (2014) presented simulations of RPS with a magnetized ICM and found that the MF can affect the morphology of the stripped gas tail, since they observed narrower tails than in purely HD simulations. Pfrommer & Dursi (2010) also showed magnetohydrodynamics (MHDs) simulations in which the galaxies are moving in a magnetized ICM. The galaxies in their simulations

Downloaded from https://academic.oup.com/mnras/article-abstract/476/3/3781/4867983 by Universidad Nacional Autonoma de Mexico user on 14 September 2018

swept the field lines where polarized radiation is generated. This is used to map the orientation of the MF in clusters, e.g. Virgo cluster. In these cases, the MF has been implemented only in the ICM and not in the discs. Some examples of models with magnetized discs are Vollmer et al. (2006, 2007); Soida et al. (2006), where they used the method of Otmianowska-Mazur & Vollmer (2003) where the MF is evolved via the induction equation using a grid code with the velocity field of the particles, so that the MF is advected with the gas. These simulations of RPS have been carried out first with a sticky particle code, and then a toroidal configuration of the MF is given to the galaxy. Even if the effect of the MF over the gas dynamics has not been taken into account, this method has been useful to explain the polarized radiation in radio that is observed in some galaxies that may be affected by the RPS, as in the case of NGC 4522 (Vollmer et al. 2006).

Additionally, Tonnesen & Stone (2014) performed MHD simulations for the RPS including galactic MF, but the ICM was not magnetized. They found that MFs do not alter or dramatically change the stripping rate of the gas disc compared to pure HD simulations. Nevertheless, the MFs have an impact in the mixing of gas throughout the tail, since inhibits the mixing of the gas tail with the ICM, the unmixed gas survives at large distances from the disc. Besides, the RPS may help magnetize the ICM up to a few μG.

Here, we present MHD simulations of RPS of a disc galaxy under the wind-tunnel approximation, for a face-on geometry. Additionally, we performed two purely HD runs to compare with the magnetized case and analyse the impact that the galactic MF has in the stripping of the disc. In Section 2, we present the initial set-up for the simulations. In Section 3, we describe the resulting gas and MF distribution, and in Section 4 we discuss our conclusions.

2 MODEL

We set up a magnetized disc in rotational equilibrium in a fixed gravitational potential. We used the MHD code RAMSES (Teyssier 2002), which is an adaptive mesh refinement code, so we can have more refinement of cells in the desired regions, and allows us to add MF in the simulations. The models were performed in 3D with 11 refinement levels, for a resolution equivalent to $(2048)^3$ cells, in a box of 120 kpc in each direction.

2.1 Initial conditions

The gravitational potential used for our galaxy is based on the model of Allen & Santillán (1991), which is an analytic and simple potential that can reproduce the rotation curve of the Milky Way and is composed by a spherical central bulge, a Miyamoto–Nagai disc, and a massive spherical halo. This potential model can be easily modified to approximate the rotation curves of other galaxies. For this work, we modelled an M33-like galaxy, which is a late type and low-luminosity spiral galaxy. We modified the mass and scale parameters to the values shown in Table 1 to model the rotation curve of the M33 galaxy (see Fig. 1, solid line) as reported by Corbelli (2003). Nevertheless, for the simulations presented in this work, we removed the galactic bulge component of the potential ($M_1 = 0$) since it generated a large potential gradient in the z-direction (perpendicular to the galactic disc) for small radii that generated problems for our initial set-up procedure (described below). Regardless, this should have little impact on our conclusions, specially since the M33 bulge's mass is small. The velocity profile used for the simulations, both with and without MFs, is also presented in Fig. 1.

Table 1. Length scale and mass parameters of the gravitational potential, as adjusted to approximate M33's rotation curve. M_1 and M_2 represent the total mass of the bulge and disc, respectively, while M_3 is a mass factor for the halo, where its total mass is obtained up to a cut-off radius.

Bulge	$M_1 = 1.39 \times 10^9 M_\odot$
	$b_1 = 0.85$ kpc
Disc	$M_2 = 1.62 \times 10^{10} M_\odot$
	$a_2 = 3.0$ kpc
	$b_2 = 1.0$ kpc
Halo	$M_3 = 6.96 \times 10^{10} M_\odot$
	$a_3 = 16.0$ kpc

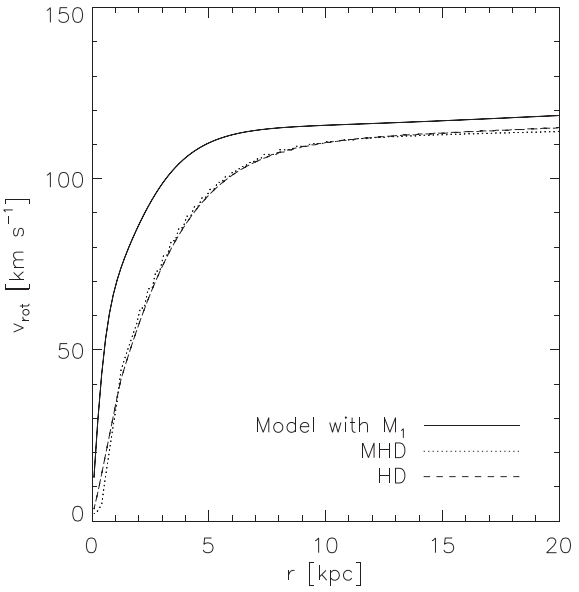

Figure 1. Rotation curve for the M33-like galaxy obtained from the gravitational potential with the values from Table 1 (solid line) and velocity profile for the MHD (dotted line) and the HD (dashed line) simulations without the bulge contribution ($M_1 = 0$).

For the initial conditions, we use a method similar to Gómez & Cox (2002). First, we define the radial density and velocity profile in the galactic mid-plane, assuming that the gas disc is in rotational equilibrium with the gravitational force, the total pressure gradient, and the magnetic tension:

$$\frac{v_\phi^2(r,z)}{r} = \frac{\partial \Phi}{\partial r} + \frac{1}{\rho(r,z)}\left[\frac{\partial P}{\partial r} + \frac{2P_{\rm B}(r,z)}{r}\right], \quad (1)$$

where the total pressure P is the sum of the thermal ($P_{\rm th} = c_{\rm s}^2 \rho(r,z)$, with $c_{\rm s}$ the sound speed) and the magnetic ($P_{\rm B}$) pressures. The magnetic pressure has two components: $P_{\rm B} = P_{\rm B,\,inner} + P_{\rm B,\,outer}$, with

$$P_{\rm B,inner} = P_{\rm B0}\left[1 - {\rm erf}\left(\frac{R}{r_{\rm b}}\right)\right] \quad \text{and} \quad (2)$$

$$P_{\rm B,outer} = \frac{P_{\rm B0}\, n}{(n + n_{\rm c})}, \quad (3)$$

where $R = \sqrt{r^2 + z^2}$, $r_{\rm b} = b_1/3$ (see Table 1), $P_{\rm B0} = 1.75 \times 10^{-13}$ dyn cm^{-2}, and $n_{\rm c} = 0.04$ cm^{-3}. With these expressions for

Downloaded from https://academic.oup.com/mnras/article-abstract/476/3/3781/4867983 by Universidad Nacional Autonoma de Mexico user on 14 September 2018

the total pressure and equation (1), a given mid-plane density (or velocity) profile uniquely defines the velocity (density) profile. In the bulge, the rotation curve resembles a rigid body, and so we define the rotation velocity linearly increasing with radius

$$v_\phi(r,0) = v_\phi(b_1,0)\left[\frac{r}{b_1}\right], \tag{4}$$

where $v_\phi(b_1, 0)$ is the circular velocity obtained from the gravitational potential in $r = b_1$ and $z = 0$. Then, the density profile in the mid-plane is given by

$$\frac{\partial\rho}{\partial r} = \frac{\rho\left(v_\phi^2 - \partial\Phi/\partial r\right) + (P_{\rm B0}/r_{\rm b})\,e^{-(R/r_{\rm b})^2}}{\left[c_{\rm s}^2 + P_{\rm B0}\rho_{\rm c}/(\rho+\rho_{\rm c})^2\right]}, \tag{5}$$

which is integrated from $r = 0$ to b_1.

For $r > b_1$ we do the converse: we define the density profile as exponentially decreasing at the mid-plane:

$$\rho(r,0) = \rho_0 \exp[-(r-b_1)/h_r],$$

where $h_r = 6$ kpc and ρ_0 is the value found at $r = b_1$ from equation (5).

Once the mid-plane density is calculated, the distribution at $z \neq 0$ is found by assuming magnetohydrostatic equilibrium and an isothermal equation of state

$$\frac{\partial P}{\partial z} = -\rho\,\frac{\partial\Phi}{\partial z}, \tag{6}$$

where again $P = P_{\rm th} + P_{\rm B}$. By substituting the magnetic pressure components (equations 2 and 3) and the equation of state it follows

$$\frac{\partial\rho}{\partial z} = \frac{-\rho\partial\Phi/\partial z + (P_{\rm B0}/r_{\rm b})\exp\left[-(R/r_{\rm b})^2\right]}{\left[c_{\rm s}^2 + P_{\rm B0}\rho_{\rm c}/(\rho+\rho_{\rm c})^2\right]}, \tag{7}$$

which is integrated along the z coordinate to obtain the vertical density profile at any radius r.

The rotation velocity above the mid-plane is given by (Gómez & Cox 2002)

$$v_\phi^2(r,z) = v_\phi^2(r,0) - v_{\rm A}^2(r,0) + v_{\rm A}^2(r,z), \tag{8}$$

where $v_{\rm A}$ is the Alfvén velocity ($v_{\rm A} = \sqrt{2P_{\rm B}/\rho}$).

Fig. 2 shows a density map for the initial condition of the disc at $y = 0$, both for a magnetized and a purely HD ($P_{\rm B0} = 0$) cases. It can be seen that, for the magnetized case, the disc is thicker in the outskirts than in the central region, that is, the galactic disc flares in the presence of the MF. Additionally, the scale height of the MHD disc is larger than in HD one. When solving the equation of hydrostatic equilibrium, the MF changes the compressibility of the gas, thus increasing the surface density Σ for the gravitational potential and mid-plane density used, which results in a heavier disc compared to the HD model. For this reason, we performed another HD simulation with surface density similar to that in the magnetized disc model. We will refer to this as the heavy disc model. To obtain the density distribution of the heavy disc, we solve again the equations (5) and (7), increasing the initial value of ρ one order of magnitude over original HD model, thus increasing $\rho_{\rm HD}(z = 0)$ results in $\Sigma_{\rm heavy} \sim 1.5\Sigma_{\rm MHD}$. The initial density distribution for the heavy model is also presented in Fig. 2.

2.2 Galactic magnetic field

In the set-up described above for the MHD model, the MF has two components (equations 2 and 3). While the outer component ($r > b_1$) is purely toroidal, the inner one is random. For the random

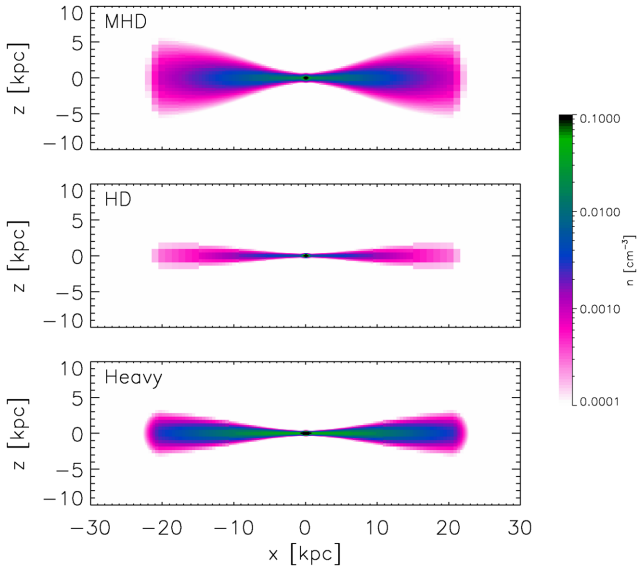

Figure 2. Density slices of the initial condition for the MHD (*top*), the HD (*centre*), and the heavy (*bottom*) models. Colours show the gas number density at the $y = 0$ plane.

inner component ($r < b_1$), we defined the vector potential $\boldsymbol{A}$ with

$$A_{\rm x} = A_0 \cos\phi_r \,\sin\theta_r\, f(z), \tag{9}$$

$$A_{\rm y} = A_0 \sin\phi_r \,\sin\theta_r\, f(z), \tag{10}$$

$$A_{\rm z} = A_0 \cos\theta_r\, f(z), \tag{11}$$

where the angles ϕ_r and θ_r were obtained randomly and A_0 is drawn from a normal distribution with dispersion equal to $\sqrt{8\pi P_{\rm B0}}$.

The function $f(z) = \mathrm{sech}^2(z/z_{\rm h})$, with $z_{\rm h} = 150$ pc, modulates the vector potential so its magnitude has the same scale height as the density in the bulge. Once the components for the vector potential are calculated, it is smoothed in order to avoid large fluctuations. Finally, the MF is calculated as $\boldsymbol{B}_{\rm inner} = \boldsymbol{\nabla} \times \boldsymbol{A}$. For the rest of the disc ($r > b_1$), the MF in the set-up follows a toroidal configuration, with its strength given by the gas density (equation 3). Fig. 3 shows the initial intensity of the MF with arrows overlaid representing the field lines for the MHD model.

2.3 ICM wind

To simulate the ICM–ISM interaction, we worked under the wind–tunnel approximation, that is, we place the galaxy at rest and the ICM flows towards the disc face-on. The ICM wind is unmagnetized and has the same parameters for all models: the wind starts at $z = -10$ kpc and moves in the $+z$-direction with density $n_{\rm ICM} = 10^{-5}$ cm^{-3} and a velocity that increases linearly in time, from 300 to 760 km s^{-1} at the end of the simulation, at 500 Myr. All the computational boundaries are outflowing, except at the bottom where the wind flows inward.

3 RESULTS

3.1 Model evolution

Fig. 4 shows the evolution of the models: the magnetized and both HD and heavy hydro models, in maps of projected density. The first

Downloaded from https://academic.oup.com/mnras/article-abstract/476/3/3781/4867983 by Universidad Nacional Autonoma de Mexico user on 14 September 2018

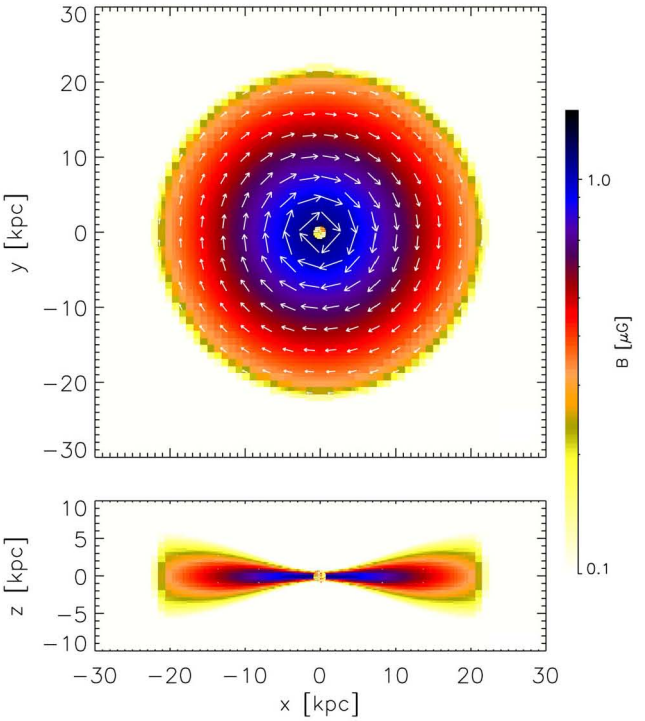

Figure 3. Slices of the MF intensity for the MHD model at the initial condition in a $z = 0$ (top) and $y = 0$ (bottom) cut. The MF strength is colour-coded in log-scale.

row corresponds to a time $t = 90$ Myr. It can be seen that the wind is starting to interact with the discs. In the MHD run (left column), oblique shocks appear on the side of the disc that is facing the ICM wind (at $z < 0$), because our disc flares in the presence of the galactic MF, giving it a 'bow tie' shape. The oblique shocks lead gas of the external parts of the disc towards the galactic centre and continues for another ∼150 Myr more until the ICM wind finally surpasses the gravitational force of the disc and starts to sweep the ISM (see Section 3.3). Since the HD disc (central column) does not flare as much as the MHD one, the ISM–ICM interaction is different. At 90 Myr, in the HD model the wind perturbs the gaseous disc and displaces it from the $z = 0$ mid-plane. The background gravitational force pulls back the gas to its original position, mainly in the inner region of the disc, whilst the outer parts of the disc are still being swept by the wind. In the heavy model, most of the gas disc initially at $z < 0$ is compressed and moved by the wind to a height $z \sim 0$, changing the disc symmetry but to a smaller extent than in the HD case.

At $t = 190$ Myr (second row), for the MHD run, most of the gas that lay below the galactic mid-plane was swept by the wind which in turn starts to erode the disc at large radii, where the ram pressure exceeds the gravitational force of the galaxy (see Section 3.2). The inner region of the disc ($r < 5$ kpc) is slightly perturbed, with small variations in the z direction, since the gravitational force tries to keep the disc in the equilibrium position. As a result, the gas moves up and down. These fluctuations in z at small radii occur at earlier times in the HD model but it is basically the same behaviour: gas at large r is swept by the wind whilst the gas located near the galactic centre remains bound to the disc. The displaced gas reaches a height of ∼5 and ∼10 kpc above the galactic mid-plane, for the MHD and HD case, respectively. The HD model shows a larger erosion than the MHD, with a gaseous disc of radius $r < 5$ kpc for the HD run, and $r \sim 20$ kpc for the MHD one. The gas of the heavy disc has moved just a few kpc from the mid-plane, showing almost the same radial extension as the MHD, although the heavy disc is denser near the galactic mid-plane.

After 310 Myr of evolution, the wind continues flowing and accelerating towards the disc and reaches $v_{\rm ICM} \sim 550$ km s^{-1} at $z = 0$. For the magnetized disc (third row, left), the gas at $r > 10$ kpc is ripped off of the galaxy, where the ram pressure is stronger than the galactic gravitational force. The swept gas has increased its height, reaching $z \sim 10$ kpc. There are still some vertical motions in the mid-plane for $r < 10$ kpc because the gas in this position is adjusting to the balance between the pressure from the wind and the gravitational force in the disc. This process is also present in the HD run, but the oscillating gas is contained in a smaller radius ($r < 7$ kpc). Additionally, for the HD model, the gas that has been removed from the disc has reached a height of ∼20 kpc above the disc mid-plane. Compared to the magnetized case, the stripped gas has a more diffuse appearance in the HD run, that is, the gas mixes easier with the surrounding, and it is less extended in the radial direction than the MHD case. The HD disc is, at this time, truncated to a radius of ∼6 kpc. The heavy disc at $t = 310$ Myr shows a structure similar to the MHD one: the heavy disc has a radial extension of $r \sim 10$ kpc in the mid-plane, while in the vertical direction the denser gas reaches a height of $z \sim 5$ kpc, but the less dense gas is farther away the galactic mid-plane in the MHD model ($z \sim 10$ kpc).

At $t = 500$ Myr, the wind has a velocity of ∼760 km s^{-1} at $z = 0$ for all cases. In the MHD model, the stripped gas reaches a height of ∼20 kpc above the galactic mid-plane. The disc has been truncated to a radius of ∼10 kpc, which is approximately half of its original size. The dimensions of the displaced gas for the MHD model resemble the one from the HD at $t = 310$ Myr, showing a similar longitude over the mid-plane, which suggests that the evolution of the MHD simulation is delayed with respect to the HD run, although differences remain in the morphology: in the MHD case, the swept gas has a smooth appearance and is denser at higher z than in the HD case, which indicates that the MF prevents the gas from mixing with the surroundings, similarly as seen in Tonnesen & Stone (2014). On the other hand, the HD model with 500 Myr of evolution shows a more filamentary and clumpier morphology in the stripped gas, contrary to the smooth appearance that the magnetized gas presents. The HD gas is extended over ∼40 kpc above $z = 0$, and the remaining disc has radius of ∼4 kpc, which indicates that this disc has reached a state of equilibrium with the ram pressure, since the gas was rapidly eroded in the first ∼200 Myr of evolution and the remaining gaseous disc (in $z = 0$) has the same radial extension until the end of the simulation. The heavy disc has a size similar to the MHD ($r \gtrsim 10$ kpc) in the mid-plane ($z = 0$), suggesting that the stripping rate for both discs is approximately the same, whilst the displaced gas for the heavy model has a lower z-height. Nevertheless, when the heavy and HD simulations are compared, the displaced gas of the heavy model resembles the HD case, in that both have a clumpy and filamentary-like structure, with the difference that, in the heavy model, the swept gas is denser because of the initial condition of the gas disc, that is $\rho_{\rm heavy} > \rho_{\rm HD}$ ($\Sigma_{\rm heavy} > \Sigma_{\rm HD}$) as mentioned in Section 2.1, which also results in a slower erosion of the disc.

Comparing the evolution of the three models, the MHD and heavy model are left with a similar remnant disc, with radius $r \sim 10$–12 kpc, which is larger than the HD model ($r \sim 4$ kpc) for the same time of evolution. Our results suggest that the stripping rate depends on the MF only through the surface density Σ of the disc:

Downloaded from https://academic.oup.com/mnras/article-abstract/476/3/3781/4867983 by Universidad Nacional Autonoma de Mexico user on 14 September 2018

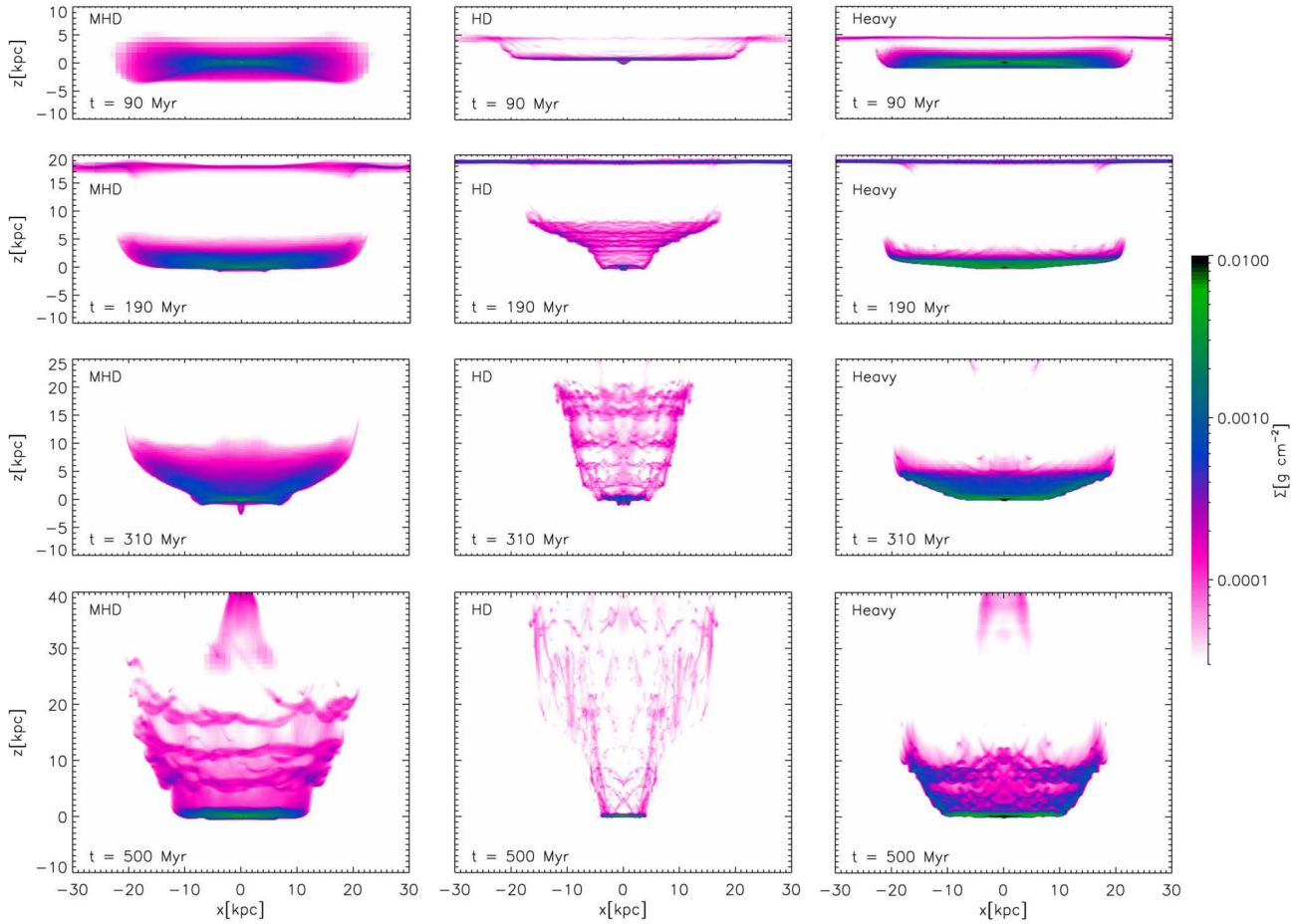

Figure 4. Projected density of the gas along the *y*-axis for the MHD (*left column*), HD (*centre*), and heavy (*right column*) runs. Each row corresponds to times $t = 90$, 190, 310, and 500 Myr. The ICM wind moves up from bottom of the computational grid. Please note that the *z*-axis limits are different for each time shown.

a heavier disc (high Σ) is more difficult to erode since the ICM has more material to sweep, even when the gas is farther away from the gravitational potential well, and thus less bound to the galaxy. This is similar to the results presented by Tonnesen & Stone (2014), where the MHD and HD discs with the same initial mass do not show a significant difference in the stripping rate. Although the heavy model agrees quite well with the MHD in the rate at which the gaseous disc is removed and the truncation radius (see Section 3.2), the problem with the heavy disc is that it gives a higher and unrealistic volumetric density ρ in the galactic mid-plane, because in the absence of the MF, using the same potential to solve the hydrostatic requires a high value of ρ to obtain the same Σ of the magnetized case. Nevertheless, this heavy model is useful to investigate the dependence of the stripping with the disc surface density.

It is observed in our models that the MF has an impact in the morphology and shape of the swept gas. In the magnetized case, the swept gas shows a smooth structure with denser gas surviving at higher *z*, similar to the results of Tonnesen & Stone (2014); while in the two non-magnetized models, the gas located above the mid-plane has a clumpy and filamentary shape. The morphology of the swept gas in the HD and heavy models is due to the equation of state of the gas. In the case where an isothermal equation of state is implemented, like in the set-up we presented, the gas is more compressible compared to an adiabatic or magnetized gas (with an adiabatic index $\gamma > 1$). In our isothermal models, when the wind hits the galaxy, the gas disc is compressed so that clump-like regions form, leading to the development of eddies due to instabilities in the gas and when the eddies are pushed upwards by the wind they generate a tail. This behaviour of the gas is similar to the flow of the cigarette smoke, giving the filamentary and clumpy shape to the swept gas in our HD simulation.

It is noticeable that, in some aspects, the swept gas in our MHD model resembles the H I distribution of the spiral galaxy NGC 4522, a galaxy considered a classic example of RPS (see the Fig. 2 from Kenney et al. 2004): the H I distribution is asymmetric with respect to the stellar disc, is cap shaped, the gas contours are compressed in the upstream side, and it is concave or curved to the downstream side. On the other hand, the stripped gas is not as far from the NGC 4522 disc as the gas distribution in our MHD model at $t = 500$ Myr.

3.2 Gunn–Gott criterion

The GG criterion (Gunn & Gott 1972) estimates the radius at which a disc galaxy, experiencing the ram pressure face-on, will be truncated. This is determined by equalizing the ram pressure $P_{\rm ram} = \rho_{\rm ICM} v_{\rm ICM}^2$ exerted by the wind and the gravitational restoring force in the disc, which is the product of the gravitational force of the galaxy and the surface density of the gas disc $F(r)\Sigma(r)$, that is, the truncation radius is defined by the position where $P_{\rm ram} = F(r)\Sigma(r)$.

Downloaded from https://academic.oup.com/mnras/article-abstract/476/3/3781/4867983 by Universidad Nacional Autonoma de Mexico user on 14 September 2018

3.2.1 *Disc surface density*

In order to verify that our simulations satisfy the GG criterion, we estimate the truncation of our discs measuring the surface density in the z-direction. We did these calculations over time also to study the differences in the stripping rate for the three models. Fig. 5 shows the evolution of the disc surface density (Σ) over time obtained for $|z| \leq 5$ kpc, for the MHD model, and $|z| \leq 3$ kpc for the HD and heavy discs. The differences in the Σ integration range in the z-direction are due to the different thickness of the MHD with respect to the HD and the heavy ones. We define the truncation radius as the one where Σ decays abruptly. At $t = 90$ Myr, the discs are barely perturbed, as can be seen by comparing with Fig. 4, and their surface density distribution is similar to the initial condition: the surface density decreases slowly in r, and decays rapidly at $r \sim 21$–22 kpc, except for the MHD disc where the decay is less abrupt. Given that in the MHD case Σ decreases approximately two orders of magnitude (10^{-4}–10^{-6} gr cm^{-2}) in $r > 20$ kpc, to obtain the truncation radius of the disc we took the mid-point for this range of densities, in the log-scale, and then we found the value of r where we have this density ($\Sigma = 10^{-5}$ gr cm^{-2}), giving $r \sim 23$ kpc. As mentioned before (see Fig. 2), the MHD disc has a higher surface density than the HD disc by approximately one order of magnitude due to the extra support that the MF provides. By construction, the heavy disc has a value of $\Sigma_{\rm heavy} \sim 1.5\Sigma_{\rm MHD}$ (see Section 2.1), but the decay of $\Sigma_{\rm heavy}$ is more abrupt than the MHD case and lies between the range of $r = 21$–22 kpc, similarly to the HD model. At $t = 190$ Myr, the surface density in the inner MHD disc is still similar to the previous snapshot, but Σ decreases more rapidly with radius than at 90 Myr, resulting in a disc with $r \sim 19$ kpc, which is a clear sign that the ICM has started to erode the gas of the disc. At this same time, for the HD run, the disc has been eroded more efficiently than the magnetized one, with $\Sigma_{\rm HD}$ showing an abrupt drop at $r \sim 6$ kpc. The heavy disc shows a truncation radius of $r \sim 20$ kpc and is also evolving similarly to the MHD run.

When the simulations have reached a time of 310 Myr, it is clear to see that the surface density profile has changed for the MHD and heavy discs, due to the accelerating wind that swept the gas of these galaxies. This is observed in the fall of the density and the smaller radial extension of the discs, which have been reduced considerably to $r \sim 15$ kpc for the MHD and heavy models. The HD model evolves faster in time than the other models, as expected, since most of its disc was swept at earlier times ($t = 190$ Myr), presenting a gaseous disc with $r \sim 7$ kpc.

The ICM wind keeps eroding the gaseous discs of the three models until the end of the simulation ($t = 500$ Myr), leaving a remnant disc with $r \sim 12$ kpc and $r = 10$–12 kpc for the MHD and heavy models, respectively. The HD simulation was run longer, but the disc length reaches an approximate steady truncation radius of $\sim$4 kpc at $t = 500$ Myr, showing that the erosion of this model was faster and more efficient than in the MHD and heavy discs, that loose their gas at a slower rate, as mentioned in Section 3.1, and whose discs are truncated at a larger radius.

It is worth mentioning that the increase in Σ is related with the following numerical factors. First is the difficulty of modelling a cylindrical system in a Cartesian grid. The gas fluxes across grid boundaries in this mismatch lead to errors when the curvature of the circular orbits is large, generating spurious radial flux and a lack of proper rotational support. Second is the rapidly changing gravitational potential in the central regions of the galaxy. The HD disc has a scale height of $\sim$200 pc or even smaller at $r = 0$, and

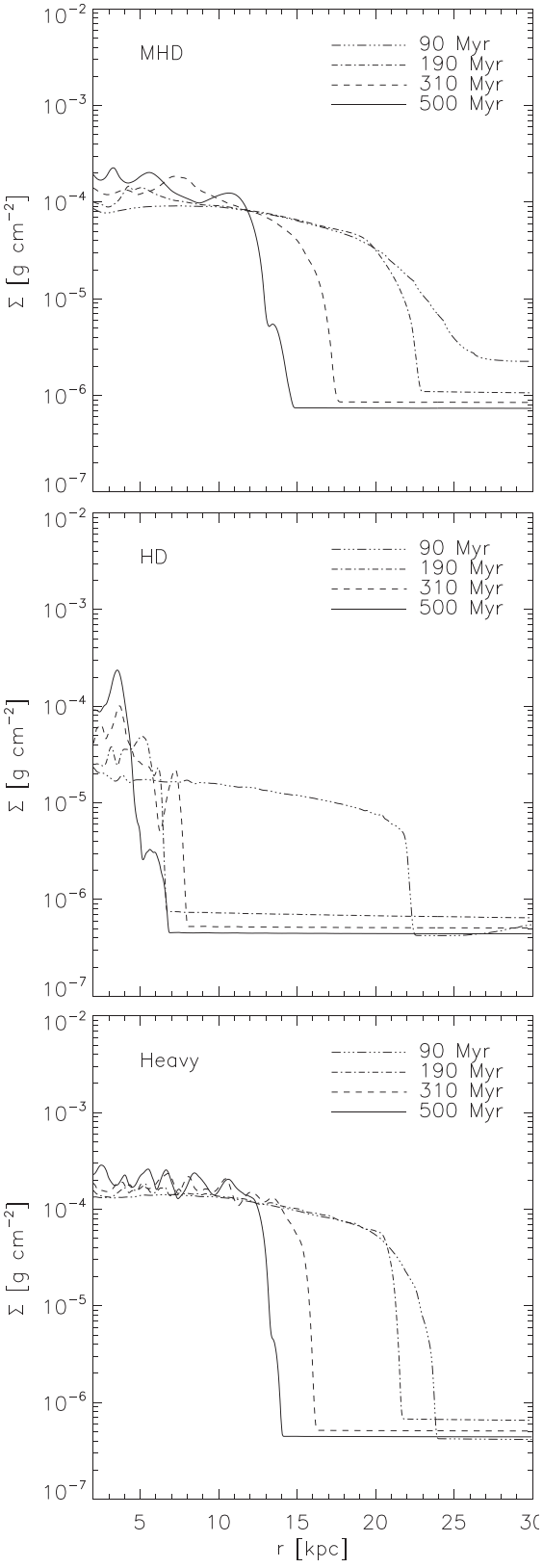

Figure 5. Evolution of surface density for the MHD (*top*), the HD (*middle*), and the heavy (bottom) models as a function of galactocentric radius. The surface density is calculated up to $z = \pm 5$ kpc from the mid-plane for the MHD disc and $z = \pm 3$ kpc for the HD and heavy discs. The MHD and heavy discs (*top* and *bottom*) are eroded more slowly than the HD (*middle*).

Downloaded from https://academic.oup.com/mnras/article-abstract/476/3/3781/4867983 by Universidad Nacional Autonoma de Mexico user on 14 September 2018

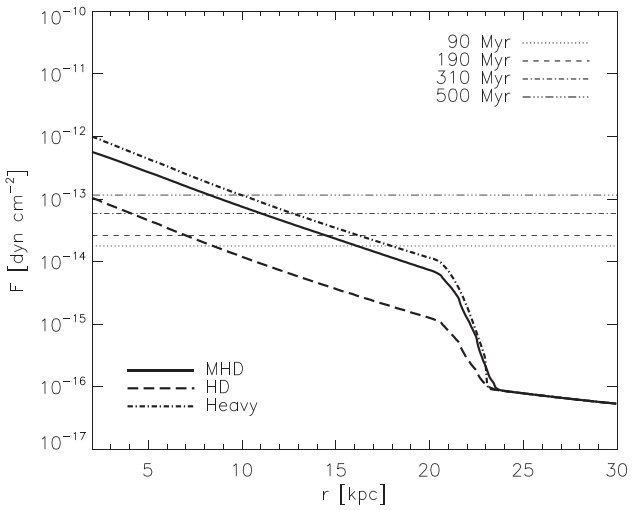

Figure 6. The Gunn–Gott criterion (Gunn & Gott 1972) for disc gas stripping applied to the simulation discs. The thick lines represent the restoring force of the MHD (solid line), the HD (dashed line), and the heavy (dot–dashed line) disc, while the horizontal lines correspond to the ram pressure measured at different times. For a given set of wind parameters, the radius where the $P_{\rm ram}$ intersects the restoring force defines the truncation of the gas disc.

with the best spatial resolution achieved, just a few grid points are calculating the hydrostatic. We tested how much our models deviate from equilibrium by performing simulations of isolated MHD and HD disc and found that the ill-resolved hydrostatics and rotation generate a collapse of material in the centre of the galaxy, which yields to an increase in the surface density. In the HD isolated disc, the surface density increases from 1 to 2 orders of magnitude in $r < 2$ kpc from $t = 0$ to $t = 500$ Myr. There is also an infall of material in the isolated MHD model, but since this disc is more extended in the z-direction, the increase in the surface density is less than one order of magnitude for the same radii and time of evolution compared with the HD case, this is because the grid effects are smaller in the MHD model. When the wind is on, the increase of the surface density is lower than in the isolated cases, since the interaction with the wind diminish this effect. With this in mind, the surface density is not an adequate measure of the inflow of gas derived from the oblique shocks in our models (see Section 3.3).

3.2.2 Disc truncation

Fig. 6 shows the gravitational force per unit area for the MHD (solid thick line), HD (dashed thick line), and heavy (dot–dashed thick line) discs, approximated as follows: using the gravitational potential of the background axisymmetric model we obtained the maximum force in the z-direction as function of r and multiplied by the surface density $\Sigma(r)$:

$$F(r) = F_{z\rm max}(r)\,\Sigma(r) = -\frac{\partial\Phi(r, z_{\rm max})}{\partial z}\,\Sigma(r)\,, \qquad (12)$$

where $z_{\rm max}$ is the point where the gravitational force is maximal. Notice that the gravitational potential is the same for all models but the differences in the restoring force are due to the initial surface density in the discs (see Section 2.1).

This gravitational restoring force is compared with the ram pressure $P_{\rm ram} = \rho_{\rm ICM} v_{\rm ICM}^2$ exerted by the wind (represented with the horizontal lines in the figure). The gravitational force of the disc decreases with increasing radius so, for a given set of parameters for the wind, we expect that the discs are truncated at the radius where both forces are equal, that is, where the $P_{\rm ram}$ and the force lines cross each other. For the wind parameters, we have $n = 10^{-5}$ cm^{-3} and the velocity is taken from the simulation. Since it increases in time we chose the value of $v_{\rm ICM}$ at $z = 0$, when it has reached the disc mid-plane. The lines for the ram pressure are labelled according to the time at which the wind velocity was calculated.

Following the GG criterion, the truncation radii expected for the MHD, HD, and heavy discs are $r \sim 16$, ∼8.5, and ∼18 kpc, respectively, with the wind velocity measured at $t = 90$ Myr, which is smaller compared to the cut in the radial direction of our discs measured in the simulation ($r_{\rm MHD} \sim 23$ kpc and $r_{\rm HD,\,heavy} \sim 21$–22 kpc). At $t = 190$ Myr, the GG truncation radii are also smaller for the MHD and heavy discs compared to the ones calculated from the simulation: 14.5 kpc (19 kpc in the simulation) for the MHD and 16.5 kpc (20 kpc in the simulation) for the heavy model. For the HD disc, the truncation radius measured from the simulation is in better agreement with the one predicted by GG, $r \sim 6$–7 kpc, and could be due to the fact that this model loses its gas faster than those with a higher initial Σ.

At later times, from $t = 310$ to 500 Myr, the truncation radius from GG is more similar to that observed in the simulations, showing slight differences of 1–2 kpc in the two non-magnetized models. By the end of the simulation, $t = 500$ Myr, the radius of the MHD disc should be $r \sim 8$–9 kpc according to GG, while the size measured is $r \sim 12$ kpc. For the HD model, GG predicts $r \sim 2$ kpc while we measure $r \sim 4$ kpc in the simulation. Finally, in the heavy disc we have $r \sim 10$ kpc and $r \sim 10$–12 kpc with GG criterion and measured in the simulation, respectively. The three models are a reasonable fit to the GG criterion, although the HD and heavy ones are marginally better. This could be due to the assumptions of GG: a zero-width disc (the HD model disc has a scale height of ∼200 pc) and no consideration of the effect of the MF in the gas dynamics. Still, even if the values for the truncation radius do not coincide exactly with the calculations from the simulations, the GG criterion yields a good approximation of how much a gaseous disc may be stripped due to ram pressure.

3.3 Oblique shocks

The MHD model has a flared disc (see Section 2.1) since the MF yields a less-compressive gas layer. Therefore, when the ICM wind reaches the galaxy, an oblique shock is generated in the wind-disc interface. The shocks change the initial distribution of gas in the disc, as can be seen in the density contours in Fig. 7 (upper panel), and are present in most of the wind-facing side of the disc. The figure compares the initial distribution of the gas density of the disc (dotted line) and at $t = 90$ Myr (solid line). The most diffuse gas with $n = 10^{-4}$ cm^{-3} (see the -4 contour) is pushed up and compressed so that the density is more extended in the $+z$-direction than in the $-z$-direction. Conversely, gas with 10^{-3} cm^{-3} (-3 contour) is more extended in the $-z$-direction compared to the initial distribution because of the accumulation of the material due to the compression. This compression advances to smaller radii, so that there is more dense gas in the central regions of the galaxy, leading to an expansion of the inner part of the disc with $n = 10^{-2}$ cm^{-3} (-2 contour) in the radial direction and below the mid-plane in 5 kpc $< r <$ 7 kpc.

These oblique shocks lead to a radial inflow of gas towards the inner regions of the galaxy. The middle panel of Fig. 7 shows this (azimuthally averaged) mass flux at $t = 90$ Myr, with the gas

Downloaded from https://academic.oup.com/mnras/article-abstract/476/3/3781/4867983 by Universidad Nacional Autonoma de Mexico user on 14 September 2018

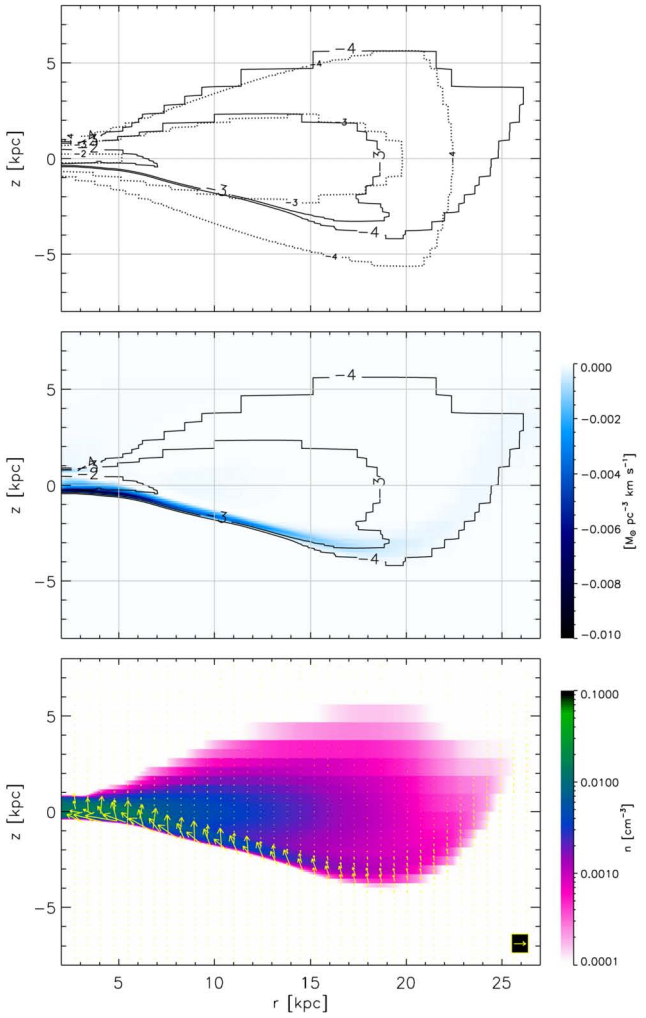

Figure 7. (Top)Slice of density for the MHD disc in a $y = 0$ cut at time $t = 0$ Myr (dotted line) and $t = 90$ Myr (solid line). The contour levels are $n = 10^{-4}$, 10^{-3}, and 10^{-2} cm^{-3} and are labelled from outside-in. *(Middle)* Radially inward flux of mass due to the oblique shocks at the ICM–ISM interaction zone for the same time-step. Colours in the flux map show radially inward mass flux, while the contours are the same as the ones for $t = 90$ Myr in the top panel, for comparison. *(Bottom)* Slice of density for $t = 90$ Myr in a $y = 0$ cut, where the colours show the gas number density and flux arrows are overlaid. The scale in the bottom right box corresponds to a mass flux of 3×10^{-3}M$_\odot$ pc^{-3} km s^{-1}. The oblique shocks are produced (due to the 'bow tie' shape of the disc) at the disc-wind interface and move the gas from the outer galaxy towards the galactic centre.

density contours at $t = 90$ Myr from the upper panel are overlaid. Notice that the inward flux matches with the shocked gas, that is the shocks funnel the gas from larger to smaller radii.

The oblique shocks and the inward flux of mass they produce are present at all radii, being stronger in the inner region of the disc (2 kpc $< r <$ 10 kpc) than in the external region. The inflow of gas can be also observed through flux arrows, which are represented in the bottom panel of Fig. 7, where these are overlaid on a density slice as in Fig. 2, in the $y = 0$ plane also for $t = 90$ Myr. The flux arrows show the motion of gas to the centre of the galaxy produced by the oblique shocks, as we mentioned earlier. The shocked gas at the interface of the disc and the wind ($z < 0$) is pushed up and redirected to smaller radii. These shocks and the inflow of gas from the outskirts ($r > 10$ kpc) may supply the central regions of the disc

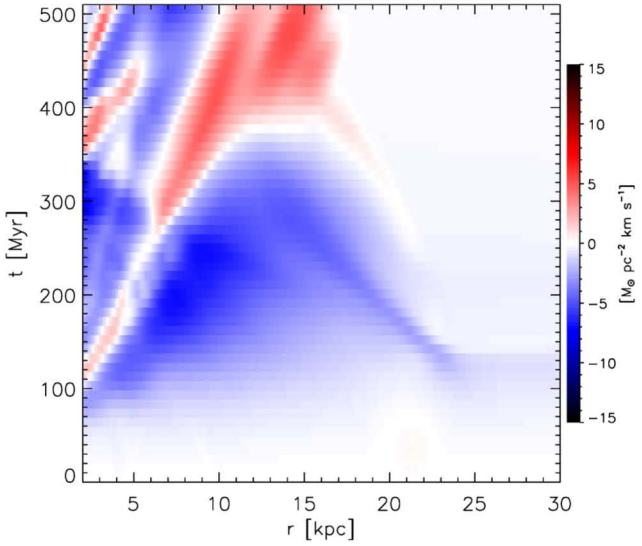

Figure 8. Flux of disc mass integrated in z as a function of time. The radial flow azimuthally averaged is z-integrated within the range $|z| \leq 10$ kpc. The colour-bar shows the inward motions in blue and the outwards as red of the mass flux. The oblique shocks appear in $r = 5$–10 kpc at $t \gtrsim 100$ Myr and increase outwards, driving gas to smaller radii. The shocks reach their maximum strength at $t \approx 250$ Myr and after that they start to vanish from the outskirts of the disc ($r > 10$ kpc) when the ram pressure increases and generates an outward flow of gas instead at $t > 300$ Myr.

to ignite star formation or nuclear activity, until the ram pressure increases and starts to sweep the gas from the galaxy.

Fig. 8 shows the evolution in time of the z-integrated radial gas flux. The gas flux is integrated over a height of $|z| \leq 10$ kpc. Blue colour represents the radial inflow and red colour is the outflow. As it was previously mentioned, the gas is compressed and funnelled to the inner regions of the galaxy. Both the shocks and the flow appear at $t = 90$–100 Myr and have a radial extension of $r = 6$–8 kpc, where the flux is maximum at this time. As the wind pushes a larger portion of the disc, the shocks and the inflow they produce increase in radius as time increases. For example, in 15 kpc $< r <$ 20 kpc the inflow is active from $t \sim 150$ Myr to $t \sim 300$–350 Myr, which means that the oblique shocks can funnel the gas from the outskirts of the disc to smaller radii before the wind sweeps it out.

The strongest inflow is generated in the time interval of ∼100–250 Myr after the shocks appear, that is, in the $t \sim 200$–350 Myr mark in Fig. 8. After $t = 300$ Myr, the inflow from the outskirts, that is the gas originally located in $r > 10$ kpc, becomes weaker until it starts to vanish at $t \sim 400$ Myr. This happens when the wind accelerates and surpasses the galactic gravitational potential, generating an outward flow instead and finally removing the gas of the disc. The swept gas is represented by the red area near the end of the simulation, $t > 400$ Myr and in the radial range of $r = 10$–17 kpc. Even though at times $t >$ ∼350 Myr for radii $r < 10$ kpc, there is still an inflow of gas to the centre of the disc, the motion in this region is more random or disordered due to the interaction with the high-speed wind ($v_{\rm ICM} > 700$ km s^{-1}), which is observed in the blue and red bands. Additionally, the initial flaring of the disc has almost vanished since the wind has compressed and displaced the gas below the mid-plane.

It can be seen from Fig. 2 that the heavy disc is also flared but to a lesser extent than the MHD one. We also analyse the oblique shocks in the heavy disc model. We observed an increase in the

Downloaded from https://academic.oup.com/mnras/article-abstract/476/3/3781/4867983 by Universidad Nacional Autonoma de Mexico user on 14 September 2018

density of the disc due to a compression of the gas in the wind-disc interaction zone, as in the MHD model. Nevertheless, the layer of the shocked gas is less prominent, with a thickness of ∼200 pc, which is ≤0.4 of the shocked region in the MHD case, where the thickness of the compressed gas ranges from ∼500 pcto 1 kpc in some regions of the disc. The intensity of the azimuthally averaged flux (as a function of r and z) for the heavy disc has nearly the same maximum value reached in the MHD case at the time as shown in Fig. 7 ($t = 90$ Myr), but the strongest flux in the heavy model is located near the centre of the disc, where our set-up is not very reliable due to the grid. Studying the flux arrows for the heavy disc, we also observed that the vertical motion of the gas in the $+z$-direction dominates over the radial one, that is the wind mostly moves the gas upwards before funnelling it to the centre of the galaxy. Additionally, the compressed layer of gas is closer to the galactic mid-plane, so the shock is less oblique. The inflow of gas as a function time for the heavy model is on average a factor of 0.5 lower than in the MHD since in the latter there is gas located at higher z-direction and therefore, when the flux is integrated in the z-direction, there is more gas moving towards the centre of the disc and the total flux as a function of time and r is higher. The strongest inflow in the heavy model is present between $t \sim 150$ and 300 Myr, lasting ∼150 Myr. At $t > 300$ Myr the motion of gas in the heavy model is more disordered in the inner disc ($r < 10$ kpc) until it is finally removed by the wind.

The inflowing gas driven by the oblique shocks raise the possibility of a strong star formation episode in the central part of the galactic disc while the outskirts of the galaxy are being stripped of gas. Observations suggest that S0 galaxies had their last star formation burst in their bulge (Sil'chenko 2006; Prochaska Chamberlain et al. 2011; Bedregal 2012; Johnston et al. 2012, 2014; Sil'chenko et al. 2012, but see Katkov et al. 2015), so this mechanism can provide the central regions with the gas necessary for that burst. Additionally, galaxies undergoing RPS have shown unusual nuclear activity, possibly because the gas is being pushed to the centre and also an enhanced star formation in the region where the gas is compressed by the ICM, that is, the star formation is induced and enhanced by the ram pressure (Cayatte et al. 1990; Poggianti et al. 2016). Poggianti et al. (2017) found a very high incidence of active galactic nucleus (AGN; Seyfert 2) among jellyfish galaxies from MUSE data and they conclude that ram pressure triggers the AGN activity.

There are several points that need to be kept in mind when comparing our simulations with the above quoted results. First, in this work we present only a generic model for a flared disc galaxy. More studies must be performed in order to verify the presence of these oblique shocks in galaxies. In our model, the flare is created by an MF, but this is not the only mechanism to create such a disc (for example, a different equation of state for the gas as presented by Roediger & Hensler 2005). The second point to consider is that the central regions of the disc in our simulation are too idealized, and so it is hard to state how much of the inward flux created by the shock actually reaches the centre of the galaxy. Also, the perfectly face-on geometry of the interaction might have an influence of the shocked-gas galactic inflow. More numerical experiments, with less idealized conditions, will be presented in future contributions. Nevertheless, as long as the disc flares, oblique shocks should appear for a face-on ICM wind interaction and the presence of an MF is a good mechanism to generate such a flare. Also, since a magnetized disc is less compressible than a pure HD one, the shocked layer in the MHD model will be more pressurized and will try to drain gas, either to the outskirts and/or to the central regions of the disc.

4 CONCLUSIONS

We performed MHD and HD simulations of a disc galaxy subject to RPS to analyse the impact of the MF in the dynamics of the gas during the stripping event. Both models were set up in hydrostatic equilibrium with the gravitational potential of an M33-like galaxy, without the galactic bulge component of the potential.

We found that the galactic MF gives us a thicker gaseous disc than the HD one, which changes the dynamics of the model, that is, we have gas farther from the galactic potential well (in the z-direction) in the MHD, plus the surface density in z is higher than in an HD disc with the same mid-plane density. When the ICM wind hits the discs, at the beginning of the simulation, the MHD disc is hardly affected by the wind, since no significant changes were observed in the initial shape of the disc, and only the compressed gas in the interaction interface was observed. The HD disc is easily perturbed and pushed off the galactic mid-plane by the wind. Then the gravitational potential pulls back the material to disc, generating an infall of gas to the disc until the ram pressure exceeds the gravitational force and removes the gaseous disc.

The evolution of both models continues as the wind velocity increases. Their ISM is removed of the disc, from the outside-in, and reaches higher z above the mid-plane. When the models have evolved for $t = 500$ Myr, the swept gas in the MHD case is denser, reaches a height of approximately $z \sim 20$ kpc, and the disc has been truncated to $r \sim 10$ kpc. In the HD run, the swept gas is farther away from the galactic mid-plane, $z \sim 40$ kpc, and has a lower density than the MHD. The disc is also eroded to a smaller radius of $r \sim 4$–5 kpc. These results show that the removal of the gas disc is less efficient in the MHD model than in the HD case with the same mid-plane density.

The main differences found so far between the models are as follows:

(i) The HD disc is more easily eroded than the MHD one, because in the magnetized case we have a higher surface density Σ and the gas is less compressible than in the HD model. Since the surface density strongly affects the stripping rate, we developed an HD model with approximately the same Σ as the MHD, which shows a similar stripping rate. This 'heavy' HD disc has a very high mid-plane volumetric density that makes it unrealistic.

(ii) The swept gas for the MHD model has a smooth appearance whilst for the HD models (both the regular and the heavy discs), the gas above the galaxy has a clumpier and filamentary-like morphology, that is, the MF mainly affects the shape and structure of the swept gas.

Previous RPS simulations have obtained broader tails, that is the swept gas of the discs, compared with observations of jellyfish galaxies (galaxies undergoing RPS). It was expected that additional physical properties, such as MF, cooling, star formation, etc. may help to solve this problem, presenting narrower tails in the simulations. Ruszkowski et al. (2014) presented MHD simulations with radiative cooling and self-gravity for a magnetized ICM only, and showed that the MF can give narrower gas tails compared with HD models. Our runs show the opposite behaviour, the swept gas from the disc in the MHD model is broader than the HD, but we do not have the same initial set-up as them. The differences in the tail width could be also accounted for the radiative cooling. HD simulations performed by Tonnesen & Bryan (2010) including radiative cooling showed narrower tails in better agreement with observations, compared to non-cooling models. On the other hand, the swept gas from our MHD model shows a smooth structure, while the HD

Downloaded from https://academic.oup.com/mnras/article-abstract/476/3/3781/4867983 by Universidad Nacional Autonoma de Mexico user on 14 September 2018

models look clumpier, similarly to tails observed in Ruszkowski et al. (2014). The differences observed in the shape and morphology of the swept gas in our models lie in the equation of state of the gas, that is an isothermal gas is more compressible than an adiabatic (e.g. Roediger & Hensler 2005; Roediger & Brüggen 2007, 2008; Tonnesen & Bryan 2009, 2010) or a magnetized gas, and when the wind hits the galaxy, clump-like regions appear in our HD simulations. When these regions are pushed and eroded by the wind, they generate tails in the swept gas, where the flow is similar to the cigarette smoke, giving the filamentary and clumpy shape to the swept gas in our HD simulation. A more detailed analysis of the morphology and structure of the gas tails will be presented in the near future (Ramos-Martínez et al., in preparation). Tonnesen & Stone (2014) also performed RPS models with galactic MF, with different configurations and intensities for the field, and they found that the MFs do not make a significant difference in the stripping rate of ISM, but the MF inhibits the mixing of the gas tail with the surrounding ICM and unmixed gas survives at larger distances from the disc. In our results we see a similar trend, since the swept gas in the MHD model also remains unmixed for longer time, despite the fact that the z-height is smaller as compared to our HD run. The differences in the tail appearance and structure for their MHD and HD models are not so evident or dramatic. Since the approach of our models is not the same as Ruszkowski et al. (2014) and Tonnesen & Stone (2014), we cannot make an analytical comparison with their works. We consider that, in order to understand if MF can make a significant difference and its relevance in the interaction of the ICM–ISM, further investigation will be needed.

Even when our HD simulation ran for 1 Gyr, the model reached equilibrium at $t \lesssim 500$ Myr: the truncated disc remained with the same radius although the wind was still accelerating to a maximum velocity of 1000 km s^{-1} before the simulation ended. Therefore, we can assume that the MHD run has also reached equilibrium with the ram pressure, or is near to it. The remaining gaseous disc could be removed by other mechanism, like interactions or fly-by's with other galaxies (e.g. galaxy harassment), this should be taken into account because these objects are not completely isolated, specially in clusters. Interactions between galaxies can remove the gas or trigger star formation so the ISM is consumed or exhausted.

It is well known that RPS works well removing the gas of the galaxies, but this process fails in reproducing other S0s features, like higher bulge-to-disc ratios than spirals, given that RPS has been proposed as a transformation mechanism of spirals to S0s. For our magnetized case, with inefficient RPS, we found an interesting behaviour in the gas: there are motions of gas from large radii to the galactic centre. This phenomenon occurs only in the early stages of the simulation, when the wind hits the disc, and it is produced by oblique shocks at the interface of the interaction. The oblique shocks appear because of our flared gas disc due to the MF presence and lead the gas to the centre of the disc, which may help to maintain a reservoir of gas available for star formation in the central region of the galaxy, which in consequence could produce a thicker bulge that may lead to a higher bulge-to-disc ratio. Studies have shown that the last star formation burst in S0s galaxies took place in the bulge (Sil'chenko 2006; Prochaska Chamberlain et al. 2011; Bedregal 2012; Johnston et al. 2012, 2014; Sil'chenko et al. 2012, but see Katkov et al. 2015). Besides, if new stars are born from the remaining gas in the centre, their strong winds could expel the rest of the ISM from the galaxy.

Other observations of galaxies affected by RPS have shown unusual nuclear activity, that is, the gas may be pushed to the centre and the compression produced by the ICM enhances star formation: the star formation is induced and enhanced by the ram pressure (Cayatte et al. 1990). Poggianti et al. (2016) showed an atlas of stripping candidates where most of their galaxies presented higher star formation compared to non-stripped galaxies. From this results, the oblique shocks can be seen as a mechanism that enhances the formation of new stars in the remaining disc or even trigger nuclear activity (e.g. an AGN). Also Poggianti et al. (2017) found a very high incidence of an AGN (Seyfert 2) among jellyfish galaxies from MUSE data and the conclusion is that ram pressure triggers the AGN activity. Since the flux of gas derived from the oblique shocks in our MHD simulation lasted about ∼150 Myr from the time the wind hit the disc, this could be considered as comparable with the duty cycle of AGNs, which has been estimated in 10–100 Myr (Haehnelt & Rees 1993), but given that our simulation neither properly model the central regions of the galaxy, nor we have a central black hole, we can only speculate that the oblique shocks will transport the gas for enough time to ignite an AGN. Other tests need to be performed to better study the funnelling of gas towards the central regions of the galaxy, such as different wind profiles and angles, and different disc surface densities and flare strengths.

Additionally, it has been reported that the star formation can continue in the tail of the stripped gas, as it is shown in observations of H II regions in the tail of a galaxy subject to RPS (Kenney & Koopmann 1999; Boselli & Gavazzi 2006; Cortese et al. 2007; Yoshida et al. 2008; Hester et al. 2010; Sun et al. 2010; Yagi et al. 2010; Abramson et al. 2011; Kenney et al. 2014; Poggianti et al. 2016). Due to the limitations of our models, neither enough resolution nor the appropriate equation of state to solve the star formation, we cannot explore the possibility of new stars born in the swept gas of our models or the centre of the discs from the motions of gas originated from the oblique shocks. More on this subject, as well as an in-depth analysis of the swept gas for the MHD model, will be done in a future work (Ramos-Martínez et al., in preparation).

ACKNOWLEDGEMENTS

We thank B. Poggianti, M. Owers, and P. Appleton for useful comments and discussions. We also thank an anonymous referee for comments that helped improve this manuscript. We acknowledge financial support from UNAM-DGAPA PAPIIT grant IN100916, and CONACyT for support for MRM.

REFERENCES

Abadi M. G., Moore B., Bower R. G., 1999, MNRAS, 308, 947
Abramson A., Kenney J. D. P., 2014, AJ, 147, 63
Abramson A., Kenney J. D. P., Crowl H. H., Chung A., van Gorkom J. H., Vollmer B., Schiminovich D., 2011, AJ, 141, 164
Abramson A., Kenney J., Crowl H., Tal T., 2016, AJ, 152, 32
Adebahr B., Krause M., Klein U., Weżgowiec M., Bomans D. J., Dettmar R. J., 2013, A&A, 555A, 23
Aguerri J., Balcells M., Peletier R., 2001, A&A, 428
Aguerri J., Agulli I., Diaferio A., Dalla Vecchia C., 2017, MNRAS, 468, 364
Allen C., Santillán A., 1991, Rev. Mex. Astron. Astrofis., 22, 255
Beck R., 2005, in Chyży K. T., Otmianowska-Mazur K., Soida M., Dettmar R.-J., eds, Proc. Conf. Held in Krakow, Poland, The Magnetized Plasma in Galaxy Evolution, Jagiellonian University, Krakow, Poland, p. 193
Beck R., Fletcher A., Shukurov A., Snodin A., Sokoloff D. D., Ehle M., Moss D., Shoutenkov V., 2005, A&A, 444, 739
Beck R., Wielebinski R., 2013, in Gilmore G., ed, Planets, Stars and Stellar Systems, Vol. 5. Springer-Verlag, Berlin, p. 641
Bedregal A. G., 2012, A&AT, 27, 177

Downloaded from https://academic.oup.com/mnras/article-abstract/476/3/3781/4867983 by Universidad Nacional Autonoma de Mexico user on 14 September 2018

Bekki K., 2014, MNRAS, 438, 444
Bekki K., Couch W. J., 2003, ApJ, 596, L13
Bekki K., Couch W. J., Shioya Y., 2002, ApJ, 577, 651
Biviano A., Katgert P., 2004, A&A, 424, 779
Borlaff A. et al., 2014, A&A, 570, 103
Boselli A., Gavazzi G., 2006, PASP, 118, 517
Boselli A., Cortese L., Boquien M., Boissier S., Catinella B., Gavazzi G., Lagos C., Saintonge A., 2014, A&A, 564, A67
Butcher H., Oemler A., Jr, 1978, ApJ, 219, 18
Cayatte V., van Gorkom J. H., Balkowski C., Kotanyi C., 1990, AJ, 100, 604
Chung E. J., Rhee M.-H., Kim H., Yun M. S., Heyer M., Young J. S., 2009, ApJS, 184, 199
Chyży K. T., Beck R., 2004, A&A, 417, 541
Corbelli E., 2003, MNRAS, 342, 199
Cortese L. et al., 2007, MNRAS, 376, 157
Dressler A., 1980, ApJ, 236, 351
Dressler A., 1986, ApJ, 301, 35
Dressler A., Oemler A., Smail I., Barger A., Butcher H., Poggianti B. M., Sharples R. M., 1997, ApJ, 490, 577
Elmegreen D. M., Elmegreen B. G., Frogel J. A., Eskridge P. B., Pogge R. W., Gallagher A., Iams J., 2002, AJ, 124, 777
Farouki R., Shapiro S. L., 1980, ApJ, 241, 928
Fasano G., Poggianti B. M., Couch W. J., Bettoni D, Kjærgaard P., Moles M., 2000, ApJ, 542, 673
Fletcher A., 2010, ASPC, 438, 197
Fletcher A., Beck R., Shukurov A., Berkhuijsen E. M., Horellou C., 2011, MNRAS, 412, 2396
Fossati M., Fumagalli M., Boselli A., Gavazzi G., Sun M., Wilman D. J., 2016, MNRAS, 455, 2028
Frick P, Stepanov R, Beck R, Sokoloff D., Shukurov A., Ehle M., Lundgren A., 2016, A&A, 585, A21
Fuchs B., von Linden S., 1998, MNRAS, 294, 513
Fumagalli M., Fossati M., Hau G. K. T., Gavazzi G., Bower R., Sun M., Boselli A., 2014, MNRAS, 445, 4335
Gallagher J. S., Faber S. M., Balick B., 1975, ApJ, 202, 7
Gießübel R., 2012, PhD thesis, Univ. Cologne
Giraud E., 1986, A&A, 167, 25
Gómez G. C., Cox D., 2002, ApJ, 580, 235
Gunn J. E., Gott J. R. I., 1972, ApJ, 176, 1
Haehnelt M. G., Rees M. J., 1993, MNRAS, 263, 168
Hester J. A. et al., 2010, ApJ, 716, L14
Icke V., 1985, A&A, 144, 115
Jáchym P., Köpen J., Palouš J., Combes F., 2009, A&A, 500, 693
Jáchym P., Combes F., Cortese L., Sun M., Kenney J. D. P., 2014, ApJ, 792, 11
Johnston E. J., Aragon-Salamanca A., Merrifield M. R., Bedregal A. G., 2012, MNRAS, 422, 2590
Johnston E. J., Aragon-Salamanca A., Merrifield M. R., 2014, MNRAS, 441, 333
Kapferer W., Kronberger T., Ferrari C., Riser T., Schindler S., 2008, MNRAS, 389, 1405
Katkov I. Y., Kniazev A. Y., Sil'chenko O. K., 2015, AJ, 150, 24
Kenney J. D. P., van Gorkom J., Vollmer B., 2004, AJ, 127, 3361
Kenney J. D. P., Geha M., Jáchym P., Crowl H. H., Dague W., Chung A., van Gorkom J., Vollmer B., 2014, ApJ, 780, 119
Kenny J. D. P., Koopmann R. A., 1999, AJ, 117, 181
Klein U., Weiland H., Brinks E., 1991, A&A, 246, 323
Koopmann R. A., Kenney J. D. P., 2004, ApJ, 613, 866
Kronberger T., Kapferer W., Ferrari C., Unterguggenberger S., Schindler S., 2008, A&A, 481, 337
Larson R. B., Tinsley B. M., Caldwell C. N., 1980, ApJ, 237, 692
Moore B., Katz N., Lake G., Dressler A., Oemler A., 1996, Nat, 379, 613
Niklas S., 1995, PhD thesis, Univ. Bonn
Oemler A., 1974, ApJ, 194, 10
Otmianowska-Mazur K., Vollmer B., 2003, A&A, 402, 879
Pfrommer C., Dursi J., 2010, Nature Phys., 6, 520
Poggianti B. M. et al., 2016, AJ, 151, 78
Poggianti B. M. et al., 2017, Nat, 548, 304
Postman M., Geller M. J., 1984, ApJ, 281, 95
Prochaska Chamberlain L. C., Courteau S., McDonald M, Rose J. A., 2011, MNRAS, 412, 423
Quilis V., Moore B., Bower R., 2000, Science, 288, 1617
Rengarajan T. N., Karnik A. D., Iyengar K. V. K., 1997, MNRAS, 290, 1
Roediger E., Brüggen M., 2006, MNRAS, 369, 567
Roediger E., Brüggen M., 2007, MNRAS, 380, 1399
Roediger E., Brüggen M., 2008, MNRAS, 388, 465
Roediger E., Hensler G., 2005, A&A, 433, 875
Roediger E., Brüggen M., Hoeft M., 2006, MNRAS, 371, 609
Ruszkowski M., Brüggen M., Lee D., Shin M. S., 2014, ApJ, 784, 75
Schulz S., Struck C., 2001, MNRAS, 328, 185
Scodeggio M., Gavazzi G., 1993, ApJ, 409, 110
Sellwood J. A., Carlberg R. G., 1984, ApJ, 282, 61
Sil'Chenko O., 2006, ApJ, 641, 229
Sil'chenko O., Proshina I. S., Shulga A. P., Koposov S. E., 2012, MNRAS, 427, 790
Simien F., de Vaucouleurs G., 1986, ApJ, 302, 564
Sivanandam S., Rieke M. J., Rieke G. H., 2010, ApJ, 717, 147
Soida M., Otmianowska-Mazur K., Chyży K., Vollmer B., 2006, A&A, 458, 727
Stein Y., Bomans D. J., Ferguson A. M. N., Dettmar R.-J., 2017, A&A, 605, A5
Steinhauser D., Haider M., Kapferer W., Schindler S., 2012, A&A, 544, A54
Sun M., Jones C., Forman W., 2006, ApJ, 637, L81
Sun M., Donahue M., Voit G. M., 2007, ApJ, 671, 190
Sun M., Donahue M., Roediger E., Nulsen P. E. J., Voit G. M., Sarazin C., Forman W., Jones C., 2010, ApJ, 708, 946
Tabatabaei F. S., Krause M., Fletcher A., Beck R., 2008, A&A, 490, 1005
Tapia T. et al., 2014, A&A, 565, 31
Teyssier R., 2002, A&A, 385, 337
Tonnesen S., Bryan G. L., 2009, ApJ, 694, 789
Tonnesen S., Bryan G. L., 2010, ApJ, 709, 1203
Tonnesen S., Bryan G. L., 2012, MNRAS, 422, 1609
Tonnesen S., Stone J., 2014, ApJ, 795, 148
Toomre A., Toomre J., 1972, ApJ, 178, 623
Vollmer B., Marcelin M., Amram P., Balkowski C., Cayatte V., Garrido O., 2000, A&A, 364, 532
Vollmer B., Cayatte V., Balkowski C., Duschl W. J., 2001, ApJ, 561, 708
Vollmer B., Beck R., Kenney J. D. P., van Gorkom J. H., 2004, AJ, 127, 3375
Vollmer B., Soida M., Otmianowska-Mazur K., Kenney J. D., van Gorkom J. H., Beck R., 2006, A&A, 453, 883
Vollmer B., Soida M., Beck R., Urbanik M., Chyzy K. T., Otmianowska-Mazur K., Kenney J. D. P., van Gorkom J. H., 2007, A&A, 464, L37
Vollmer B., Braine J., Pappalardo C., Hily-Blant P., 2008, A&A, 491, 455
Yagi M. et al., 2010, AJ, 140, 1814
Yoshida M. et al., 2008, ApJ, 688, 918-930
Zhang B. et al., 2013, ApJ, 777, 122

This paper has been typeset from a TEX/LATEX file prepared by the author.

Downloaded from https://academic.oup.com/mnras/article-abstract/476/3/3781/4867983 by Universidad Nacional Autonoma de Mexico user on 14 September 2018

Chapter 3

Magnetic field structure in stripped tails and disc inclination effects

This chapter is focused on the imprints observed in the magnetic field (MF) left by the interaction of a disc galaxy with the intracluster medium (ICM) through the ram pressure stripping process when the galaxy falls through the ICM. Different disc inclinations were simulated to study the evolution of the magnetic field and how much the surroundings of the galaxy are magnetized. Additionally, maps of synthetic observations of the polarization and synchrotron emission were obtained for the models. The results presented in this chapter will be part of a second article to be submitted.

3.1 Introduction

Magnetic fields (MFs) have been observed in galaxies from polarized emission in optical (Scarrott et al. 1987; Fendt et al. 1998; Fosalba et al. 2002), infrared (Jones 2000), submillimeter (Greaves et al. 2000), and radio wavelengths (Vollmer et al. 2004, 2010, 2013). In optical wavelengths, the starlight is polarized by elongated dust grains with their major axis aligned with the magnetic field lines perpendicular to the line-of-sight (LOS), while the dust grains emit their own linearly polarized waves at far infrared and submillimeter, without contributions by polarized scattered light (Vallée 1997). Combining information obtained with different techniques like Faraday rotation, Zeeman effect, and polarized radio synchrotron emission, it is possible to develop a model for the 3D structure of MFs in galactic discs. It is known that MFs in spirals have an ordered component, i.e. with a constant and co-

herent direction within the telescope beam (large-scale), and a random or turbulent component that has been amplified and tangled by turbulent gas flows changing its direction within the telescope beam (small-scale) and its orientation can be isotropic or anisotropic (Beck 2005, Beck & Wielebinski 2013 and references therein). The anisotropic turbulent field can be originated from an isotropic field that has been affected by compression or shearing of gas. In spirals, the average total field strength is $\sim 9\mu G$ (Niklas 1995) and the regular field strength is $1-5\mu G$ (Beck & Wielebinski 2013). In radio-faint galaxies like M31 and M33 the total field is $6\mu G$ (Gießübel 2012; Tabatabaei et al. 2008), in gas rich spiral galaxies the total field is $20-30\mu G$ (Fletcher et al. 2011; Frick et al. 2016), for bright galaxies $\sim 17\mu G$ (Fletcher 2010), in blue compact dwarf galaxies $10-20\mu G$ (Klein et al. 1991), and the strongest total fields are found in starburst and barred galaxies with $50-100\mu G$ (Adebahr et al. 2013; Chyży & Beck 2004; Beck et al. 2005).

The MFs in other galaxies have been mainly studied in radio frequencies through synchrotron emission. This radio emission is produced when relativistic particles (electrons or cosmic rays, CR) with density $n_{\rm cr}$ gyrate around the MF lines: $\varepsilon \propto n_{\rm cr} B_{\perp}^{(p+1)/2}$, where $B_{\perp}$ is the MF component perpendicular to the LOS, p is the spectral index of the distribution of cosmic ray electrons, and ε is the emissivity of the synchrotron emission. The linearly polarized synchrotron emission is generated from the regular component of the MF. In observations of spiral galaxies the degree of polarization on average is low in the spiral arms, so the random field is assumed to be stronger there, up to five times the intensity of the ordered field, whilst in the interarm region the degree of polarization is higher, hence the ordered field should dominate. Additionally, it has been observed that the ordered MF shows a spiral pattern that is offset from the spiral arms of gas and stars (Beck 2005). Given that the regular field has large-scale interactions with the environment during events like galaxy harassment, tidal interactions with the cluster or the compression of the gas resulting from ram pressure would have an impact in the polarized synchrotron emission.

Since the MF is frozen into the gas, any interaction in the ISM would be reflected on the MF. For example, during ram pressure stripping, the gas of the galaxy is compressed before it is swept, and hence the MF is compressed too and enhanced (Otmianowska-Mazur & Vollmer 2003). Studies of the synchrotron and polarization emission of spirals have been performed in the Virgo Cluster (Vollmer et al. 2010 and Vollmer et al. 2013). Since it is the rich cluster closest to our Galaxy and it contains undisturbed and interacting galaxies, some of which are good candidates to be under the effect of RPS. In Vollmer et al. (2010), the radio continuum emission has a sharp distribution where the edges coincide with HI distribution, such that the synchrotron traces the interaction of a galaxy with its environment, like RPS and interacting galaxies seen edge-on present a radio continuum emission that extends

a little farther than the HI.

From deep VLA observations at 4.86 GHz, Vollmer et al. (2004, 2007); Chyży et al. (2006, 2007) showed that the distribution of polarized radio continuum emission of 8 Virgo cluster spiral galaxies is strongly asymmetric, with elongated ridges located in the outer galactic disc, which is different for field galaxies where the distribution is generally relatively symmetric and strongest in the interarm regions (Beck 2005b).

Murphy et al. (2009) investigated the radio/FIR relation in galaxies of the Virgo Cluster, possibly affected or with signs of RPS. Galaxies interacting with the ICM show a radio emission deficit on the leading side of the ISM-ICM interaction due to ram pressure. Also, galaxies from the Virgo Cluster exhibit highly polarized radio emission on the upstream side of the ISM-ICM interaction, e.g. NGC 4522 (Chyży et al. 2007; Vollmer et al. 2007). Some Virgo galaxies (NGC 4254, NGC 4388, and NGC 4402) present highly polarized regions that coincide with local radio continuum enhancements and interior to the radio-deficit regions. In the sample of Murphy et al. (2009), it is seen that while the local radio deficit increases, the global radio flux density is enhanced by a factor of $2-3$ compared to isolated galaxies, which could be related to magnetic field compression and CRs that are swept and reaccelerated by the ICM-wind generating synchrotron tails. Also in Vollmer et al. (2013), it was found that even when not too strong active ram pressure stripping has no influence on the spectral index, it enhances the global radio continuum emission with respect to the FIR emission by up to a factor of 2, while an accreting gas envelope may or may not enhance the radio continuum emission with respect to the FIR emission.

MFs are present in the ICM and their strength has been observationally measured and constrained to be $B_{\rm ICM} \sim \mu G$ (reviewed in Carilli & Taylor 2002; Govoni & Feretti 2004; Kronberg 2005; Ryu et al. 2012). Indirect evidence for the presence of cluster MFs and their strengths comes from cluster radio halos produced by the synchrotron radiation (Miley 1980; Giovannini et al. 1993; Feretti et al. 1999; Govoni & Feretti 2004). The integrated cluster MF can be directly measured using the Faraday rotation measure (RM). Faraday RM shows that ICM magnetic fields are of $\sim \mu G$ strengths coherent over scales of tens of kpc (Vallé et al. 1986; Vallée et al. 1987; Kim et al. 1990, 1991; Taylor & Perley 1993; Taylor et al. 1994, 2001; Clarke et al. 2001; Rudnick & Blundell 2003; Murgia et al. 2004; Govoni et al. 2010; Bonafede et al. 2010, 2011, 2013; Vacca et al. 2012) In a phenomenon such as RPS, it is expected that the MFs are dragged with the stripped gas and hence the tails can magnetize or maintain the magnetic fields in the ICM.

On the theoretical side, Ruszkowski et al. (2014) presented simulations of RPS with a magnetized ICM and found that the MF can affect the morphology of the

stripped gas tail, since they observed narrower tails than in purely hydrodynamic (HD) simulations. Pfrommer & Dursi (2010) also showed magnetohydrodynamics (MHD) simulations in which the galaxies are moving in a magnetized ICM. The galaxies in their simulations swept the field lines where polarized radiation is generated. This is used to map the orientation of the MF in clusters. In these cases, the MF has been implemented only in the ICM and not in the discs. Some examples of models with magnetized discs are from Vollmer et al. (2006, 2007) and Soida et al. (2006), which used the method of Otmianowska-Mazur & Vollmer (2003) where a toroidal galactic MF is evolved via the induction equation using a grid code with the velocity field of the particles, so that the MF is advected with the gas. Even if the effect of the MF over the gas dynamics has not been taken into account, this method has been useful to explain the polarized radiation in radio that is observed in some galaxies that may be affected by the RPS, as in the case of NGC 4522 (Vollmer et al. 2006). Additionally, Tonnesen & Stone (2014) performed MHD simulations for the RPS including galactic MF, but the ICM was not magnetized. They found that MFs do not alter or dramatically change the stripping rate of the gas disc compared to pure HD simulations. Nevertheless, the MFs have an impact in the mixing of gas throughout the tail. Since it inhibits the mixing of the gas tail with the ICM, the unmixed gas survives at large distances from the disc. Additionally, the RPS may help magnetize the ICM up to a few μG. Vijayaraghavan & Sarazin (2017) presented MHD simulations where both ICM and ISM are magnetized with different MF orientations and with/without thermal conduction. From their models, the MF orientation changes the morphology of the gas tails: for an MF parallel to the wind motion, the stripped tails are long and narrow compared to case where the MF lines are perpendicular to the ICM motion. Also, the MFs act as a shield in the stripped tails preventing their rapid evaporation in the ICM. Including or not thermal conduction in their simulations represents a difference of $10 - 20\%$ in the gas loss rate, which means that the dominant process in removing the gas from the galaxy is the RPS.

In this chapter it is analysed the structure of the stripped tails when varying the inclination of disc galaxies interacting with the ICM. The evolution of the galactic MF is studied in the scheme of RPS and how much is the ICM magnetized depending on the inclination of a galaxy. Synchrotron emission maps are generated from the models as well as the magnetic field B-vectors.

3.2 Model

In the present study, four models were carried out to represent the RPS of disc galaxies with different inclination angles with respect to motion of the ICM wind:

$0, 20, 70$ and $90^{\rm o}$ with respect to the $z = 0$ plane. The models were performed in 3D with 9 levels of refinement, in a box of size 120 kpc in each direction. Each galaxy is at rest and the ICM flows as a wind to simulate the galaxy falling towards a cluster.

3.2.1 Initial Conditions

To set up the initial conditions of the models, the procedure from Ramos-Martínez et al. (2018) was used for an M33-like galaxy with a rotation curve of $\sim 110-120\,\mathrm{km\ s^{-1}}$ subject to RPS. The galaxy consists of a gas disc that is initially set up in rotational equilibrium with the gravitational force, the magnetic tension, the centrifugal force and the pressure gradient, through the balance equation:

$$\frac{v_\phi^2(r,z)}{r} = \frac{\partial\Phi}{\partial r} + \frac{1}{\rho(r,z)}\left[\frac{\partial P}{\partial r} + \frac{2P_B(r,z)}{r}\right], \tag{3.1}$$

where the total pressure P is the sum of the thermal ($P_{th} = c_s^2\rho(r,z)$, with $c_s \approx 8\,\mathrm{km\ s^{-1}}$ the constant sound speed) and magnetic (P_B) pressures. The magnetic pressure is given by

$$P_{B,inner} = P_{B0}\left[1 - \mathrm{erf}\left(\frac{R}{r_b}\right)\right] \quad \text{for } R < r_b, \text{ and} \tag{3.2}$$

$$P_{B,outer} = \frac{P_{B0}\,n}{(n+n_c)}, \tag{3.3}$$

where $R = \sqrt{r^2+z^2}$, $r_b = b_1/3$, $b_1 = 0.85\,\mathrm{kpc}$ (see table 1 from Ramos-Martínez et al. 2018), $P_{B0} = 1.75\times10^{-13}\,\mathrm{dyn\,cm^{-2}}$, $n = \rho/(\mu m_{\rm H})$[1] and $n_c = 0.04\,\mathrm{cm^{-3}}$. The density and velocity profile are defined first in the galactic midplane and then the distribution at $z \neq 0$ is obtained assuming magnetohydrostatic equilibrium and an isothermal equation of state,

$$\frac{\partial P}{\partial z} = -\rho\frac{\partial\Phi}{\partial z}. \tag{3.4}$$

The rotation velocity at any z is given by (Gómez & Cox 2002):

$$v_\phi^2(r,z) = v_\phi^2(r,0) - v_A^2(r,0) + v_A^2(r,z), \tag{3.5}$$

where v_A is the Álfven velocity ($v_A = \sqrt{2P_B/\rho}$).

[1] $\mu = 1.27$ is the mean particle mass and $m_{\rm H} = 1.67\times10^{-24}\,\mathrm{g}$

Table 3.1: Angle of inclination for the discs and their respective nomenclature. The angle of inclination is measured between the galactic midplane and the $z = 0$ plane.

	Inclination
Mod1	0^{o}
Mod2	20^{o}
Mod3	70^{o}
Mod4	90^{o}

In the central parts of the galaxy ($r < b_1$), the magnetic field (MF) has a random distribution $\mathbf{B_{inner}} = \nabla \times \mathbf{A}$, where $\mathbf{A}$ is the vector potential with random magnitude and orientation. For the rest of the disc, the field has a toroidal configuration where its strength depends on the gas density according to eq. 3.3.

3.2.2 ICM conditions

The ICM is modeled as a wind and the disc is at rest, simulating the falling of the galaxy towards a cluster center. The ICM-wind has a constant density with $n_{\mathrm{ICM}} = 10^{-5}\,\mathrm{cm}^{-3}$ and a velocity profile that increases linearly in time from $300\,\mathrm{km\ s}^{-1}$ at $t = 0$ to $1000\,\mathrm{km\ s}^{-1}$ in 700 Myr and moves in the $+z$-direction. Additionally, we present four models with different galaxy inclinations with respect to the wind direction. Mod1 represents a galaxy with its disc plane parallel to the $z = 0$ plane, i.e. an inclination of 0^{o} or a face-on interaction with the wind. Mod2 and Mod3 are discs inclined 20^{o} and 70^{o}, respectively, and finally in Mod4 the disc has an inclination of 90^{o} with respect to the $z = 0$ plane, which is a completely edge-on interaction with the wind (see table 3.1). The initial conditions of the models are shown in the left panels of figs. 3.1, 3.3, 3.5 and 3.7.

3.3 Evolution of the magnetic field

When the ICM-wind is switched-on and hits the galactic disc, the compression exerted by the wind enhances the MF strength in all the models by a factor of ~ 3 in the shock front. Depending on the geometry of the model, the shocked layer of gas can be present at all radii, as in Mod1 where the compression is visible in $z < 0$ (right panel fig. 3.1), or partially in the disc, as in Mod2 at the region between $z < 0$ and $x < 0$ (right panel fig. 3.3), or more evidently in Mod3 and Mod4 in $z \sim -20\,\mathrm{kpc}$ (see right panels of figs. 3.5 and 3.7).

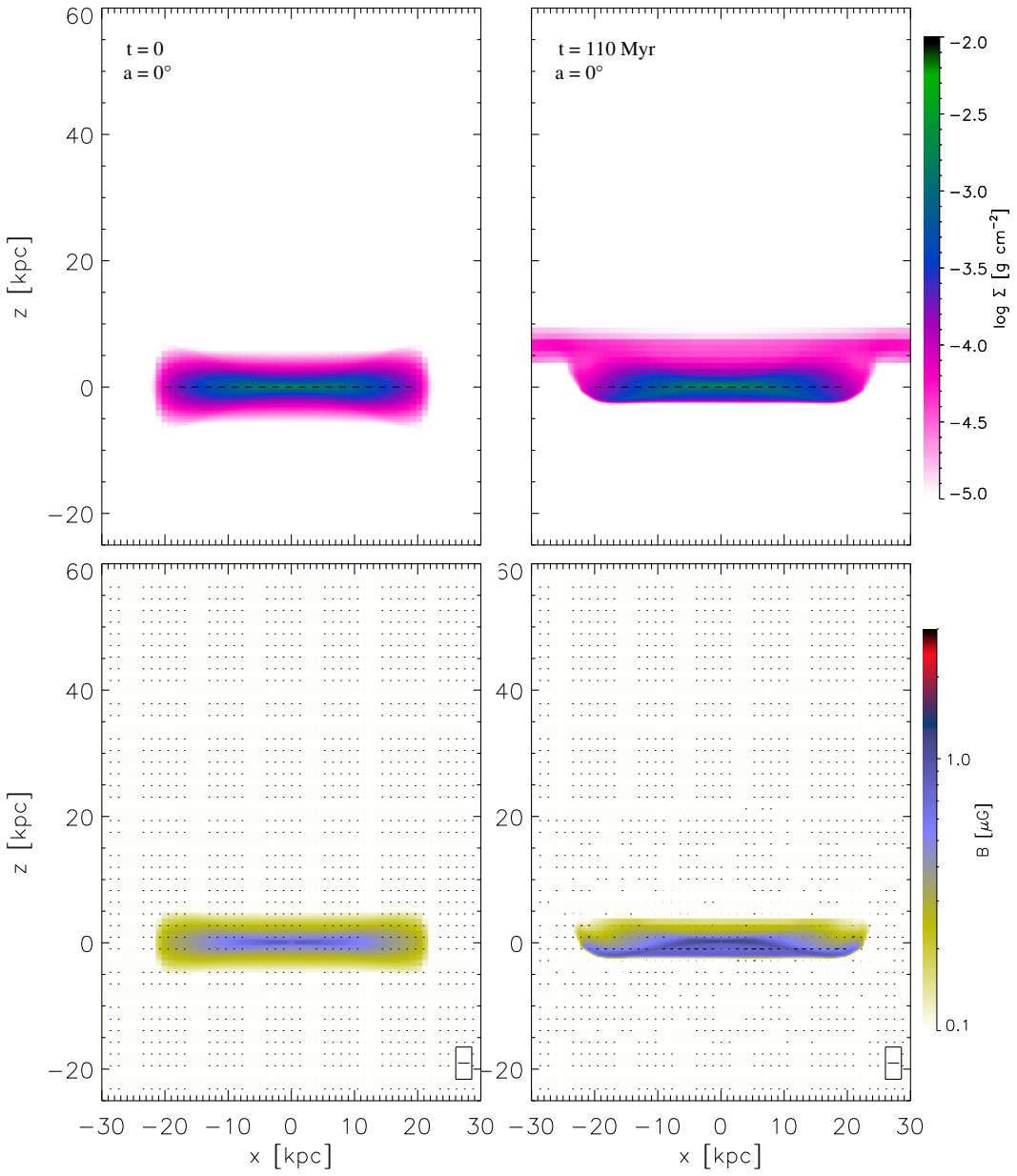

Figure 3.1: Gas surface density (*top row*) and magnetic field strength (*bottom row*) for Mod1 at $t = 0\,\mathrm{Myr}$ (*left column*) and $t = 110\,\mathrm{Myr}$ (*right column*) in the xz-plane. The dashed lines in the top panels represents the initial size of the disc: $r = 20\,\mathrm{kpc}$. The box in the bottom panels shows an MF line with a strength of $0.1\mu G$. In the maps, a denotes the disc inclination with respect to the $z = 0$ plane.

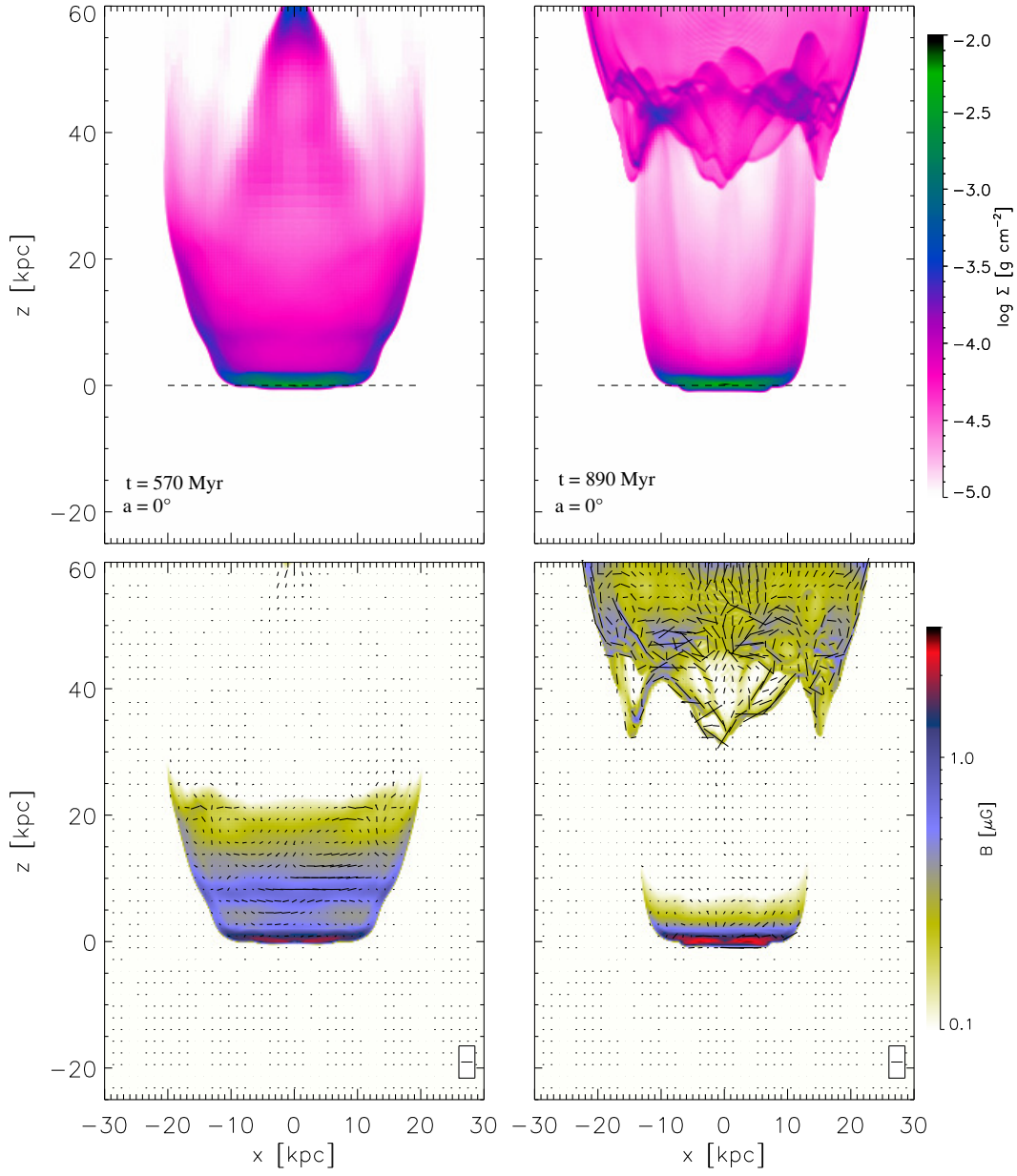

Figure 3.2: Same as fig. 3.1 for $t = 570\,\mathrm{Myr}$ (*left column*) and $t = 890\,\mathrm{Myr}$ (*right column*).

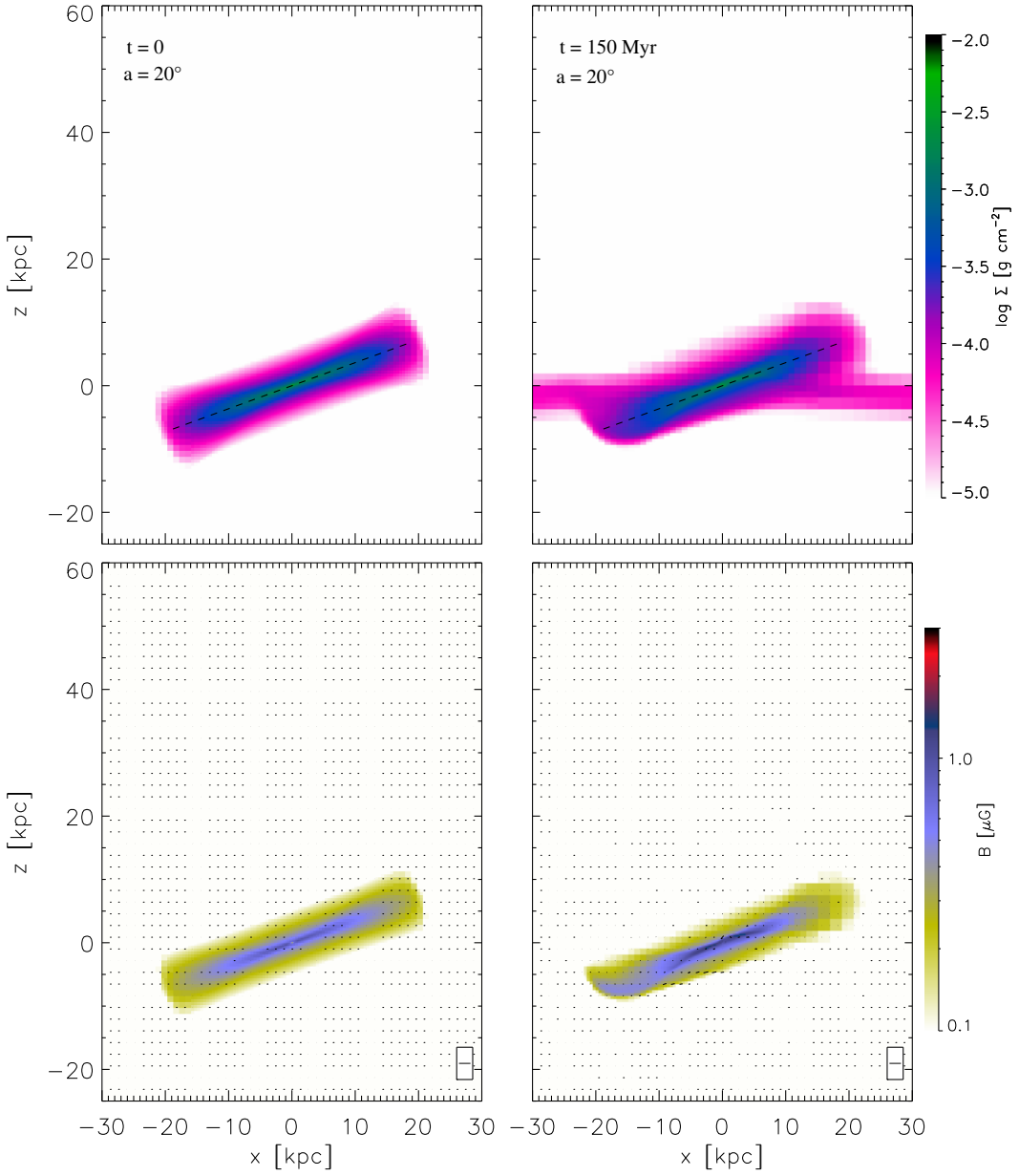

Figure 3.3: Same as fig. 3.1 for the Mod2 simulation at $t = 0\,\mathrm{Myr}$ (*left column*) and $t = 150\,\mathrm{Myr}$ (*right column*). Here the box in the lower panels represents an MF vector of $0.3\mu G$.

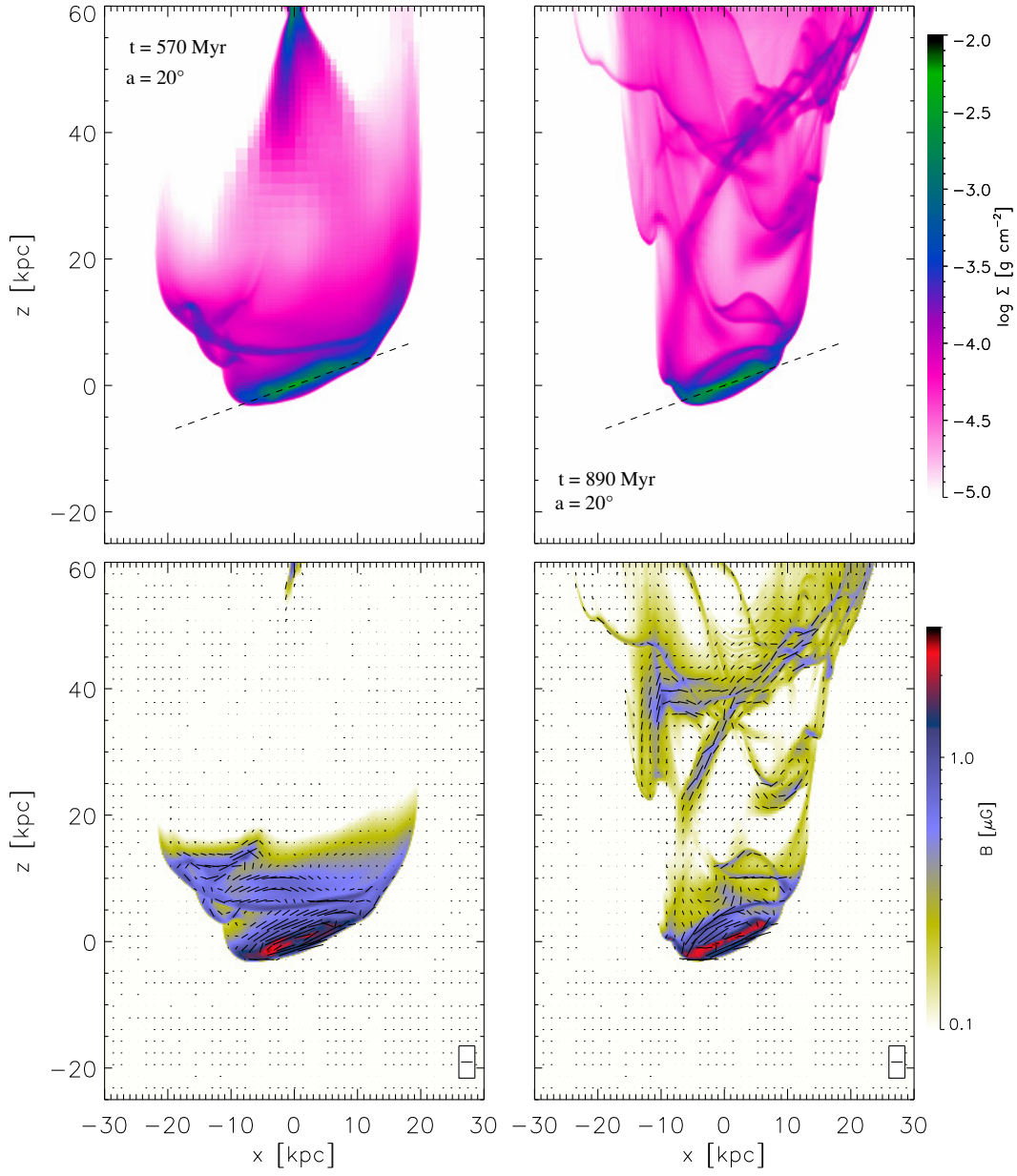

Figure 3.4: Same as fig. 3.3 for $t = 570\,\mathrm{Myr}$ (*left column*) and $t = 890\,\mathrm{Myr}$ (*right column*).

Since the wind keeps flowing and accelerates, it starts to remove the material from the outskirts ($20\,\mathrm{kpc} < r < 10\,\mathrm{kpc}$) where a tail of gas appears in the downstream side. In the Mod1 and Mod2 cases, since the interaction with the wind is (nearly) face-on, the gas is swept from the galaxy in ring-like structures and also the general distribution of the gas has a cap shape as seen in the xz-plane (left panels in figs. 3.2 and 3.4), however, at $z \gtrsim 10\,\mathrm{kpc}$ the rings start to show some slight perturbations along the direction of the wind, farther away from the disc where the stripped gas is less influenced by the potential well of the galaxy. At $t \geq 500\,\mathrm{Myr}$, since the magnetic field is dragged with the gas, it helps to magnetize the downstream side of the tail up to $z \sim 20\,\mathrm{kpc}$ with a strength of $B \approx 0.4 - 0.7\mu G$, which can be seen in the bottom left panels of figs. 3.2 3.4. The disc of the galaxies shows an enhancement of the field from $B(t = 0) \approx 0.8 - 1\mu G$ to $B(t \sim 500\,\mathrm{Myr}) \approx 2.5\mu G$ in $r \lesssim 10\,\mathrm{kpc}$, that is, a factor of $\sim 2-3$. On the other hand, Mod3 and Mod4 do not present a very extended tail at $t \geq 500\,\mathrm{Myr}$, as can be observed in an edge-on view of the galaxies on the xz-plane (left panels in figs. 3.6 and 3.8). Instead, the gas disc shows asymmetries compared to the initial density distribution, being spread out to $z \sim 20 - 40\,\mathrm{kpc}$ but with a low surface densities ($\Sigma < 10^{-4.5}\,\mathrm{g\,cm^{-2}}$). Additionally, in Mod3 and Mod4, the MF intensity increases a factor of $\sim 2 - 3$ ($B \approx 1.5 - 3\mu G$) in the upstream side of the interaction ($-10\,\mathrm{kpc} < z < 0$) while in downstream side ($z = 0 - 20\,\mathrm{kpc}$) the strength of the field remains with no dramatical changes, at $B \approx 0.8 - 1\mu G$ (bottom left panels in figs. 3.6 and 3.8).

At $t = 890\,\mathrm{Myr}$, the wind reaches velocities of $\sim 1000\,\mathrm{km\ s^{-1}}$ in $z = 0$, and for Mod1 and Mod2 it moves the rings of gas above and farther away of the galaxy, showing tails of at least 60 kpc in length (right panels in figs. 3.2 and 3.4). Due to the interaction with the accelerated wind, the rings are distorted in the vertical (z) direction giving a filamentary structure to the tail and, since these filaments are the densest structures of the tail ($\Sigma \sim 10^{-3.6}\,\mathrm{g\,cm^{-2}}$), here the MF has values ranging from $B \approx 0.3 - 0.4\mu G$ to $0.7\mu G$ (figs. 3.2 and 3.4, bottom right panels). At intermediate heights of the tails ($z = 15 - 30\,\mathrm{kpc}$) the field strength drops to $B \lesssim 0.2\mu G$ since less gas is swept from the disc and the surface density also decreases. Mod3 and Mod4 at $t = 890\,\mathrm{Myr}$ did not develop very prominent or extended tails, where the displaced gas of disc lies between $z = 20 - 60\,\mathrm{kpc}$ on figs. 3.6 and 3.8 (right panels). Also the tail is poorly magnetized with $B \lesssim 0.2 - 0.3\mu G$ compared to the (nearly) face-on models (Mod1 and 2).

Observing the disc surface for all the models, that is in the xy-plane for Mod1 and Mod2 (fig. 3.9) and the yz-plane for Mod3 and Mod4 (fig. 3.10), the gas in the remnant disc with $\Sigma > 10^{-3.5}\,\mathrm{g\,cm^{-2}}$ in Mod3 and Mod4 presents more structure than in the tails, i.e. spiral-like features, contrary to Mod1 and Mod2 which show discs with a smoother gas distribution. The structures observed in Mod3 and Mod4 could be related to the fact that in these (nearly) edge-on interactions the ram

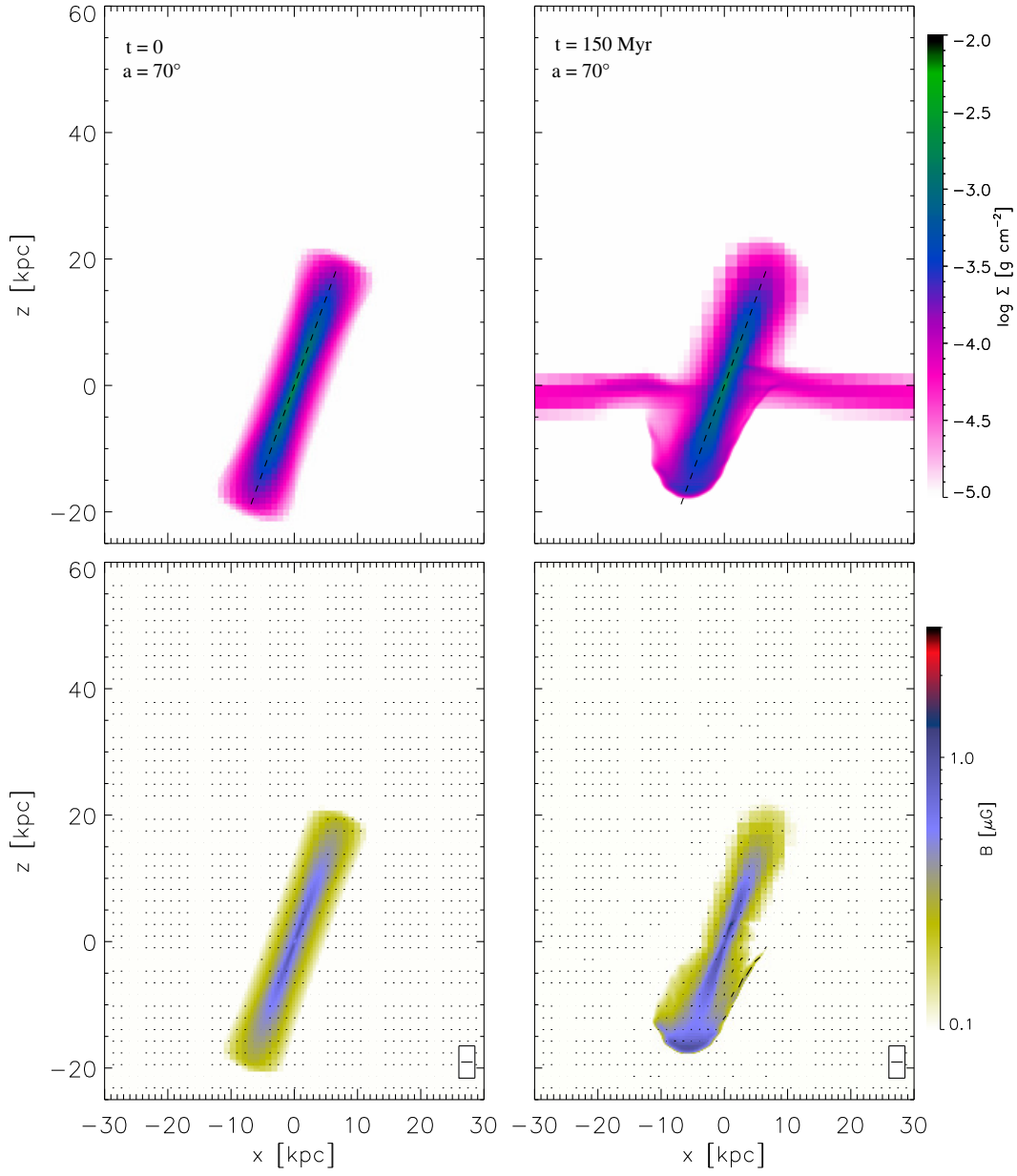

Figure 3.5: Same as fig. 3.3 for the Mod3 simulation at $t = 0\,\mathrm{Myr}$ (*left column*) and $t = 150\,\mathrm{Myr}$ (*right column*).

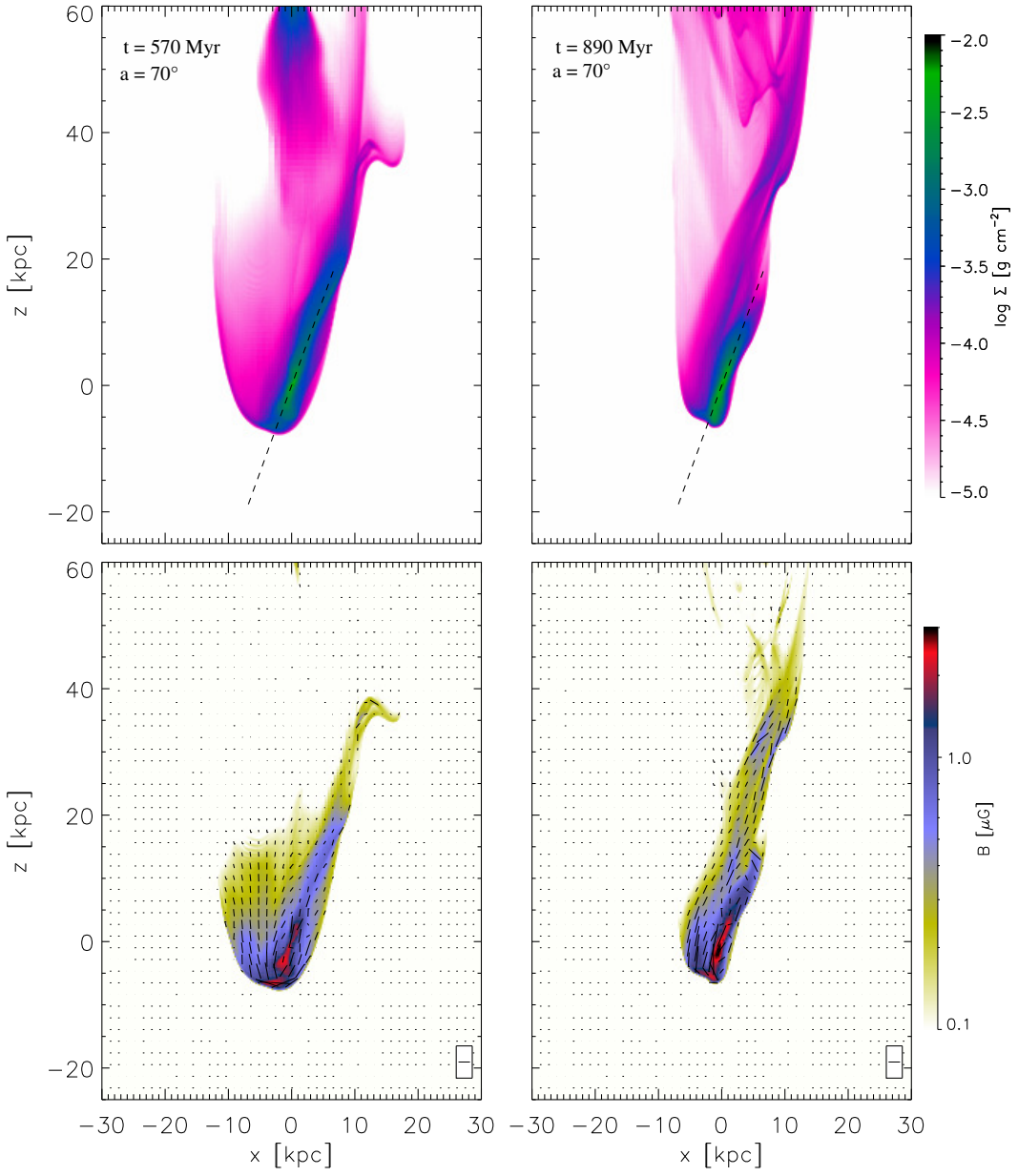

Figure 3.6: Same as fig. 3.5 for $t = 570\,\mathrm{Myr}$ (*left column*) and $t = 890\,\mathrm{Myr}$ (*right column*).

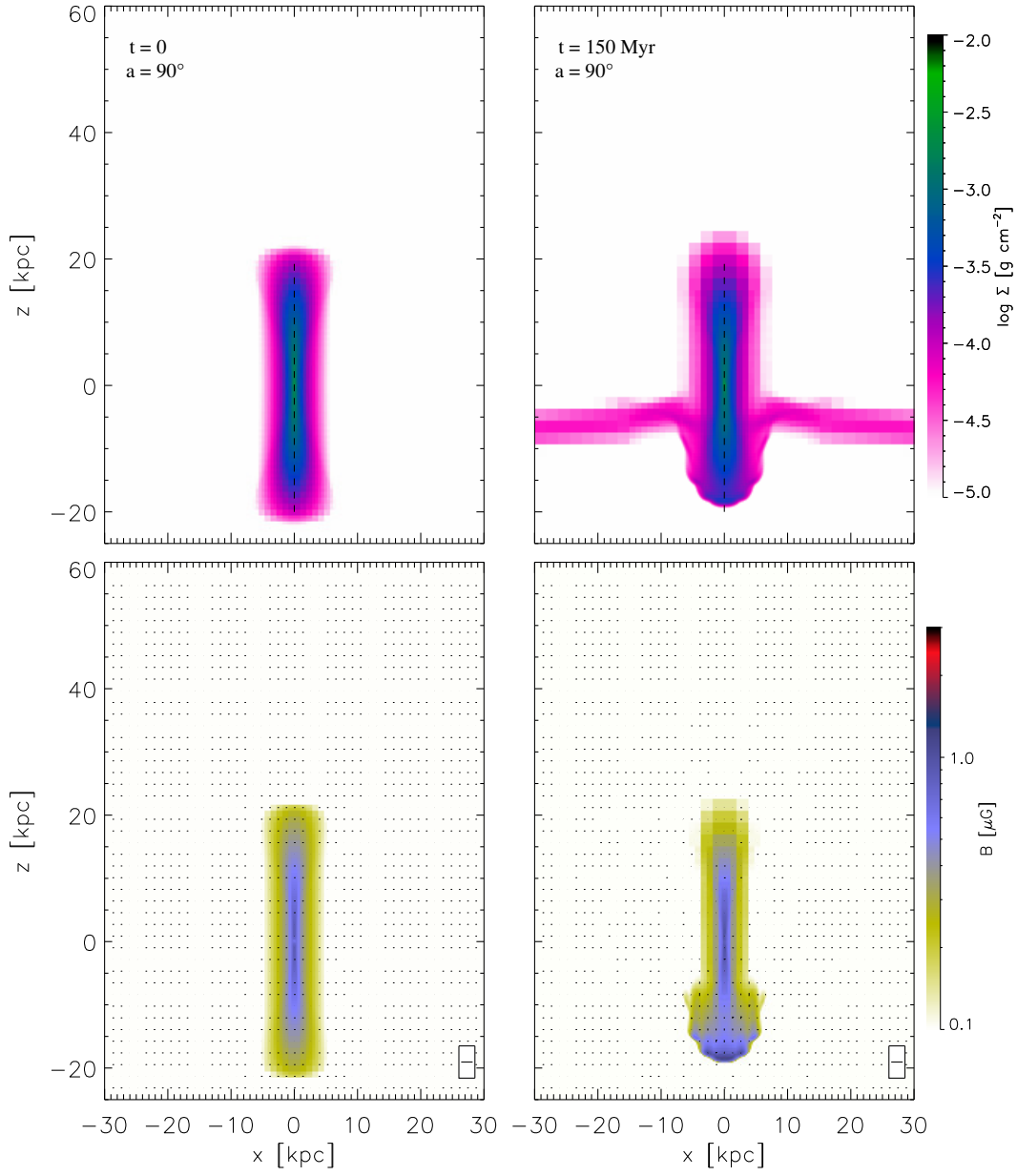

Figure 3.7: Same as fig. 3.3 for the Mod4 simulation at $t = 0\,\mathrm{Myr}$ (*left column*) and $t = 150\,\mathrm{Myr}$ (*right column*).

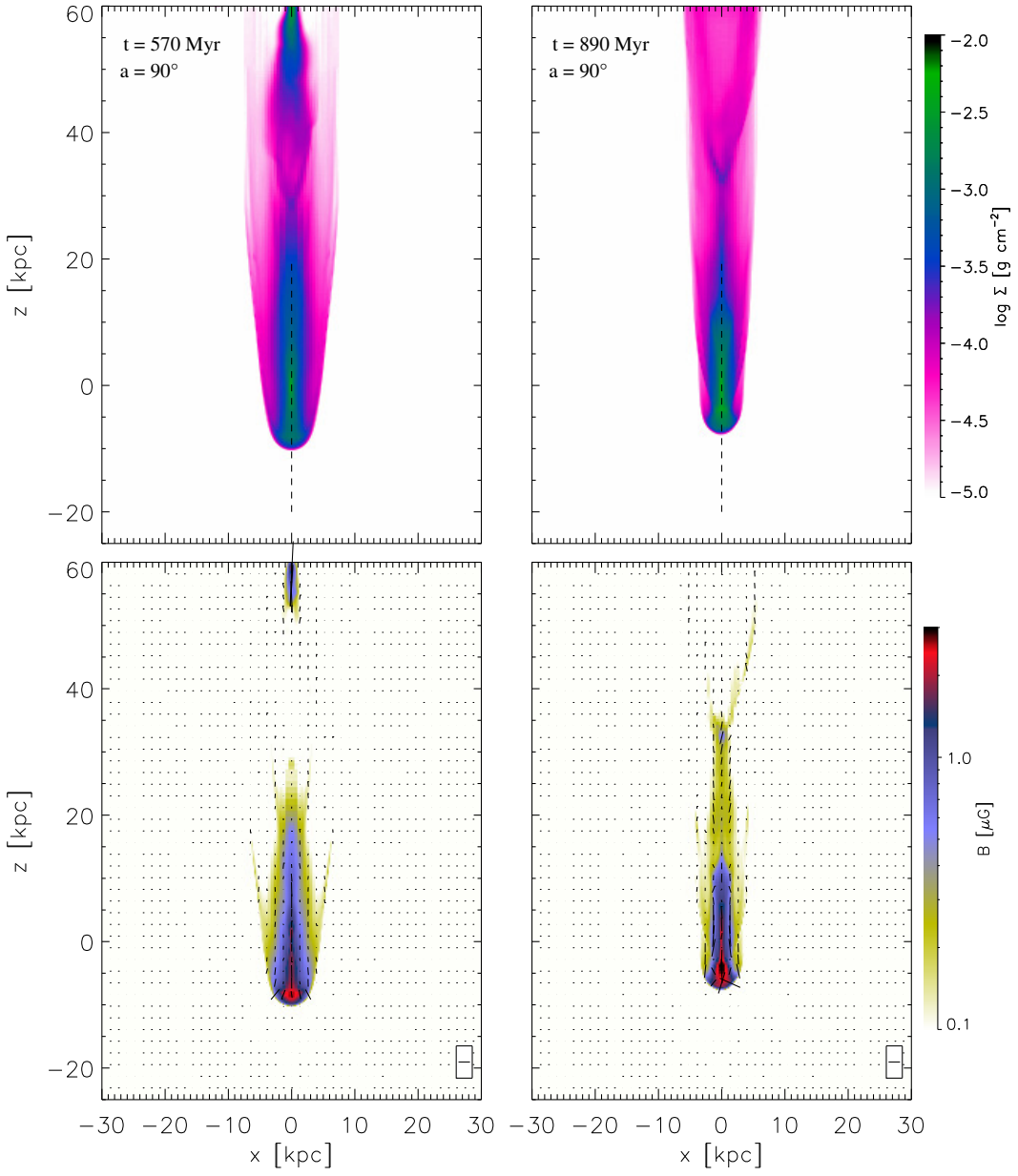

Figure 3.8: Same as fig. 3.7 for $t = 570\,\mathrm{Myr}$ (*left column*) and $t = 890\,\mathrm{Myr}$ (*right column*).

pressure has to compete against the circular velocity of the discs: if the wind reaches the portion of the disc where the gas sense of rotation has the same direction as the ram pressure, then the gas is stripped slightly easier and displaced farther of the galaxy; while in the side of the disc whose rotation opposes to the motion of the wind, the rotation itself prevents the gas of being swept and instead more material accumulates in that part of the galaxy, generating a shape similar to spiral arms, although in our set up the gas does not have self gravity.

In all the models, a remnant gaseous disc of size $r \lesssim 10\,\mathrm{kpc}$ is observed at the end of the simulation and all cases present an enhanced MF strength of $B \sim 2-3\mu G$ in the disc and on the leading side of the shock with the wind: in Mod1 and Mod2 is close to the galactic midplane, while in Mod3 and Mod4 in the leading side of the shock with the ICM ($z < 0$). The enhancement of the MF strength is a factor of ~ 3 compared to the initial condition. Observations of late-type spiral galaxies in clusters showed that they have a radio continuum emission enhanced by a factor up to ~ 5 compared to isolated spirals (Gavazzi & Jaffe 1986; Gavazzi & Boselli 1999) and this could be either by an increase in the star formation activity, producing more cosmic rays from supernovae, or an enhancement of the MF, or a combination of both.

To better determine in which model the ICM is magnetized the most, we calculate the magnetic energy outside the disc. Fig. 3.11 shows the magnetic energy E_{mag} as function of the volumetric density n for the swept gas, defined as gas located above a height $h > 5\,\mathrm{kpc}$ from the galactic midplane. In the case of low tilted discs (Mod1 and Mod2, top panels in fig. 3.11), the magnetic energy is spread through a wide range of values between 10^{47} to $10^{49}\,\mathrm{erg}$, reaching close to $10^{50}\,\mathrm{erg}$ in some cases. Also, since the gas of these models is stripped in ring-like features that evolve into a filamentary structure, the tails present regions of high and low density, hence we have a high number of cells extending over a range in densities of 10^{-4} to $\gtrsim 10^{-2}\,\mathrm{cm}^{-3}$ and with higher magnetic energy compared to Mod3 and Mod4 (bottom panels in fig. 3.11). For Mod3 and Mod4, we have less cells with magnetic energy $E_{\mathrm{mag}} \sim 10^{47} - 10^{48}\,\mathrm{erg}$ outside of the discs (also with low densities 10^{-4} to $10^{-3}\,\mathrm{cm}^{-3}$). However, the higher increase of magnetic energy in these models lies in the discs (not shown in the graphics of fig. 3.11) since the MF, compressed with the disc in the upstream side of the interaction, increases a factor of ~ 1.2 compared to Mod1 and Mod2. From this simulations it is observed that (nearly) face-on disc-wind interaction tend to magnetize more the ambient than (nearly) edge-on models.

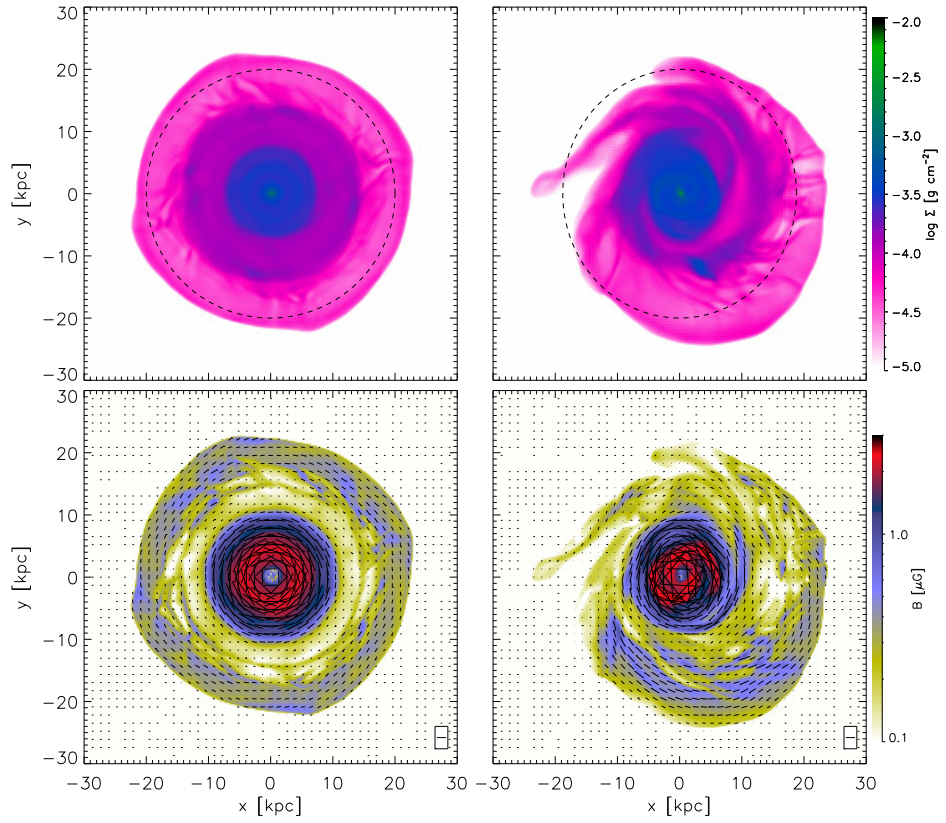

Figure 3.9: Gas surface density (*top row*) and magnetic field strength (*bottom row*) for Mod1 (tilted at 0^{o}, *left column*) and Mod2 (tilted at 20^{o}, *right column*) at $t = 890\,\mathrm{Myr}$ in the xy-plane. The dashed lines in the top panels represents the initial size of the disc: $r = 20\,\mathrm{kpc}$. The box in the bottom panels shows an MF line with a strength of $0.5\mu G$.

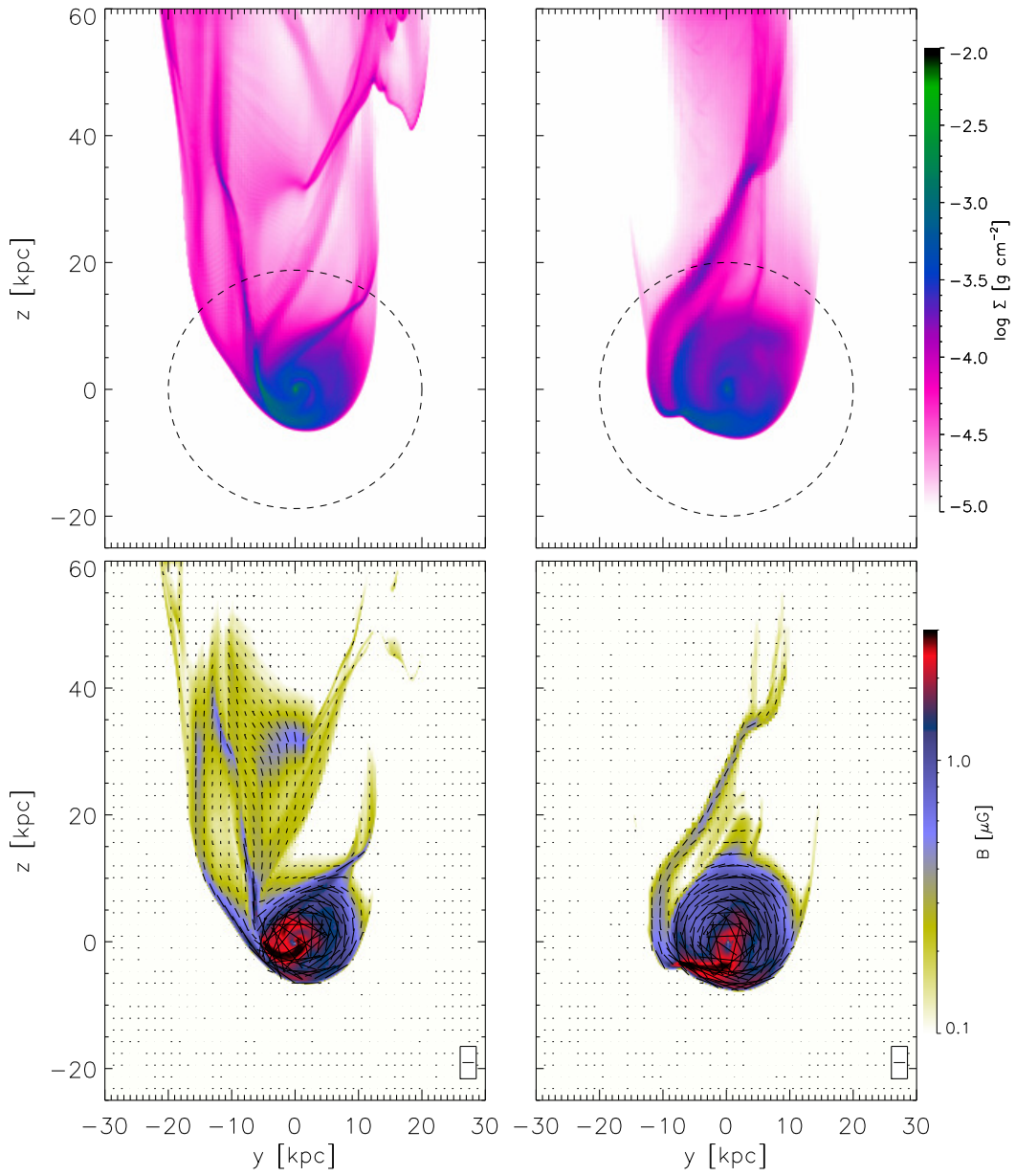

Figure 3.10: Same as fig. 3.9, for Mod3 (tilted at 70^{o}, *left column*) and Mod4 (tilted at 90^{o}, *right column*).

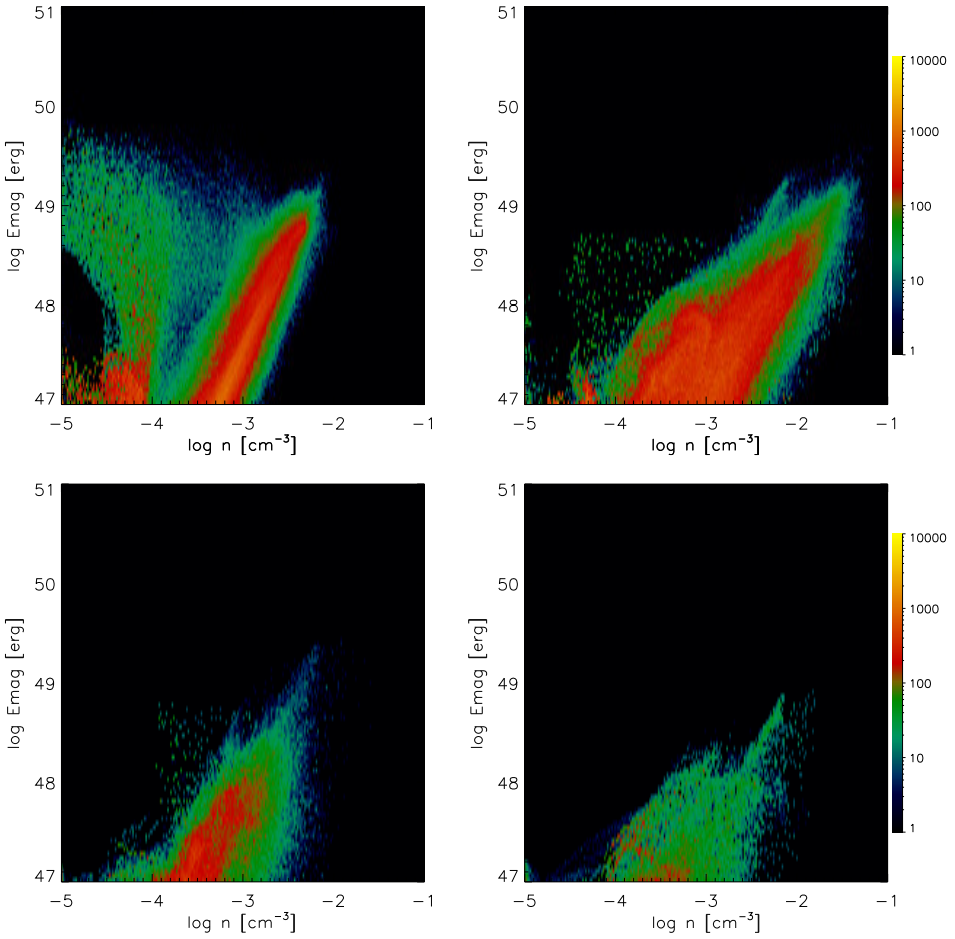

Figure 3.11: Histograms of magnetic energy and density at $t = 890\,\mathrm{Myr}$ for the four runs: disc tilted at 0^{o} (*top left*), 20^{o} (*top right*), 70^{o} (*bottom left*) and 90^{o} (*bottom right*) respectively.

3.3.1 Magnetic field lines

As mentioned, in the (nearly) face-on models the gas is removed in ring-like structures dragging the MF with it and, as time goes by and the wind accelerates, the rings are perturbed by the wind and filaments appear along the gas tail. In figs. 3.2 and 3.4 (bottom right in both images) it can be observed, on an xz view, that the MF lines are aligned with the filaments, similarly to the results obtained by Ruszkowski et al. (2014). On a view over the xy-plane from figs. 3.9 (bottom panels), the MF lines still keep their initial circular configuration, such that these are distorted in the z-axis, parallel to the wind motion. However, Mod2 shows some asymmetries for the distribution of the MF lines (lower right panel in fig. 3.9) that are probably due to projection effects or the inclination of the disc.

In the case of the (nearly) edge-on models (Mod3 and Mod4), when the discs are seen in the xz-plane (lower panels in figs. 3.6 and 3.8), the MF lines resemble a water fountain: they have a concave shape in the upstream side and wrap around the disc at higher $|z|$ since the wind flows parallel or nearly to the plane of the disc and sweeps the gas above and below the galaxy midplane more easily than gas closer to the galactic plane. Observing these models on the yz-plane in figs. 3.10 (bottom panels), the MF is compressed in the upstream side and more extended by the wind in the downstream side giving an ellipsoid morphology to the MF lines. Similarly to Mod2, this effect is more evident in Mod3 due to the inclination of the disc.

3.4 Synthetic synchrotron emission and polarization

The total synchrotron emission of the models is obtained by integrating the emissivity:

$$\varepsilon \propto n_{\rm cr} B_{\perp}^{(p+1)/2}\,, \tag{3.6}$$

where $n_{\rm cr}$ is the cosmic ray electrons (CR) density distribution, $B_{\perp}$ is the MF component perpendicular to the line of sight (LOS), and $p = 2.5$ is the spectral index of the distribution of cosmic ray electrons. Here, $n_{\rm cr}$ is assumed constant since it is expected that the less energetic CRs, with a gyroradius smaller than the size of the galaxy, are dragged with the MF when the wind is sweeping the material (additionally, the distribution of the CRs at high z is uncertain; Ferrière 1998).

Fig. 3.12 shows the synchrotron emission (contours normalized to its maximum value) over the gas surface density for all the models at $t = 570\,\mathrm{Myr}$. The

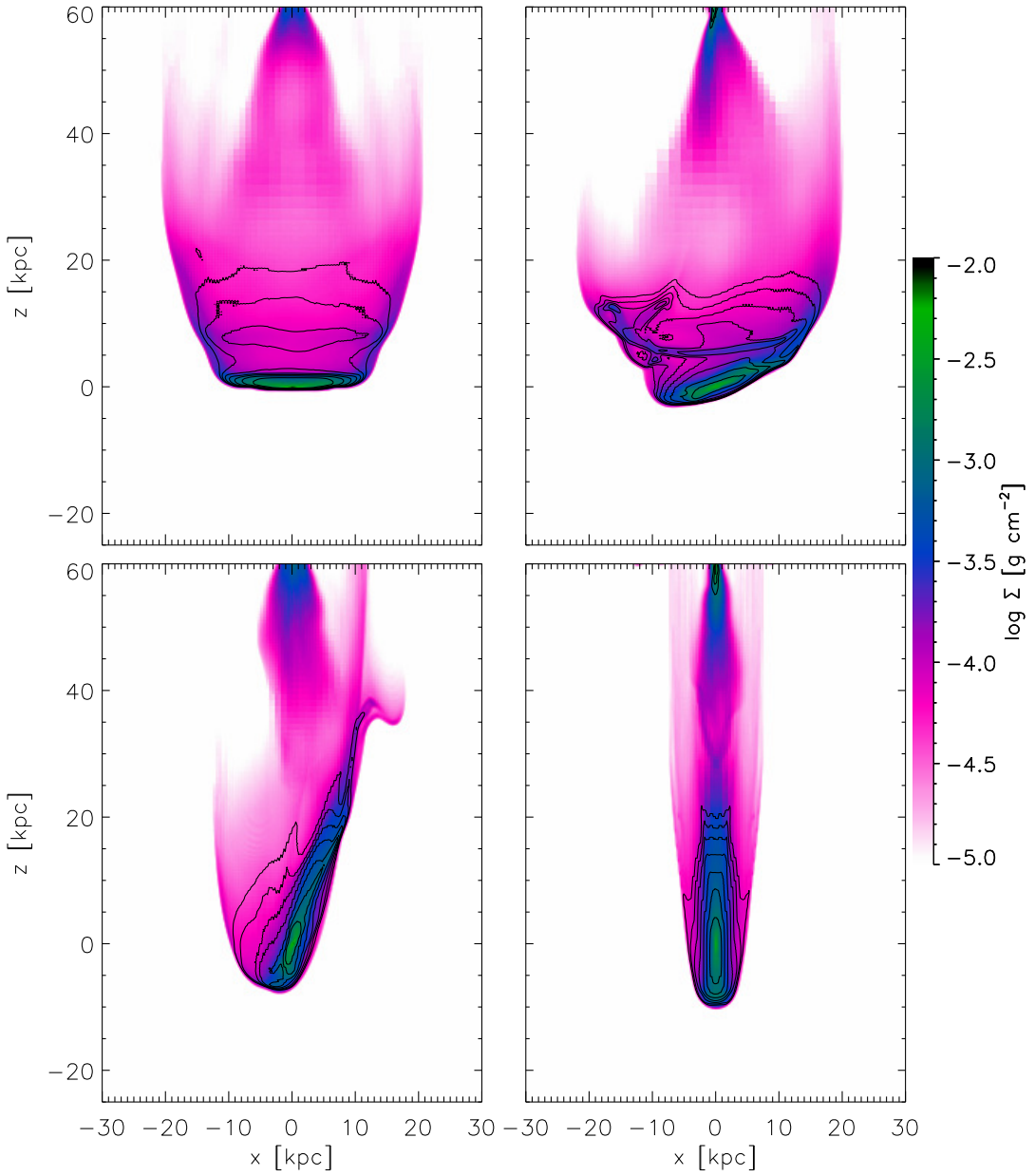

Figure 3.12: Total synchrotron emission distribution on a gas surface density map at $t = 570\,\mathrm{Myr}$ for the four models: disc tilted at 0 (*top left*), 20 (*top right*), 70 (*bottom left*) and 90$^{\mathrm{o}}$ (*bottom right*), respectively. The synchrotron emission is displayed in contours normalized to its maximum values and with levels $-2, -1.75, -1.5 - 0.75$ and -0.5 in log-scale. The gas surface density projected along the y-axis.

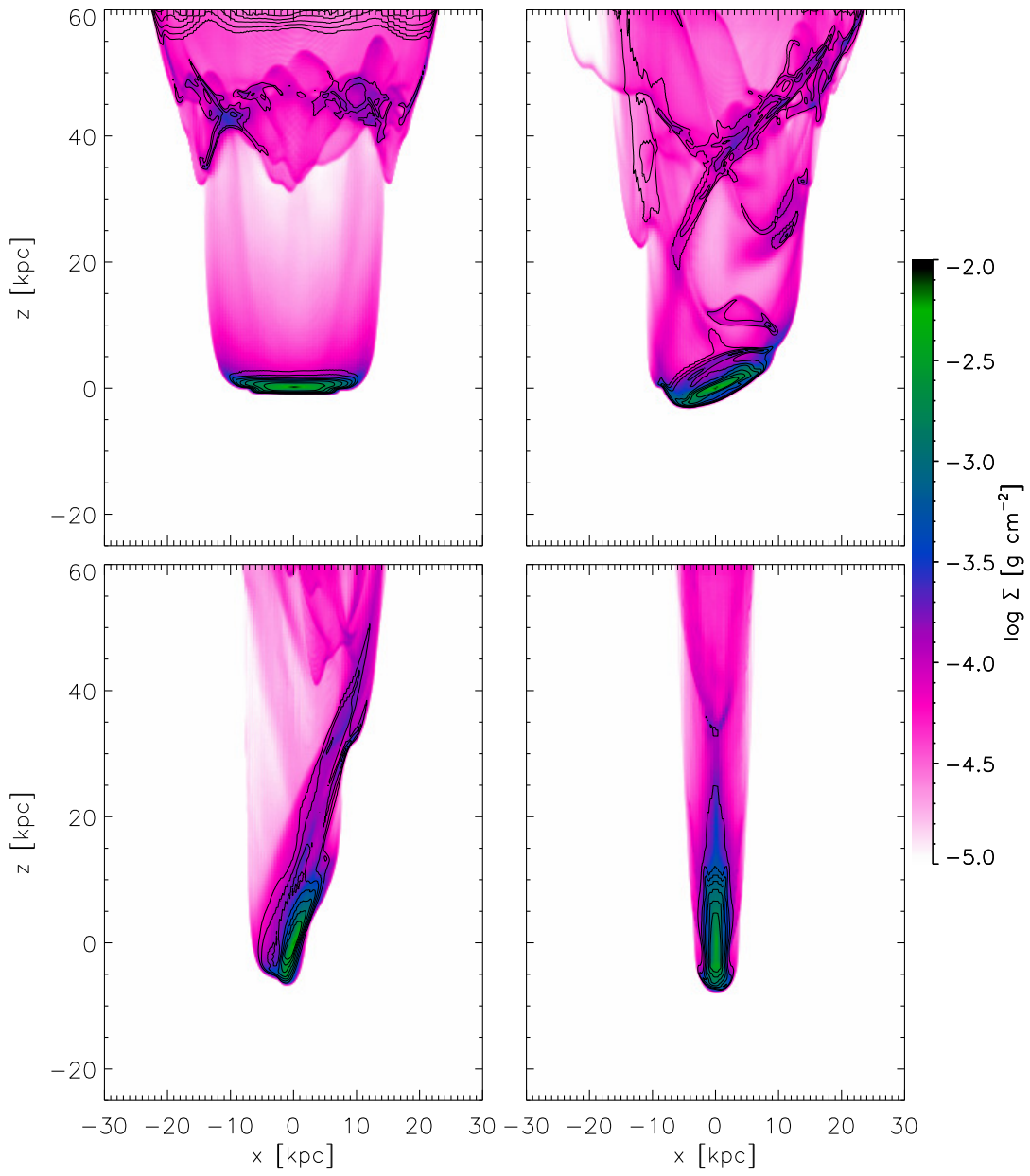

Figure 3.13: Same as fig. 3.12, for $t = 890\,\mathrm{Myr}$.

distribution of the synchrotron emission is asymmetric. On the side of the galaxy that is facing the ICM wind, the emission is compressed with sharp edges while in the opposite side it is extended developing a synchrotron tail. However, the distribution in Mod1 and Mod2 (top panels in fig. 3.12) presents larger and broader tails than in Mod3 and Mod4 (bottom panels in fig. 3.12). The distribution of the total synchrotron emission at $t = 570$ is similar to the one observed in some Virgo Cluster galaxies, e.g. Mod1 and Mod2 with NGC 4522 (fig. 3.14) or NGC 4330 (fig. 3.15) given that is truncated with the gaseous disc and spans on the opposite direction, and Mod3 and Mod4 with NGC 4396, NGC 4402, and NGC 4654 (Vollmer et al. 2010, also see fig. 3.16). At $t = 890\,\mathrm{Myr}$ (fig. 3.13), all models have developed longer synchrotron tails as the wind swepts the gas from disc and drags the magnetic field. Although most of the emission lies in the discs, it can be also observed along the tails in $z > 20\,\mathrm{kpc}$. In Mod1 and Mod2 (top panels in fig. 3.13) at $z > 20\,\mathrm{kpc}$, the densest knots and filaments show synchrotron emission. The emission in Mod3 and Mod4 (bottom panels in fig. 3.13) is mostly present in the disc since the downstream side is not as magnetized as in Mod1 and Mod2 (see 3.3). In Mod3, there is some emission in $z > 20\,\mathrm{kpc}$ because the wind not only removes gas from the side of the disc that is interacting with it first (between $x < 0$ and $z < 0$) but also from the part of the disc that is behind of the interaction ($x > 0$) developing a denser gaseous tail with a stronger MF intensity and hence a stronger synchrotron emission that in Mod4, where the gas is mainly removed from above and below the galactic midplane (located in $x = 0$ for this case) resulting in a thinner tail with low MF intensity and synchrotron emission.

It was also calculated the synchrotron emission from other LOS, e.g. along the z-axis for Mod1 and Mod2 and the x-axis for Mod3 and Mod4. The different directions for the LOS were chosen to be able to observe the entire disc surfaces. Fig. 3.17 shows the synchrotron emission of Mod1 (left) and Mod2 (right) when integrating the emissivity along the z-axis, where it can be seen from the contour that the synchrotron is approximately symmetric at $|x| \lesssim 10\,\mathrm{kpc}$ which is the emission form the remnant disc while at larger radii ($|x| > 10\,\mathrm{kpc}$) is the projected distribution of gas and synchrotron from the filaments. In fig. 3.18 the synchrotron emission for Mod3 (left) and Mod4 (right) is sharp on the leading side of the wind-disc interaction and extended over the opposite side along with the wind motion. There is also emission in filaments of the tails that resemble an unwinded spiral structure.

3.4.1 Polarization

To determine the direction of the polarization vectors, the emissivity parallel to the MF component in the plane of the sky $B_\perp$ is calculated as follows:

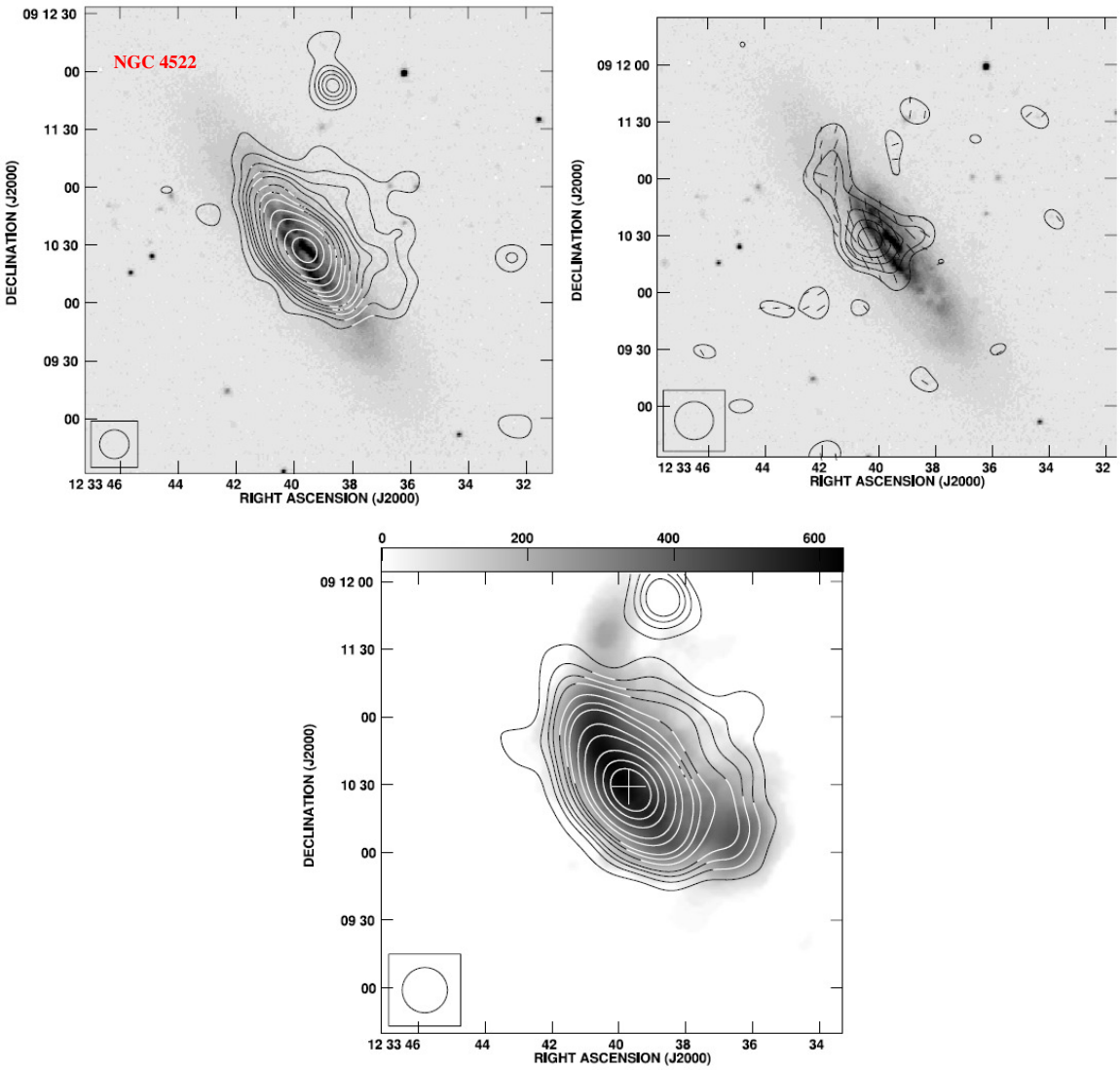

Figure 3.14: NGC 4522. *Top left*: contours of the 6 cm total continuum emission on an *R*-band image (grey scale). *Top right*: 6 cm polarized intensity (contours) and *B*-vectors on an *R*-band image (grey scale). *Bottom*: HI gas distribution (grey scale) with 6 cm total emission (contours). The cross marks the galaxy centre. (from Vollmer et al. 2004).

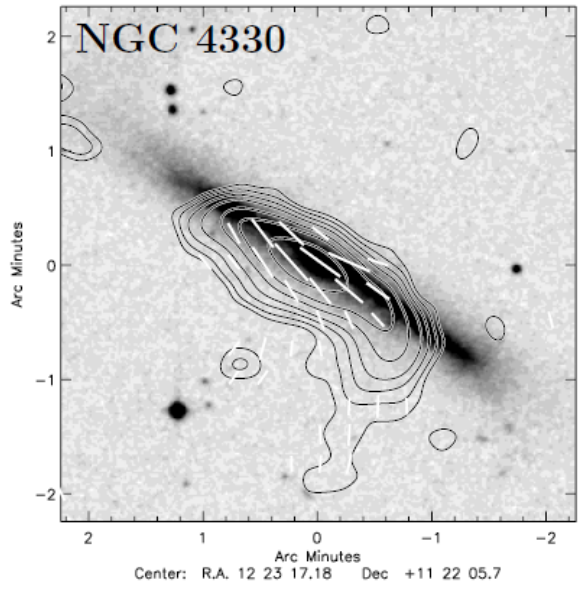

Figure 3.15: NGC 4330. Contours of the 6 cm total continuum emission on a B-band image (grey scale) with B-vectors (white). (from Vollmer et al. 2013).

$$\varepsilon_{\parallel} = \varepsilon_{tot} \times \frac{(1+\Pi)}{2}\,, \tag{3.7}$$

where ε_{tot} is the total emissivity from eq. 3.6 and $\Pi = (p+1)/(p+7/3)$ is the degree of polarization of the emissivity. First, the emissivity over the y-axis is integrated in order to obtain the polarization vectors on the xz-plane. The parallel intensity over the y-axis is given by

$$I_{\parallel,x}(y+dy) = I_{\parallel}(y)\cos(\alpha) + \varepsilon(y)dy\cos(\alpha) = I_{\parallel}(y+dy)\cos(\beta) \tag{3.8}$$
$$I_{\parallel,z}(y+dy) = I_{\parallel}(y)\sin(\alpha) + \varepsilon(y)dy\sin(\alpha) = I_{\parallel}(y+dy)\sin(\beta)\,, \tag{3.9}$$

where α is the direction of $B_{\perp}$ measured in the x-axis and β is the direction of the inferred B-field,

$$\beta = \arctan\left(\frac{\int \varepsilon_{\parallel}\sin(\alpha)dy}{\int \varepsilon_{\parallel}\cos(\alpha)dy}\right)\,. \tag{3.10}$$

For the polarization vectors on the disc surface, that is, the xy-plane, $\varepsilon_{\parallel}$ was integrated over the z-axis.

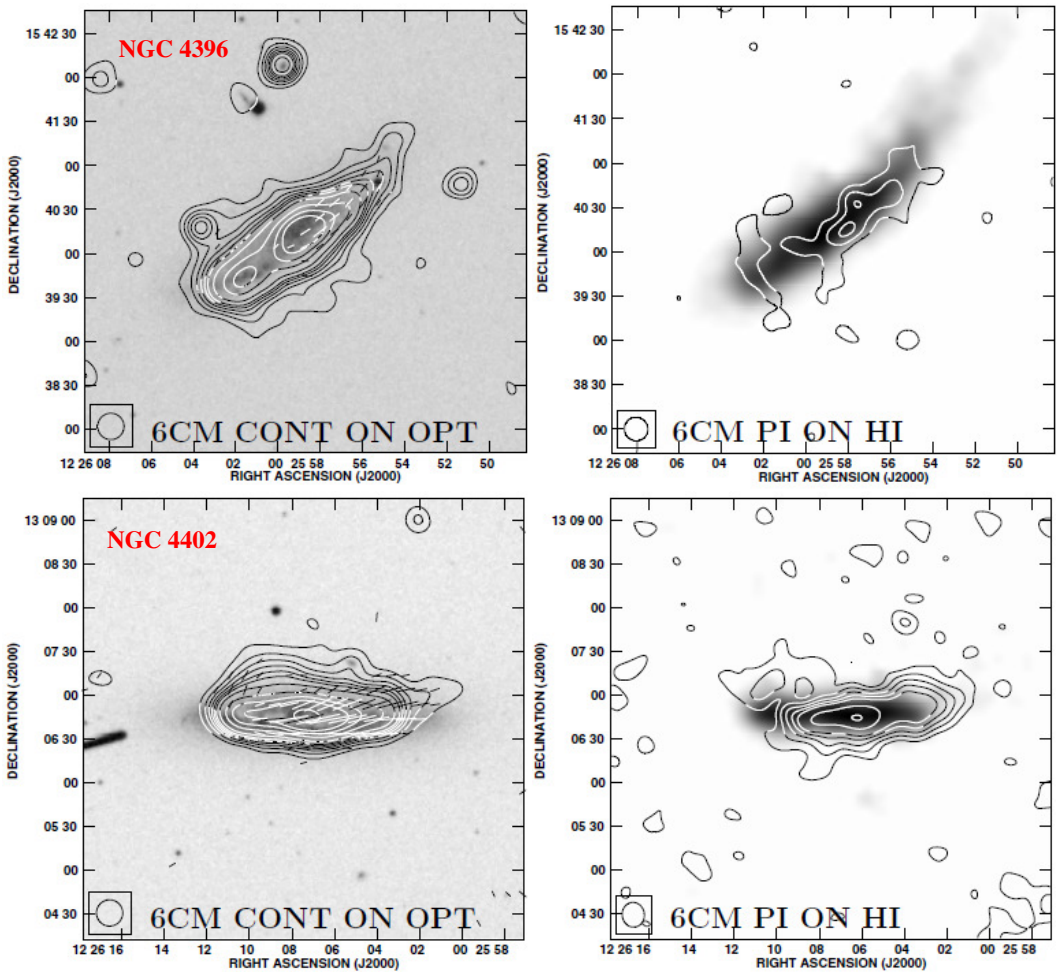

Figure 3.16: NGC 4396 (*top panels*) and NGC 4402 (*bottom panels*). *Left*: contours of the 6 cm total continuum emission on a B-band image (grey scale) and B-vectors. *Right*: HI gas distribution (grey scale) with 6 cm polarized intensity in contours. (from Vollmer et al. 2010).

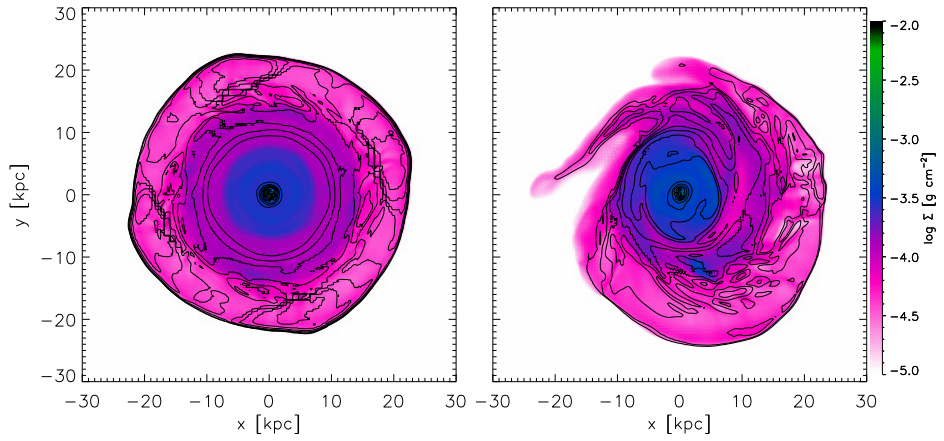

Figure 3.17: Total synchrotron emission distribution on a gas surface density map at $t = 890\,\mathrm{Myr}$ for Mod1 (0^{o}, *left*) and Mod2 (20^{o}, *right*). The synchrotron emission is displayed in contours normalized to its maximum values and with levels $-2, -1.75, -1.5 - 0.75$ and -0.5 in log-scale. The gas surface density projected along the z-axis.

Fig. 3.19 shows the B-vectors overlaid on maps of the surface density for the four runs at $t = 570\,\mathrm{Myr}$. For the (nearly) face-on models, Mod1 and Mod2 in the upper panels, the B-vectors are parallel to disc surface up to $\sim 10\,\mathrm{kpc}$ above the galactic midplane. Farther from the disc they are distorted along the wind motion, since in these models the field is dragged by the swept gas in the shape of rings, as mentioned in sections 3.3 and 3.3.1. In the highly tilted discs, Mod3 and Mod4, lower panels of fig. 3.19, the B-vectors are also parallel to the disc on the radial direction, although on the leading side of the interaction they show a water fontain morphology as in the bottom panels of figs. 3.6 and 3.8, i.e., they are concave in the shock front and then wrap around the disc at $z > 0$.

At $t = 890\,\mathrm{Myr}$ (fig. 3.20), the B lines have more random orientations in the tails of the two nearly face-on models (top panels) but still they tend to be aligned with the gas filaments and in the remnant disc the lines remain parallel to the disc surface lines. Mod3 and Mod4 (bottom panels) have evolved more pasively since they show the same distribution during the simulation: on the downstream side the B lines run parallel along the elongated disc and tail while in the leading side they have a water fountain or concave shape. For the highly inclined discs, the field lines in the upstream side have a curved morphology and appear as if were shielding the galaxy. The distribution of the field for Mod3 and Mod4 is due to the way the discs

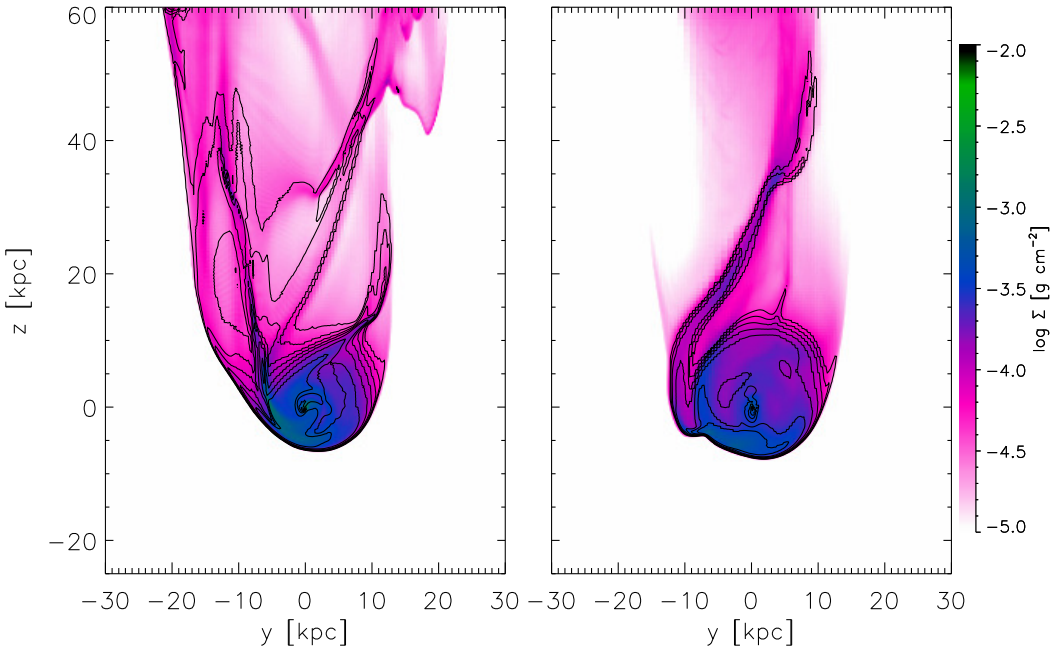

Figure 3.18: Same as fig. 3.17 for Mod3 and Mod4.

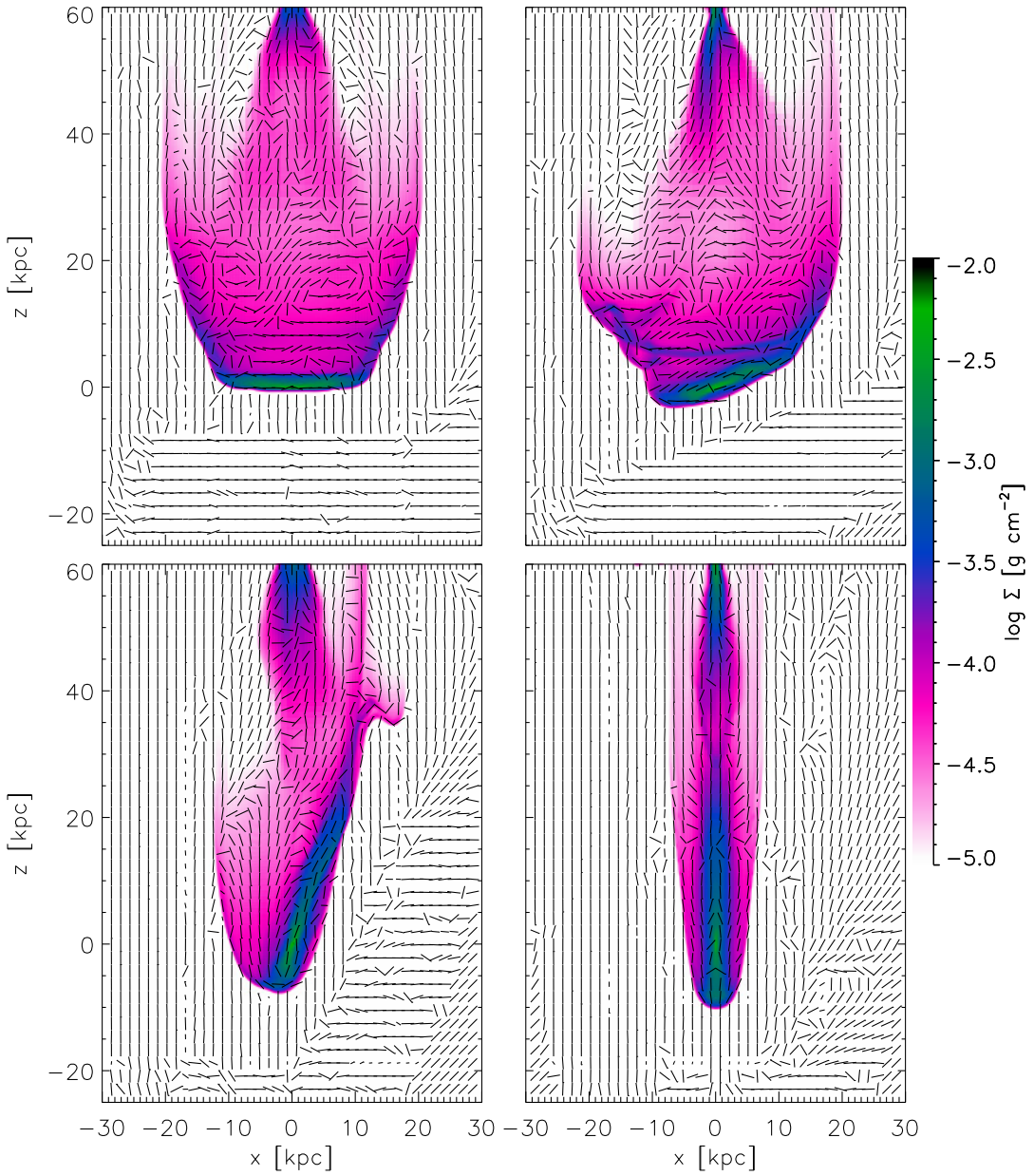

Figure 3.19: B-vectors inferred from the polarization of the synchrotron emission on a gas surface density map at $t = 570\,\mathrm{Myr}$ for the four runs: Mod1 at 0^{o} (*top left*), Mod2 at 20^{o} (*top right*), Mod3 at 70^{o} (*bottom left*) and Mod4 at 90^{o} (*bottom right*), respectively. The gas surface density is projected along the y-axis.

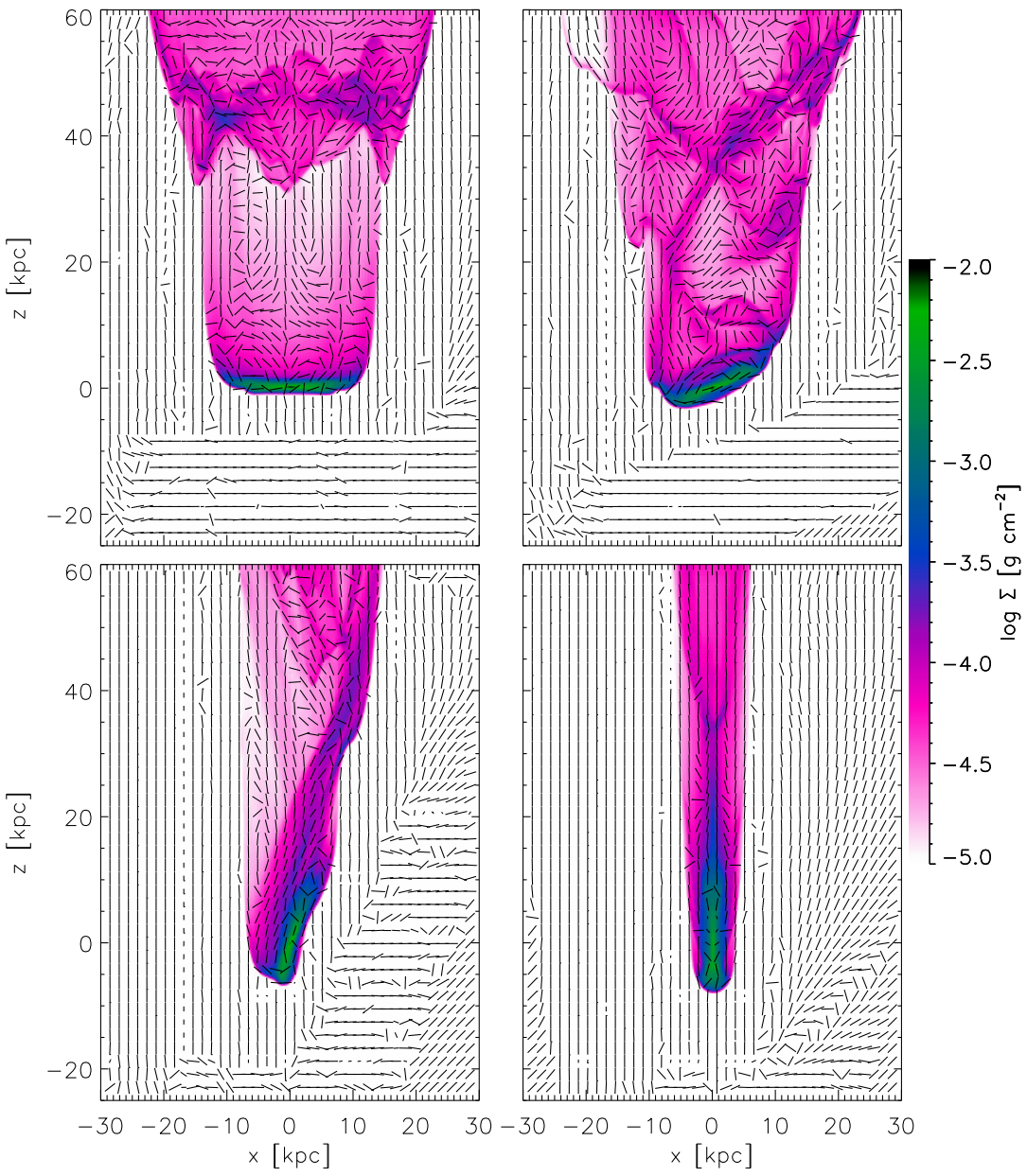

Figure 3.20: Same as fig. 3.19 for $t = 890\,\mathrm{Myr}$.

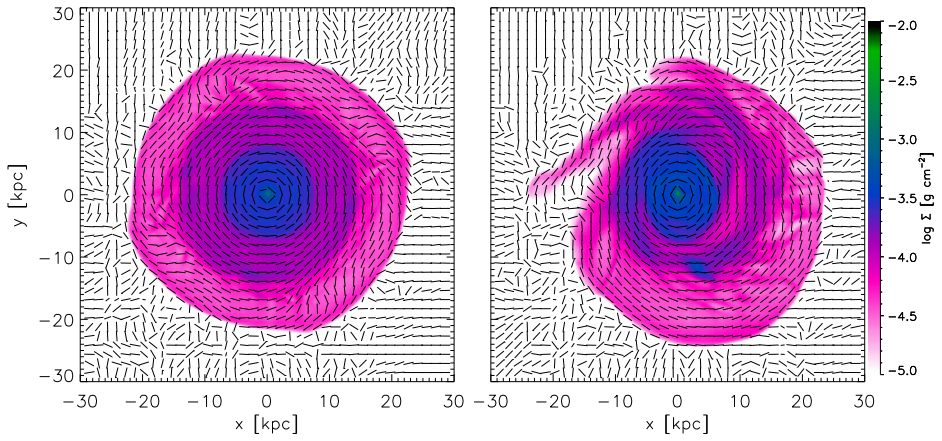

Figure 3.21: *B*-vectors inferred from the polarization of the synchrotron emission on a gas surface density map at $t = 890\,\mathrm{Myr}$ for Mod1 (0^{o}, *left*) and Mod2 (20^{o}, *right*). The gas surface density is projected over the z-axis.

are eroded, since the wind removes the gas above and below the galactic midplane, then the lines open on the leading side and wrap around the disc on the downstream side following the wind motion (see discussion in section 3.3.1).

The *B*-vectors are calculated for face-on views of the models and are shown in the fig. 3.21 for Mod1 and Mod2 models. They have a toroidal distribution with slight deviations between $r = 15 - 20\,\mathrm{kpc}$, at the filaments location, which means that the MFs remains circular in nearly face-on interactions but is perturbed in the vertical direction by the wind when its displaced with the gas. In Mod3 and Mod4 (fig. 3.22), although the lines are toroidal in the disc, with $r \lesssim 10\,\mathrm{kpc}$ and surface density $\Sigma \gtrsim 10^{-3.5}\,\mathrm{g\,cm^{-2}}$, they tend to elongate along the z-axis, similar to ellipses with its major axis parallel to the wind motion. Also, in the two nearly edge-on models a spiral structure appears that spreads outside the disc to the downstream side (in the $+z$ direction), where the *B*-field also lines up vertically.

3.5 Conclusions

In this chapter, MHD simulations of four tilted galaxies undergoing RPS were presented in order to analyze the effects of the disc inclination in the gas removal. The inclination angle of the discs with respect to the $z = 0$ plane: $0, 20, 70$ and 90^{o}, which are denominated Mod1, Mod2, Mod3 and Mod4, respectively.

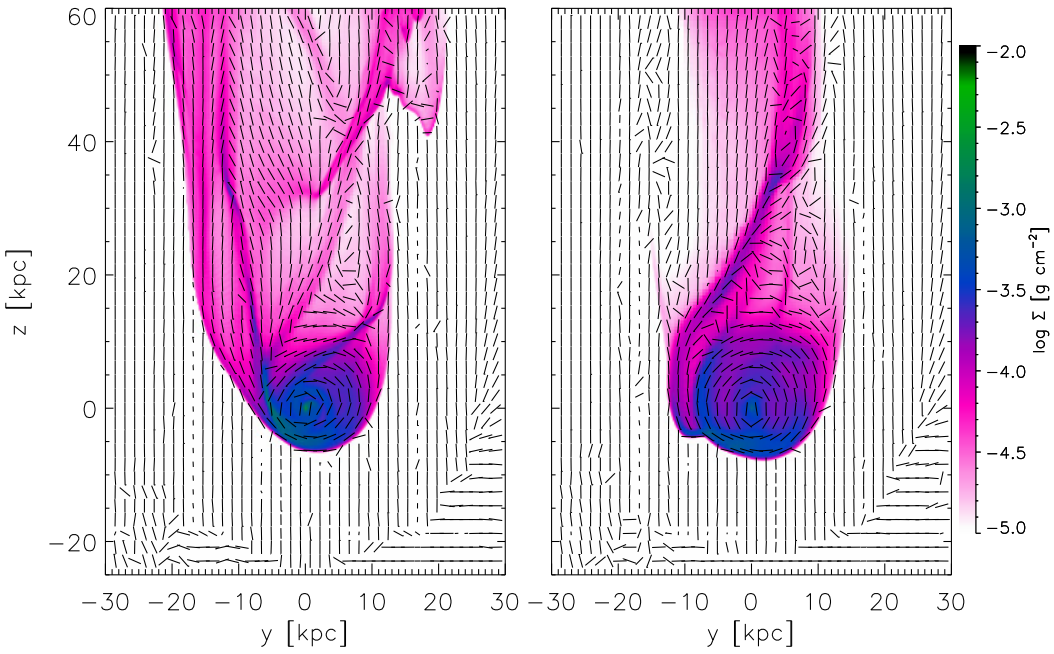

Figure 3.22: Same as fig. 3.21 for Mod3 ($70^{\rm o}$, *left*) and Mod4 ($90^{\rm o}$, *right*).

Once the ICM-wind starts to interact with the galaxies, it is observed that in models with (nearly) face-on geometry with respect to the wind motion, the gas is removed in ring-like structures and, since the MF and the gas are bound, the MF is also dragged by the wind. When the wind starts to remove gas from the disc, the rings of gas run parallel to the galactic plane up to $10 - 20\,\mathrm{kpc}$ above the disc at $t \gtrsim 500\,\mathrm{Myr}$ with $B \approx 0.4 - 0.7\mu G$. When the gas is displaced farther from the galactic plane, the rings get distorted along the direction of the wind giving a filamentary structure to the tails, where also the MF is aligned with the filaments and since these are the densest structures in the tails, here the MF reaches its highest strength outside the discs, from $B \approx 0.3 - 0.4\mu G$ to $0.7\mu G$. In this interaction, the MF preserves its initial toroidal configuration during most of the time of the simulations with slight deviations in the region where the filaments are. For the nearly edge-on models, the MF lines emerge outside to the galactic plane in a "water fountain" shape wraping around the disc in the downstream side (at high z): the MF lines have an elipsoid structure in the disc that is compressed in the upstream side and elongated in the downstream side. The tails in these models are not so prominent nor do they magnetize so much the surroundings, reaching values of $B \lesssim 0.2 - 0.3\mu G$. Edge-on models also develop a spiral structure in the disc that spreads downstream pushed by the wind, similar to the results of (Tosa 1994) where a single-arm appears in an edge-on ram pressure stripped galaxy.

It was also obtained synchrotron emission maps and the B-vectors inferred from the polarization. The synchrotron emission presents an asymmetric distribution that is truncated in the disc and spreads out on the downstream side, following the gas. The maps of the emission from these simulations obtained at $t = 570\,\mathrm{Myr}$ resemble the shape of the synchrotron tails of some Virgo galaxies, e.g. NGC 4522 (Vollmer et al. 2004), NGC 4330 (Vollmer et al. 2013), NGC 4396, NGC 4402, and NGC 4654 (Vollmer et al. 2010), despite the restrictions of the models presented in this work. The B-vectors trace very accurately the MF of the simulations: they line up with the filaments of gas observed in face-on interactions and follow the compressed gas in the upstream side of the disc and are more elongated in the downstream side of the edge-on models. Since the MFs lines in these simulations change depending on the disc inclination, the distribution of the synchrotron and the B-vectors inferred from the polarization can have also information of the wind direction in galaxies travelling through a cluster. Additionally, the gas is easy to perturb in tidal interactions or RPS, so it will still be reflected on the MFs through compression or shear motions, leaving an imprint in the synchrotron and polarization emission.

Chapter 4

Future work

This chapter presents future and in-progress work. Here are addressed additional aspects that can be compared with observations of galaxies undergoing ram pressure stripping (RPS).

4.1 Gas kinematics

When gas is removed from a galaxy and the tail appears, the displaced gas retains some rotation while it is pushed away from the galaxy. In observations of stripped galaxies, one way to estimate the rotation curve is with emission lines of neutral (21 cm) or ionized gas (Hα). Stripped galaxies have asymmetric distributions of HI, the gas in the disc is truncated and extended in one side of the galaxy and, for measuring the rotation curve, it is assumed that the swept gas is still rotating with the same velocity it had while it was on the disc. The figs. 4.1 and 4.2 show the velocity maps of the four models at $t = 570\,\mathrm{Myr}$ and $t = 890\,\mathrm{Myr}$, respectively. Then the circular velocity of the gas is measured in the galactic midplane and at different heights in the tails for $t = 570\,\mathrm{Myr}$ and $t = 890\,\mathrm{Myr}$ which is shown in the position-velocity diagrams of figs. 4.3, 4.4, 4.5, and 4.6 for each model. In the tilted disc models (Mod2, Mod3, and Mod4), the disc is rotated so that the galactic midplane coincides with the $z = 0$ plane. It is also compared how much the gas velocity deviates of the velocity obtained from the gravitational potential. From these diagrams, it can be seen that the circular velocity of the gas decreases from that of the midplane value with increasing height above the disc. In the models Mod3 and Mod4, the gas in the disc increases its velocity on the leading side due to the contribution of the wind, since the circular velocity has a component parallel to the ICM motion.

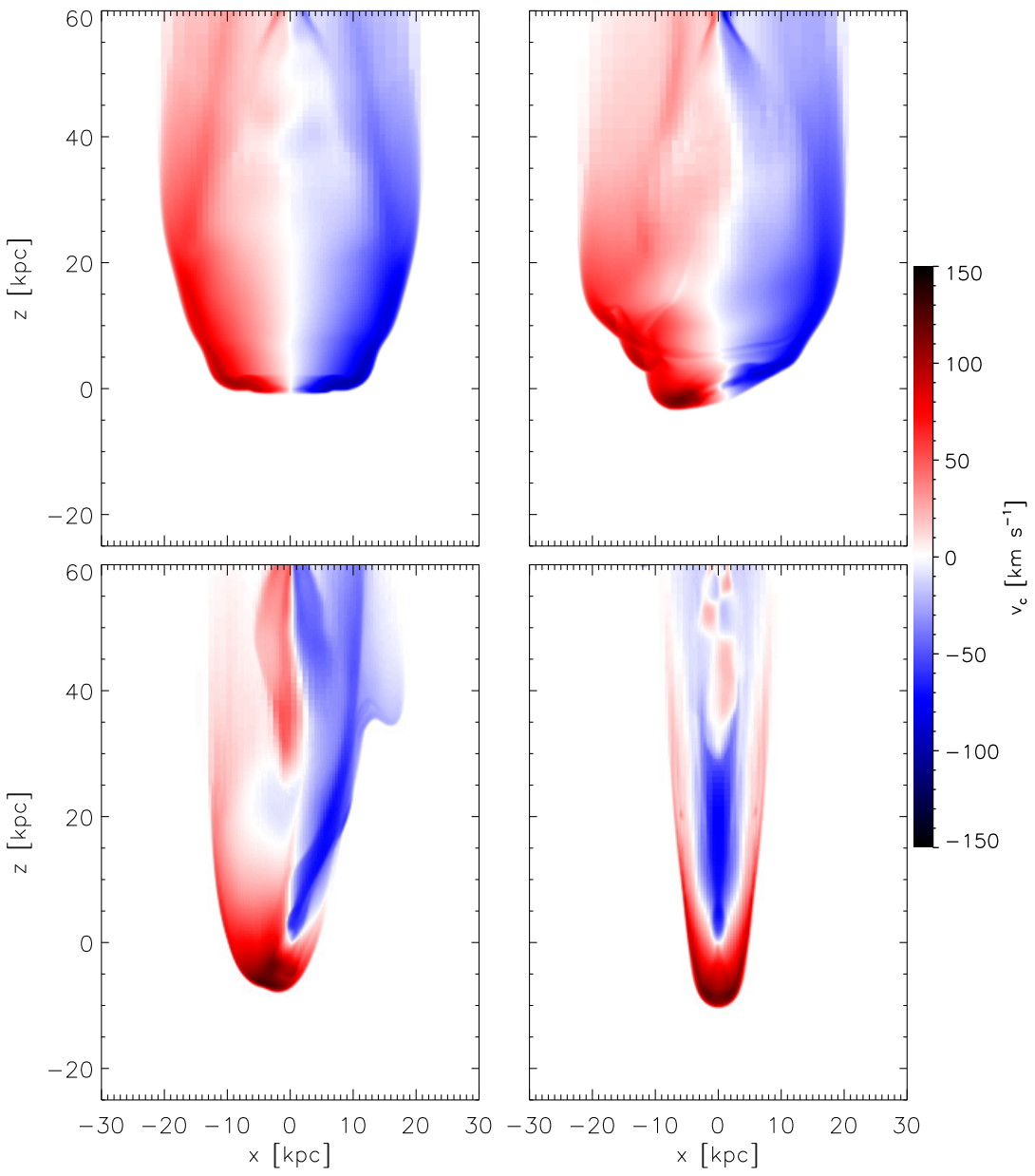

Figure 4.1: Velocity maps projected over the y-axis at $t = 570\,\mathrm{Myr}$ for Mod1 (*Top left*), Mod2 (*top right*), Mod3 (*bottom left*) and Mod4 (*bottom right*).

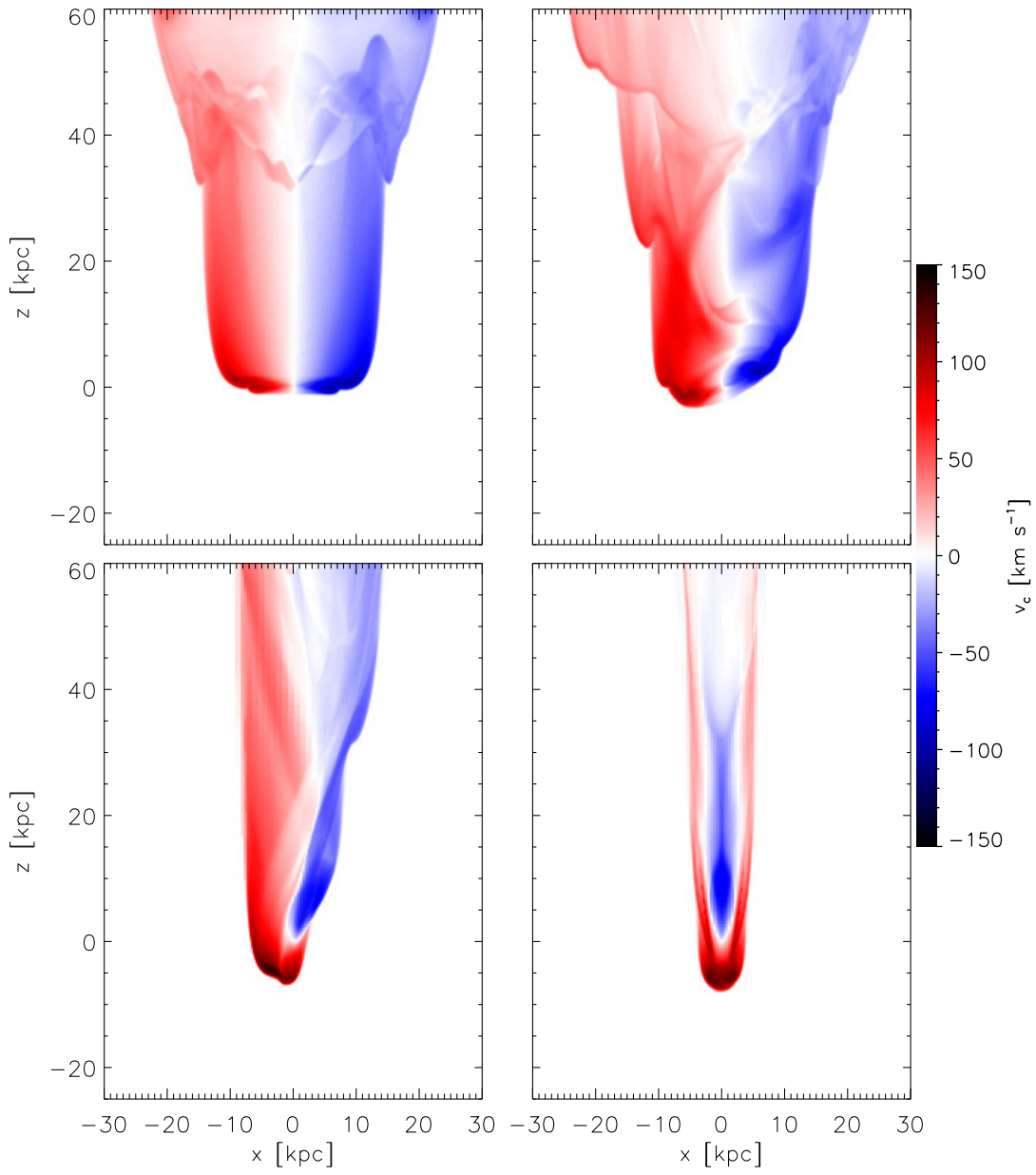

Figure 4.2: Same as in fig. 4.1 for $t = 890\,\mathrm{Myr}$.

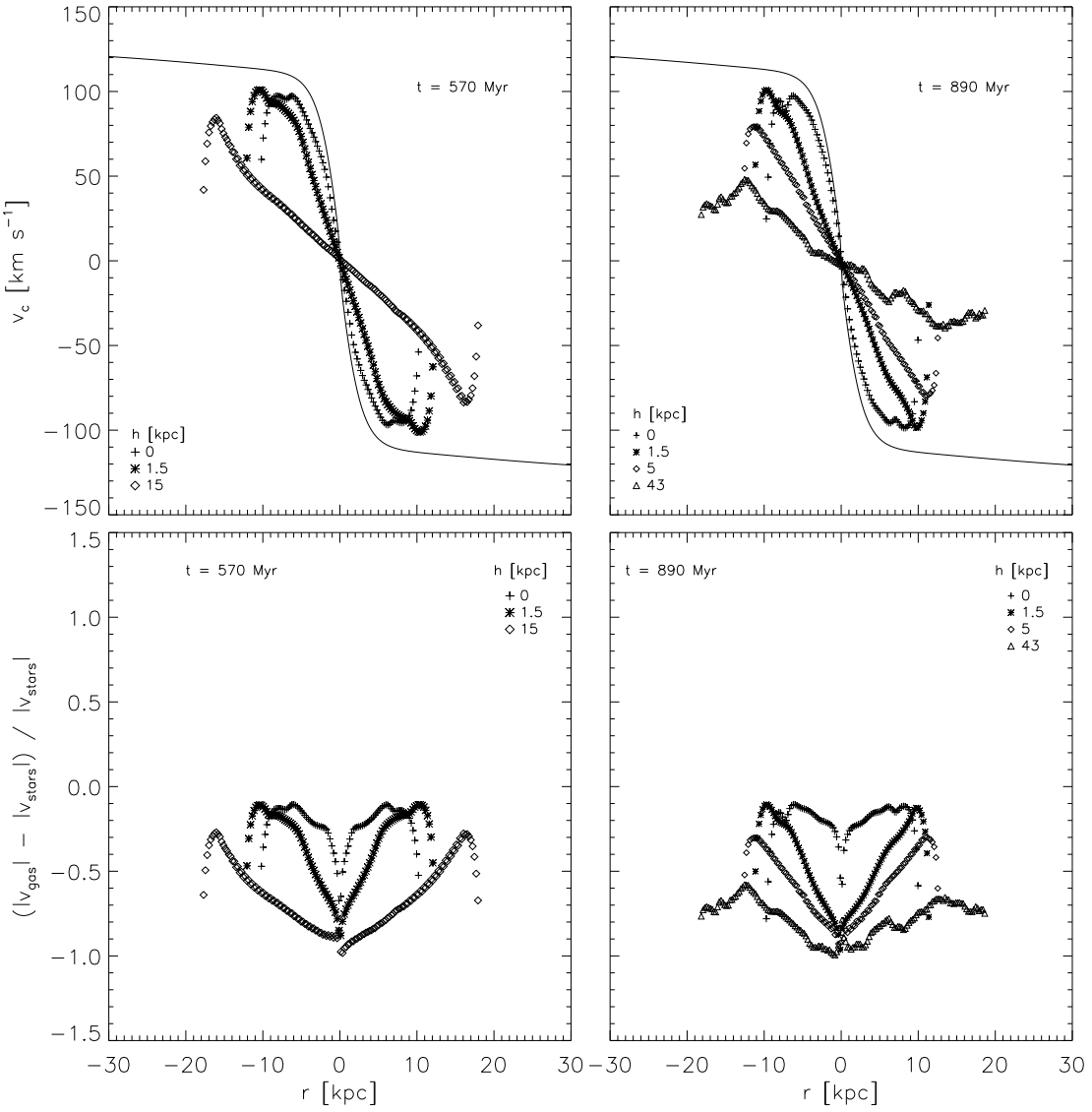

Figure 4.3: *Top:* Position-velocity diagrams for the gas of Mod1 at $t = 570\,\mathrm{Myr}$ (*left*) and $t = 890\,\mathrm{Myr}$ (*right*) at different heights from the galactic midplane with the circular velocity obtained from the (background) gravitational potential (*solid line*). *Bottom*: Gas velocity deviation with respect to the midplane circular velocity.

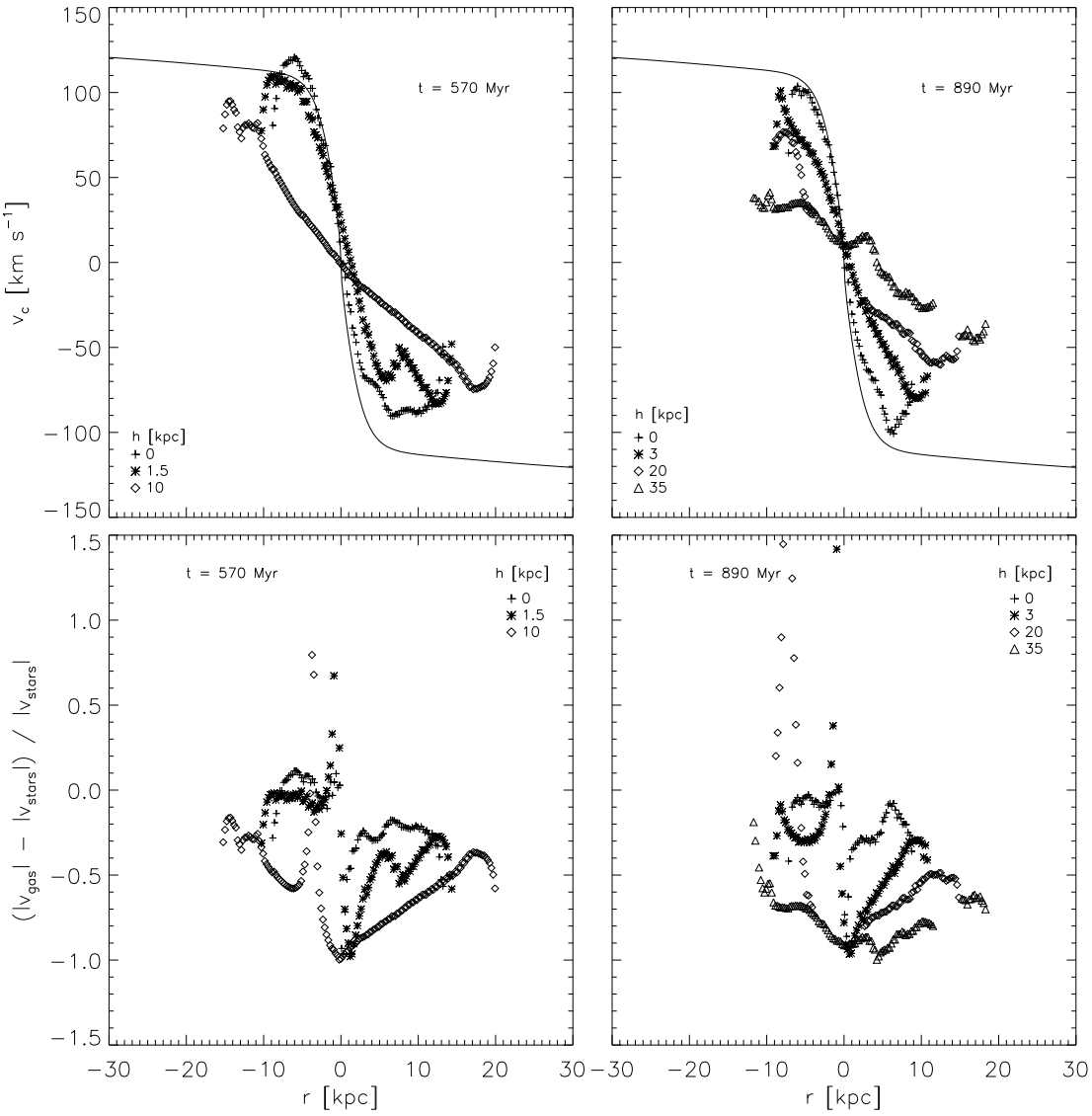

Figure 4.4: Same as fig. 4.3 for Mod2 simulation.

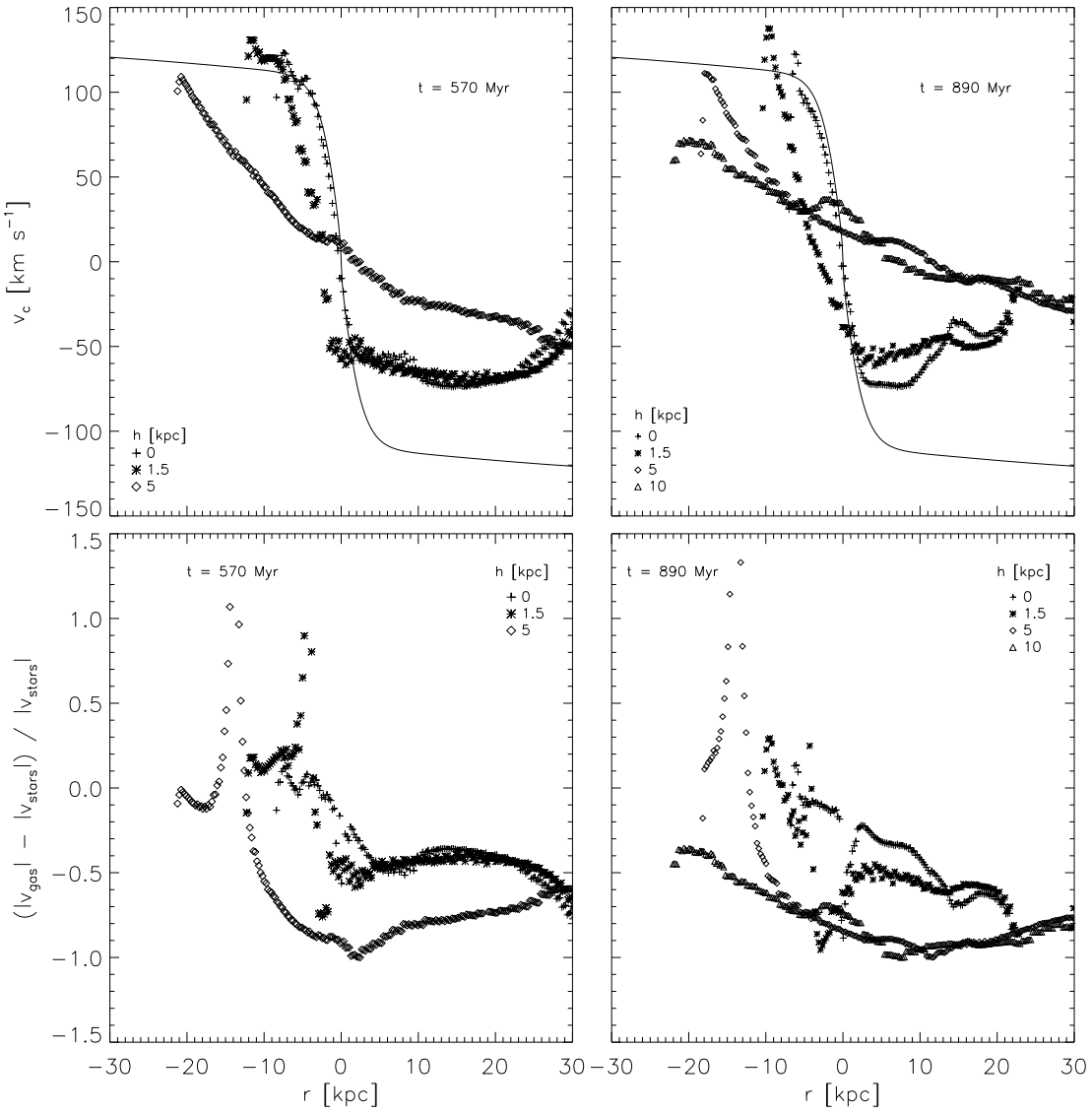

Figure 4.5: Same as fig. 4.3 for Mod3 simulation.

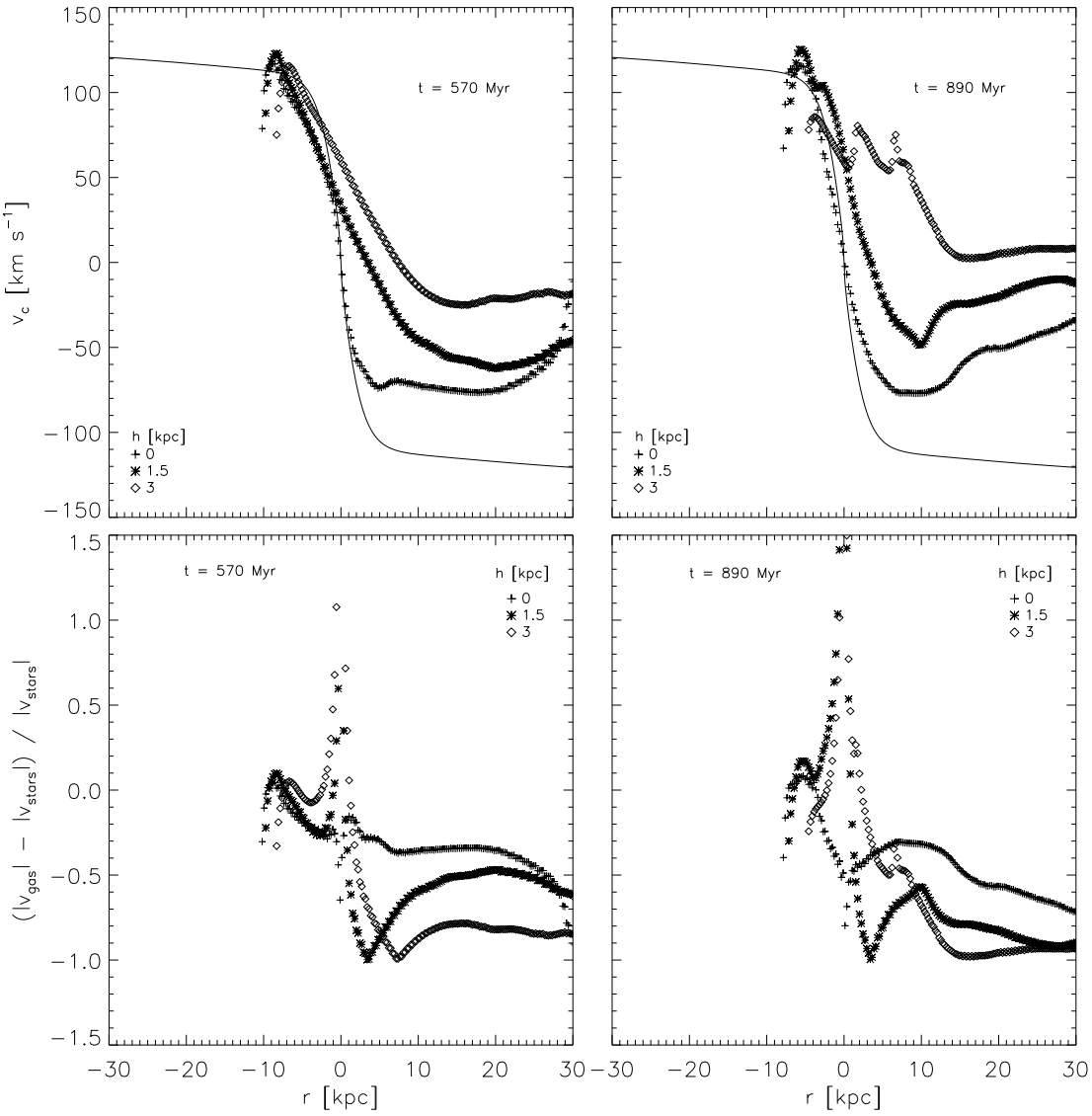

Figure 4.6: Same as fig. 4.3 for Mod4 simulation.

From this analysis, it is observed that despite the fact that the RPS is a process that affects directly the gaseous component in the galaxy, the gas in the tail still retain some rotation, which has been observed in the jellyfish galaxy JO201 through the Hα emission line (Bellhouse et al. 2017). Although in JO201 the gas outside the disc is still rotating with nearly the same velocity as the stars, in the models presented here, the velocity decreases with increasing distance from the disc as it is pushed off the galaxy and mixing with the non-rotating ICM wind.

4.2 Star formation

A preliminary analysis concerning the star formation in jellyfish galaxies is being performed. It has been observed that the star formation is ongoing while the ISM is being removed from the disc (Sun et al. 2010; Yagi et al. 2010, 2013; Poggianti et al. 2017b, 2019). There is also enhanced star formation in the disc (Vulcani et al. 2018) due to the compression of the ISM by the ICM. Since the simulations do not have enough resolution to model the star formation, we will use a sub-grid model to estimate it. From observations of jellyfish galaxies (see example in fig. 4.7), we can analyze the distribution of the Hα emission and determine a density threshold for the star formation and then estimate a probability for our simulations to form new stars in the filaments of the simulated tails, where we could expect the birth of new stars since these are the densest regions of the swept gas. In this way, we will explore how the tail structures in models with galactic magnetic field and the inclination of the disc affect the star formation. Given that the structures in the tails move up forward from the galaxy and we expect some star formation to occur in these regions, then it is possible to have different stellar populations along the tails (see Bellhouse et al. 2019).

4.3 Chemical enrichment of the ICM

In the RPS process, when the ISM is removed from a galaxy as it travels within the cluster, the ISM mixes with the ICM, and this latter is enriched with metallicities of $\sim 0.3 Z_{\odot}$ (for a review see Werner et al. 2008). In chapter 2 it was shown that magnetic fields can inhibit the mixing of gas from the galaxy with the ICM compared to pure HD models, so the enrichment of the ICM could be inhomogeneous. Additionally, in chapter 3 it has been studied how much the ICM can be magnetized through the tails depending on the inclination of the disc with respect to the wind, where models with face-on geometry contribute more to the magnetization of the surroundings. A similar dependency is expected for the enrichment

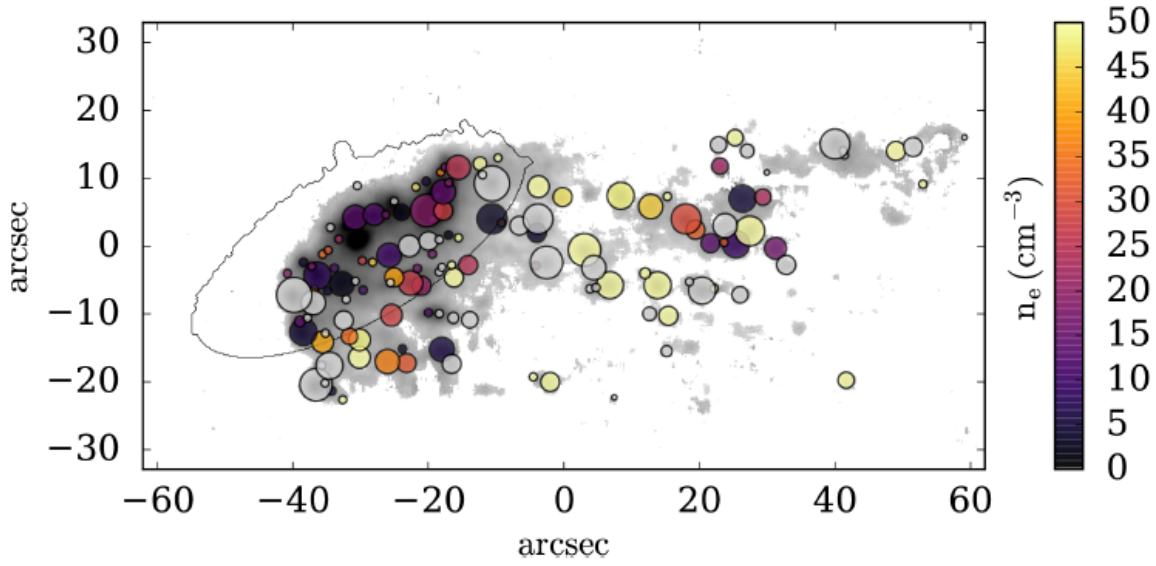

Figure 4.7: Gas density of star-forming clumps (circles) for the jellyfish galaxy JO206. The Hα map is in greyscale and the stellar is the black contour. (from Poggianti et al. 2019).

of the ICM from these simulations. The appropiate way to calculate abundances and metallicities of these models could be with the use of a passive scalar in the evolution of the simulations, so that we may differentiate the gas that used to be in disc from that of the wind. Due to current limitations of the numerical code, the passive scalar did not work properly. However, by measuring the mass loss for each model, it is possible to estimate how much mass is "injected" into the ICM, and therefore, estimate the enrichment rate of the ICM. Also, as it was mentioned in section 4.2, stars formed along the tail with different ages may have an impact in the tail metallicity, that later would be mixed with the ICM.

Chapter 5

Conclusions

In this thesis it has been studied the gas dynamics in simulations of ram pressure stripping on a disc galaxy leading to the formation of a jellyfish galaxy. 3D magnetohydrodynamic (MHD) models of a gaseous disc in hydrostatic equilibrium with galactic magnetic fields were performed, initially in rotational equilibrium with the gravitational potential. Additionally, simulations of pure hydrodynamic discs (no magnetic field) were carried out to study the effects of the magnetic field on the interaction of the ICM with the galactic disc.

The presence of the magnetic fields increases the thickness of the disc, increasing the gas surface density in the galaxy and producing a flared gaseous disc. In the MHD disc, when the ICM wind hits the galaxy, oblique shocks appear at the wind-disc interface and generate an inflow of gas from the outskirts of the galaxy towards the central regions, which lasts about $\sim 150\,\mathrm{Myr}$ in the model. This inward motion of gas could induce star formation or ignite nuclear activity by providing material before it is removed by the ICM wind. Recent studies of jellyfish galaxies have shown nuclear activity (Poggianti et al. 2016, 2017), where a high fraction of these objects present an AGN, so the ISM loses angular momentum when it is compressed by the ICM and thus moving towards the galactic centre. Other tests need to be performed to better study the funnelling of gas towards the central regions of the galaxy: different disc surface densities, flare strengths, and different wind profiles and angles of motion of the galaxy.

The magnetic field also alters the morphology of the stripped gas. In the MHD cases the displaced gas has a smoother distribution and denser gas survives farther away from the galaxy while in the HD the gas looks clumpier and mixes easier with the surroundings. For the HD case, when the wind hits the disc and starts to remove the gas, clump-like regions form leading to the development of eddies that, when pushed by the wind, leave a tail of gas giving the clumpy and filamentary

structure in the displaced gas. These differences are due to the effective equation of state of the models, since an isothermal gas is more compressible than an adiabatic or magnetized gas. The MHD disc loses its gas at a slower rate and the disc is less truncated than the HD because the MHD has a higher surface density. The truncation radius in these cases depends on the presence of the magnetic field, since both models have the same gravitational potential. Another HD model was tested with a surface density similar to the one for the MHD, resulting in a disc with a higher volumetric density at the galactic midplane. It was observed that the *heavy* HD model has a stripping rate and a truncation radius similar to the MHD case, i.e., a disc with a higher surface density is more difficult to remove its gas. However, the morphology of the stripped gas in the heavy model is similar to the HD one.

Additionally, the effects of varying the disc inclination with respect to the wind direction in MHD simulations of jellyfish galaxies were studied. Here four simulations were perfomed with disc inclinations of $0, 20, 70$, and 90^{o}. In models with inclinations of 0 and 20^{o}, which have a (nearly) face-on interaction with the wind, the gas is removed from the disc in ring-like structures dragging the MF as the wind accelerates and flows through the galaxy. More gas is removed and displaced farther away from the disc and the rings get distorted in the direction of the wind motion, forming filaments aligned with the MF. For the (nearly) edge-on models, with inclinations of 70 and 90^{o}, the gas and the MF are compressed in the leading side of the galaxy and elongated downstream. However, these models do not show a very extended tail but instead they develop a spiral-like structure in the disc similar to the results from Tosa (1994). Also, when these models are seen edge-on, the MF lines emerge outside of the galactic plane and then wrap around the disc in the downstream side shielding the galaxy. From these models, it was found that face-on interactions tend to magnetize more the ICM, with $B \approx 0.3$ to $0.7\mu G$ in the tails, than highly tilted discs, where $B \lesssim 0.2 - 0.3\mu G$ in the tails. In the remnant disc, the MF strength is enhanced a factor of $\sim 2 - 3$ compared to the initial condition, although in the edge-on models B is slightly higher in the upstream side.

Synthetic observations were generated for the synchrotron emission and polarization. It is observed that the synchrotron image is truncated in the galaxy and also shows a tail following the gas distribution similar to some galaxies in the Virgo Cluster undergoing RPS. In the polarization maps, information of the MF is recovered, since the B-vectors inferred from the polarization of the synchrotron emission accurately draw the MF structure.

Appendix A

RAMSES code

A.1 Numerical method

The simulations used in this thesis were developed with the adaptive mesh refinement (AMR) code RAMSES (Teyssier 2002). The AMR grid is built on a tree structure allowing recursive grid refinement, with new refinements created or destroyed according to user-defined criteria. RAMSES uses a second-order Godunov hydrodynamical solver, a method for shock capturing based on a Riemann solver without artifical viscosity. The time integration can be performed for each level independently using standard stability constraints, where each level evolves according to its own timestep. RAMSES solves the magnetohydrodynamic equations in their conservative form:

$$\frac{\partial \rho}{\partial t} + \nabla \cdot (\rho \mathbf{v}) = 0\,, \tag{A.1}$$

$$\frac{\partial (\rho \mathbf{v})}{\partial t} + \nabla \cdot (\rho \mathbf{v}\mathbf{v} - \mathbf{B}\mathbf{B}) + \nabla P_{\rm tot} = 0\,, \tag{A.2}$$

$$\frac{\partial E}{\partial t} + \nabla \cdot [(E + P_{\rm tot})\mathbf{v} - \mathbf{B}(\mathbf{B} \cdot \mathbf{v})] = 0\,, \tag{A.3}$$

$$\frac{\partial \mathbf{B}}{\partial t} + \nabla \cdot (\mathbf{v}\mathbf{B} - \mathbf{B}\mathbf{v}) = 0\,, \tag{A.4}$$

where ρ is the fluid density, $\mathbf{v}$ is the fluid velocity, $\mathbf{B}$ is the magnetic field, $P_{\rm tot}$ is the fluid total pressure

$$P_{\rm tot} = P_{\rm th} + \frac{\mathbf{B} \cdot \mathbf{B}}{8\pi}\,, \tag{A.5}$$

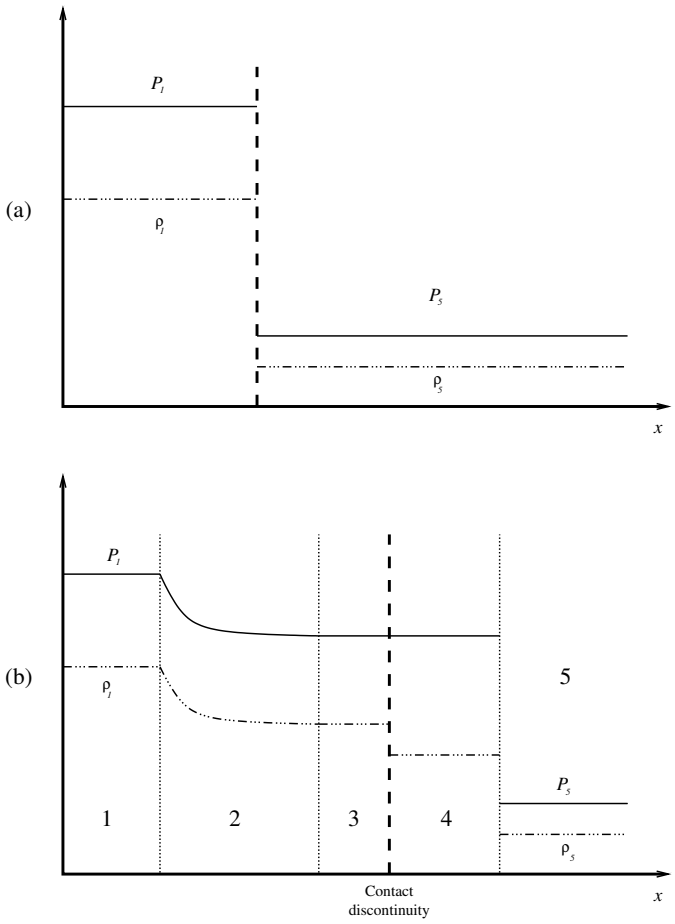

Figure A.1: Sketch of a shock tube. *Top*: Initial state of two regions filled with a fluid separated by a diaphragm (dashed vertical line). *Bottom*: Flow pattern of the two fluids once the diaphragm is removed

where $P_{\rm th}$ is the thermal pressure, E is the total energy of the fluid

$$E = \varepsilon + \rho\frac{\mathbf{v}\cdot\mathbf{v}}{2} + \frac{\mathbf{B}\cdot\mathbf{B}}{2}\,, \tag{A.6}$$

and ε is the internal energy density.

To illustrate how a Riemann solver works, consider a shock tube: two regions filled with a fluid initially at rest and separeted by a diaphragm (see fig. A.1, top panel). The fluid to left of the diaphragm has pressure P_1 and density ρ_1 and the fluid located at the right has $P_5 < P_1$ and $\rho_5 < \rho_1$. When the diaphragm is removed (fig. A.1, bottom panel), the fluid from the left moves to the right. Then,

the interaction of the two fluids generates five regions: two undisturbed (regions 1 and 5), one expanding (2), one decompressed (3), and one with compressed fluid (4). The solution of the Riemann problem consists in finding the functions $\rho(x,t)$, $P(x,t)$ and the velocity $v(x,t)$ that describe the flow in regions 2 to 4 knowing the values of regions 1 and 5. Methods that solve the Riemann problem are denominated Riemann solvers. In the RAMSES code, the Riemann problem is solved with the Godunov method at the face of each cell to determine the flow of material to the next cell. This Godunov solver captures discontinuities with a high level precision.

A.2 Initial conditions

A magnetized disc was set up in rotational equilibrium in a fixed gravitational potential. The models presented in Chapter 2 were performed in 3D with 11 refinement levels, for a resolution equivalent to $(2048)^3$ cells, while those in Chapter 3 have 9 levels of refinement. In both cases, a box of 120 kpc in each direction was used.

The gravitational potential used for the galaxy is based on the model of Allen & Santillán (1991), which is an analytic and simple potential that can reproduce the rotation curve of the Milky Way. This potential model can be easily modified to approximate the rotation curves of other galaxies. For this work, it was modeled a late type, low-luminosity spiral galaxy (similar to M33). The mass and scale parameters were modified to model a rotation curve of $v_{circ} = 110 - 120\,\mathrm{km\ s^{-1}}$ (Corbelli 2003, for M33). Nevertheless, for the simulations presented in this work, the galactic bulge component was removed of the potential since it generated a large density gradient in the z-direction (perpendicular to the galactic disc) for small radii that generated problems for the initial setup procedure (described below). Regardless, this should have little impact on the conclusions, specially since the M33 bulge's mass is small.

The initial conditions were established from a method similar to Gómez & Cox (2002). First, the radial density and velocity profiles are defined in the galactic mid-plane, assuming that the disc gas is isothermal and in rotational equilibrium with the gravitational force, the total pressure gradient, and the magnetic tension,

$$\frac{v_\phi^2(r,z)}{r} = \frac{\partial \Phi}{\partial r} + \frac{1}{\rho(r,z)}\left[\frac{\partial P_{\mathrm{tot}}}{\partial r} + \frac{2P_B(r,z)}{r}\right], \tag{A.7}$$

where the total pressure P_{tot} is the sum of the thermal ($P_{th} = c_s^2\rho(r,z)$, with $c_s \approx 8\,\mathrm{km\ s^{-1}}$) and the magnetic ($P_B$) pressures. The magnetic pressure has two components, $P_B = P_{B,inner} + P_{B,outer}$, with

$$P_{B,inner} = P_{B0}\left[1 - \mathrm{erf}\left(\frac{R}{r_b}\right)\right] \quad \text{and} \tag{A.8}$$

$$P_{B,outer} = \frac{P_{B0}\, n}{(n + n_c)}\,, \tag{A.9}$$

where $R = \sqrt{r^2 + z^2}$, $r_b = b_1/3$, $P_{B0} = 1.75 \times 10^{-13}\,\mathrm{dyn\,cm^{-2}}$ and $n_c = 0.04\,\mathrm{cm^{-3}}$. With these expressions for the total pressure and eq. (A.7), a given midplane density (or velocity) profile uniquely defines the velocity (density) profile. In the bulge, the rotation curve resembles a rigid body, and so we define the rotation velocity that increases linearly with radius,

$$v_\phi(r, 0) = v_\phi(b_1, 0)\left[\frac{r}{b_1}\right], \tag{A.10}$$

where $v_\phi(b_1, 0)$ is the circular velocity obtained from the gravitational potential in $r = b_1$ and $z = 0$. Then, the density profile in the midplane is given by,

$$\frac{\partial \rho}{\partial r} = \frac{\rho\left(v_\phi^2 - \partial\Phi/\partial r\right) + \left(P_{B0}/r_b\right) e^{-(R/r_b)^2}}{[c_s^2 + P_{B0}\rho_c/(\rho + \rho_c)^2]}\,, \tag{A.11}$$

which is integrated from $r = 0$ to b_1.

For $r > b_1$ we do the converse: a density profile is defined as exponentially decreasing at the mid-plane,

$$\rho(r, 0) = \rho_0 \exp[-(r - b_1)/h_r]\,,$$

where $h_r = 6\,\mathrm{kpc}$ and ρ_0 is the value found at $r = b_1$ from eq. (A.11). Once the mid-plane density is calculated, the distribution at $z \neq 0$ is found by assuming magnetohydrostatic equilibrium and an isothermal equation of state,

$$\frac{\partial P_{\mathrm{tot}}}{\partial z} = -\rho\,\frac{\partial \Phi}{\partial z}\,, \tag{A.12}$$

where again $P_{\mathrm{tot}} = P_{th} + P_B$. By substituting the magnetic pressure components (eqs. A.8 and A.9) and the equation of state it follows

$$\frac{\partial \rho}{\partial z} = \frac{-\rho\partial\Phi/\partial z + \left(P_{B0}/r_b\right)\exp\left[-(R/r_b)^2\right]}{[c_s^2 + P_{B0}\rho_c/(\rho + \rho_c)^2]}\,, \tag{A.13}$$

which is integrated along the z coordinate to obtain the vertical density profile at any radius r. The rotation velocity above the midplane is given by (Gómez & Cox 2002):

$$v_\phi^2(r,z) = v_\phi^2(r,0) - v_A^2(r,0) + v_A^2(r,z)\,, \tag{A.14}$$

where v_A is the Alfvén velocity ($v_A = \sqrt{2P_B/\rho}$).

Figure A.2 (*top*) shows the number density $n = \rho/(\mu m_{\rm H})$[1] for the initial condition of the MHD disc at $y = 0$, which results in the initial β parameter ($\beta = P_{\rm th}/(B^2/8\pi)$) shown in fig. A.2 (*bottom*). It can be seen that, for the magnetized case, the disc is thicker in the outskirts than in the central region, that is, the galactic disc flares in the presence of the MF. Additionally, the scale height of the MHD disc is larger than in HD one. When solving the equation of hydrostatic equilibrium, the MF changes the compressibility of the gas, thus increasing the surface density Σ for a given gravitational potential and midplane density, which results in a heavier disc compared to an HD model. For this reason, another HD simulation was performed with surface density similar to that of the magnetized disc model. This is called the heavy model (fig. A.2). To obtain the density distribution of the heavy disc, the equations (A.11) and (A.13) are solved by taking $\rho_{heavy}(z = 0) = 10\rho_{HD}(z = 0)$, where ρ_{HD} is the density of the HD model, thus resulting in $\Sigma_{heavy} \sim 1.5\Sigma_{MHD}$.

In the setup described above for the MHD model, the MF has two components (eqs. A.8 and A.9). While the outer component ($r > b_1$) is purely toroidal, the inner one is random. For the inner random component ($r < b_1$), the vector potential $\mathbf{A}$ is defined as

$$A_x = A_0 \cos\phi_r \, \sin\theta_r \, f(z) \tag{A.15}$$
$$A_y = A_0 \sin\phi_r \, \sin\theta_r \, f(z) \tag{A.16}$$
$$A_z = A_0 \cos\theta_r \, f(z)\,, \tag{A.17}$$

where the angles ϕ_r and θ_r where obtained randomly at each cell within the range $[-\pi/2, \pi/2]$ and $[0, 2\pi]$, respectively. A_0 is drawn from a normal distribution with dispersion equal to $\sqrt{8\pi P_{B0}}$.

The function $f(z) = \mathrm{sech}^2(z/z_h)$, with $z_h = 150\,\mathrm{pc}$, modulates the vector potential so its magnitude has the same scale height as the density in the bulge. Once the components for the vector potential are calculated, it is smoothed at each cell,

[1] $\mu = 1.27$ is the mean particle mass and $m_{\rm H} = 1.67 \times 10^{-24}\,\mathrm{g}$ is the hydrogen mass

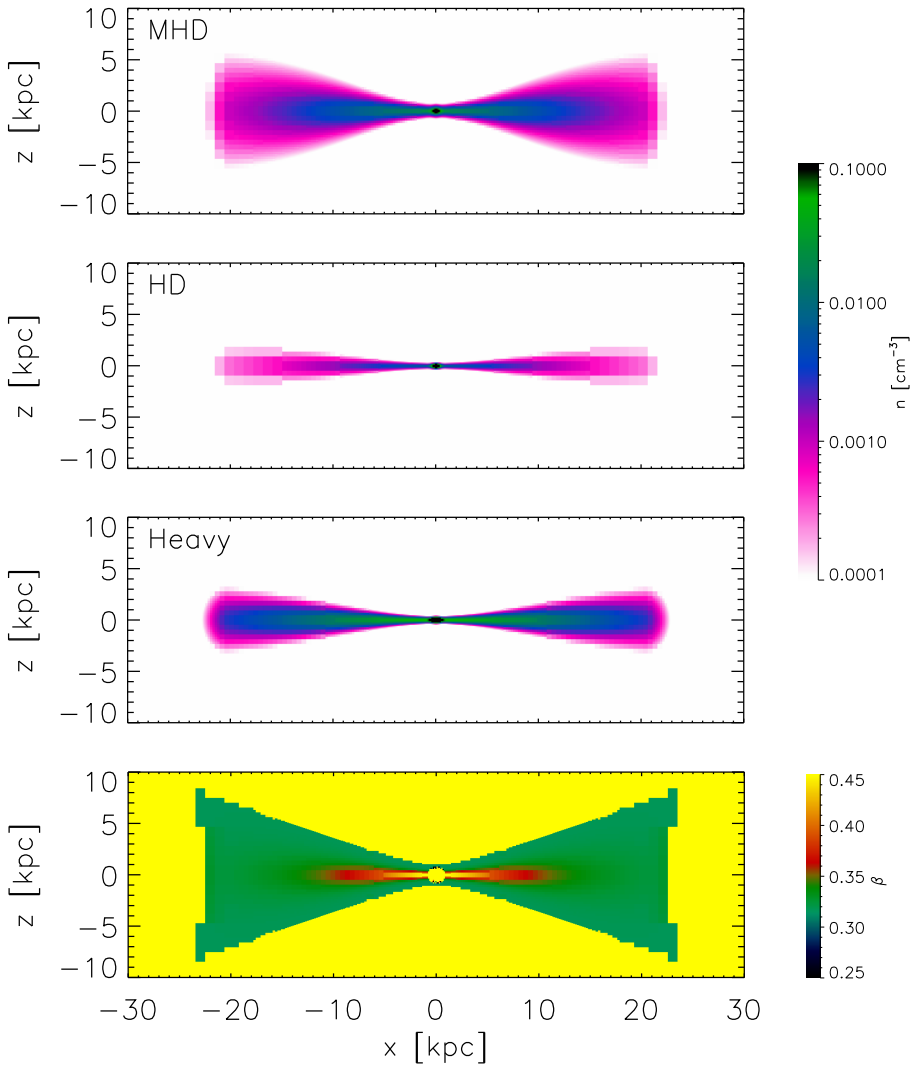

Figure A.2: From top to bottom: density slices of the initial condition for the MHD (*first row*), HD (*second row*), and heavy (*third row*) models. Initial $\beta = P_{\rm th}/(B^2/8\pi)$ parameter (*bottom*). All images are slices at the $y = 0$ plane.

$$A_{xs} = \sum_{ijk}(A_{x,ijk}\, w_{ijk}) / \sum_{ijk} w_{ijk}\,, \tag{A.18}$$

$$A_{ys} = \sum_{ijk}(A_{y,ijk}\, w_{ijk}) / \sum_{ijk} w_{ijk}\,, \tag{A.19}$$

$$A_{zs} = \sum_{ijk}(A_{z,ijk}\, w_{ijk}) / \sum_{ijk} w_{ijk}\,, \tag{A.20}$$

where $w_{ijk} = \exp -[r_{ijk}/(2\sigma^2)]$ is a weighted average, $r_{ijk} = (i^2 + j^2 + k^2)dx^2$, $\sigma = N_p dx/2$, N_p is the number of neighboring cells with which the average, calculated in each direction i, j and k, and dx is the displacement between cells. Finally, the MF is calculated $\mathbf{B}_{inner} = \nabla \times \mathbf{A}$. For the rest of the disc ($r > b_1$), the MF in the setup follows a toroidal configuration, with its strength given by the gas density (eq. A.9).

A.3 Boundary conditions

The RAMSES code uses "ghost regions" outside of the computational box to set up the boundary conditions. There are four types of boundary conditions used in RAMSES: periodic, where the fluid that goes out of the grid on one side is returned on the opposite side with the same physical values; reflexive, where the fluid from cells located in a ghost region x_{I+1} and x_{I+2} has the same properties as the fluid in the last cells from the active region x_I and x_{I-1}, respectively, that is $\rho(x_{I+1}) = \rho(x_I)$ and $\rho(x_{I+2}) = \rho(x_{I-1})$; outflow, where the properties of the cells in the ghost region have the same as the cells in the active region $\rho(x_{I+1}) = \rho(x_I)$; and inflow, where the fluid properties are user-defined and may vary in time.

In the present models, since the ICM-wind flows in the $+z$-direction, it was implemented an inflow boundary condition such that the flow enters from a ghost region at the bottom of the computational box. For a box of size $b = 120\,\mathrm{kpc}$ in each direction, the wind is contained in a cylinder of radius $r < r_{\mathrm{boundary}}$, where $r_{\mathrm{boundary}} = b/2 - b/2^{l_{\mathrm{min}}}$ and l_{min} is the minimum level of refinement. At $r < r_{\mathrm{boundary}}$, the wind velocity profile is $v_{\mathrm{wind}} = (v_f - v_i)t/t_f + v_i$ with $v_f = 1000\,\mathrm{km\ s^{-1}}$, $v_i = 300\,\mathrm{km\ s^{-1}}$, and $t_f = 700\,\mathrm{Myr}$, while outside r_{boundary} the wind velocity is v_f. Density and magnetic field are $n = 10^{-5}\,\mathrm{cm^{-3}}$ and $B = 0$ in both regions. Outflow conditions were used for the rest of the boundaries.

Bibliography

Abadi, M. G., Moore, B. & Bower, R. G. 1999, MNRAS, 308, 947

Abell, G. O. 1958, ApJS, 3, 211

Abell, G. O., Corwin, H. G., Jr., & Olowin, R. P. 1989, ApJS, 70, 1

Abramson, A. & Kenney, J. D. P. 2014, AJ, 147, 63

Abramson, A., Kenney, J. D. P., Crowl, H. H., Chung, A., van Gorkom, J. H., Vollmer, B. & Schiminovich, D. 2011, AJ, 141, 164

Abramson, A., Kenney, J., Crowl, H., & Tal, T. 2016, AJ, 152, 32

Adebahr, B., Krause, M., Klein, U., Weżgowiec, M., Bomans, D. J. & Dettmar, R. J. 2013, A&A, 555A, 23A

Aguerri, J., Balcells, M. & Peletier, R. 2001, A&A, 367, 428

Aguerri, J. A. L., Debattista, V. P., & Corsini, E. M. 2003, MNRAS, 338, 465

Aguerri, J. A. L., Elias-Rosa, N., Corsini, E. M., & Muñoz-Tuñón, C. 2005, A&A, 434, 109

Aguerri, J., Agulli, I., Diaferio, A. & Dalla Vecchia, C. 2017, MNRAS, 468, 364

Allen, C. & Santillán, A. 1991, Rev. Mex. Astron. Astrofis., 22, 255

Andersen, V., & Owen, F. N. 1995, AJ, 109, 1582

Andredakis, Y. C., & Sanders, R. H. 1994, MNRAS, 267, 283

Andredakis, Y. C., Peletier, R. F., & Balcells, M. 1995, MNRAS, 275, 874

Aragón-Salamanca, A., Bedregal, A. G., & Merrifield, M. R. 2006, A&A, 458, 101

Balcells, M., Graham, A. W. & Peletier, R. F. 2007, ApJ, 665, 1104

Barr, J. M., Bedregal, A. G., Aragón-Salamanca, A., Merrifield, M. R., & Bamford, S. P. 2007, A&A, 470, 173

Beck, R. in *The magnetized plasma in galaxy evolution* 2005, ed. K. T. Chyży, K. Otmianowska-Mazur, M. Soida & R.-J. Dettmar, 193

Beck, R. in *Cosmic Magnetic Fields* 2005, ed. R. Wielebinski, & R. Beck. (Berlin: Springer), Lect. Notes Phys., 664, 41

Beck, R., Fletcher, A., Shukurov, A., Snodin, A., Sokoloff, D. D., Ehle, M., Moss, D. & Shoutenkov, V. 2005, A&A, 444, 739B

Beck, R. & Wielebinski, R. in *Planets, Stars and Stellar Systems* 2013, Vol. 5, ed. G. Gilmore, Springer-Verlag, Berlin, p. 641

Bedregal, A. G., Aragón-Salamanca, A., & Merrifield, M. R. 2006, MNRAS, 373, 1125

Bedregal, A. G. 2012, A&AT, 27, 177

Bekki, K., Couch, W. J. & Shioya, Y. 2002, ApJ, 577, 651

Bekki, K. & Couch, W. J. 2003, ApJ, 596, L13
Bekki, K. 2014, MNRAS, 438, 444
Bellhouse, C., Jaffé, Y. L., Hau, G. K. T., et al. 2017, ApJ, 844, 49
Bellhouse, C., Jaffé, Y. L., McGee, S. L., et al. 2019, MNRAS, 485, 1157
Biviano, A. & Katgert, P. 2004, A&A, 424, 779
Bonafede, A., Feretti, L., Murgia, M., et al. 2010, A&A, 513, A30
Bonafede, A., Govoni, F., Feretti, L., et al. 2011, A&A, 530, A24
Bonafede, A., Vazza, F., Brüggen, M., et al. 2013, MNRAS, 433, 3208
Borlaff, A., Eliche-Moral, M. C., Rodríguez-Pérez, C., Querejeta, M., Tapia, T., Pérez-González, P. G., Zamorano, J., Gallego, J. & Beckman, J. 2014, A&A, 570, 103
Boselli, A. 1994, A&A, 292, 1
Boselli, A., Casoli, F., & Lequeux, J. 1995, A&AS, 110, 521
Boselli, A., Gavazzi, G., Lequeux, J., et al. 1997, A&A, 327, 522
Boselli, A., Lequeux, J., & Gavazzi, G. 2002, A&A, 384, 33
Boselli, A., Boissier, S., Cortese, L., et al. 2006, ApJ, 651, 811
Boselli, A. & Gavazzi, G. 2006, PASP, 118, 517
Boselli, A., Cortese, L., Boquien, M., Boissier, S., Catinella, B., Gavazzi, G., Lagos, C. & Saintonge, A. 2014, A&A, 564, A67
Budzynski, J. M., Koposov, S. E., McCarthy, I. G., & Belokurov, V. 2014, MNRAS, 437, 1362
Burstein, D. 1979, ApJ, 234, 435
Burstein, D. 1979, ApJ, 234, 829
Buta, R. J., Sheth, K., Regan, M., et al. 2010, ApJS, 190, 147
Butcher, H. & Oemler, Jr., A. 1978, ApJ, 219, 18
Byrd, G., & Valtonen, M. 1990, ApJ, 350, 89
Capaccioli, M., in *The World of Galaxies* 1989, eds. Corwin, H. G. & Bottinelli, L., (Le Monde des Galaxies), New York, Springer-Verlag, p. 208
Carilli, C. L., & Taylor, G. B. 2002, ARA&A, 40, 319
Carollo, C. M., Scarlata, C., Stiavelli, M., Wyse, R. F. G., & Mayer, L. 2007, ApJ, 658, 960
Casoli, F., Boisse, P., Combes, F., & Dupraz, C. 1991, A&A, 249, 359
Cayatte, V., van Gorkom, J. H., Balkowski, C. & Kotanyi, C. 1990, AJ, 100, 604
Cayatte, V., Kotanyi, C., Balkowski, C., & van Gorkom, J. H. 1994, AJ, 107, 1003
Cen, R., & Ostriker, J. P. 2006, ApJ, 650, 560
Chiu, I., Mohr, J. J., McDonald, M., et al. 2018, MNRAS, 478, 3072
Chung, E. J., Rhee, M.-H., Kim, H., Yun, M. S., Heyer, M. & Young, J. S. 2009, ApJS, 184, 199
Chung, A., van Gorkom, J. H., Kenney, J. D. P., Crowl, H. & Vollmer, B. 2009, AJ, 138, 1741
Chyży, K. T. & Beck, R. 2004, A&A, 417, 541C
Chyży, K. T., Soida, M., Bomans, D. J., et al. 2006, A&A, 447, 465
Chyży, K. T., Ehle, M., & Beck, R. 2007, A&A, 474, 415
Clarke, T. E., Kronberg, P. P., & Böhringer, H. 2001, ApJ, 547, L111
Condon, J. J., Condon, M. A., Gisler, G., & Puschell, J. J. 1982, ApJ, 252, 102

Corbelli, E. 2003, MNRAS, 342, 199
Cortese, L., Marcillac, D., Richard, J., Bravo-Alfaro, H., Kneib, J.-P., Rieke, G., Covone, G., Egami, E., Rigby, J., Czoske, O. & Davies, J. 2007, MNRAS, 376, 157
Courteau, S., de Jong, R. S., & Broeils, A. H. 1996, ApJ, 457, L73
Cowie, L. L. & Songaila, A. 1977, Nature, 266, 501
Davies, R. D., & Lewis, B. M. 1973, MNRAS, 165, 231
de Jong, R. S. 1996, A&A, 313, 45
de Vaucouleurs, G. 1948, Annales d'Astrophysique, 11, 247
de Vaucouleurs, G. 1953, MNRAS, 113, 134
de Vaucouleurs, G. 1959, Handbuch der Physik, 53, 275
Dressler, A. 1980, ApJ, 236, 351
Dressler, A. 1986, ApJ, 301, 35
Dressler, A., Oemler, A., Smail, I., Barger, A., Butcher, H., Poggianti, B. M. & Sharples, R. M. 1997, ApJ, 490, 577
Duval, M. F., & Athanassoula, E. 1983, A&A, 121, 297
Ellison, S. L., Simard, L., Cowan, N. B., et al. 2009, MNRAS, 396, 1257
Elmegreen, B. G., & Elmegreen, D. M. 1985, ApJ, 288, 438
Elmegreen, D. M., Elmegreen, B. G.,Frogel, J. A., Eskridge, P. B., Pogge, R. W., Gallagher, A. & Iams, J. 2002, AJ, 124, 777
Erwin, P., Beckman, J. E., & Pohlen, M. 2005, ApJ, 626, L81
Farouki, R. & Shapiro, S. L. 1980, ApJ, 241, 928
Fasano, G., Poggianti, B. M., Couch, W. J., Bettoni, D, Kjærgaard, P. & Moles, M. 2000, ApJ, 542, 673F
Fendt, C., Beck, R., & Neininger, N. 1998, A&A, 335, 123
Feretti, L., Dallacasa, D., Govoni, F., et al. 1999, A&A, 344, 472
Ferrière, K. 1998, ApJ, 497, 759
Fletcher, A. 2010, ASPC, 438, 197F
Fletcher, A., Beck, R., Shukurov, A., Berkhuijsen, E. M., Horellou, C. 2011, MNRAS, 412, 2396
Fosalba, P., Lazarian, A., Prunet, S., & Tauber, J. A. 2002, ApJ, 564, 762
Fossati, M., Fumagalli, M., Boselli, A., Gavazzi, G., Sun, M. & Wilman, D. J. 2016, MNRAS, 455, 2028
Freeman, K. C. 1966, MNRAS, 133, 47
Freeman, K. C. 1970, ApJ, 160, 811
Frick, P, Stepanov, R, Beck, R, Sokoloff, D., Shukurov, A., Ehle, M. & Lundgren, A. 2016, A&A, 585, A21
Fuchs, B. & von Linden, S. 1998, MNRAS, 294, 513
Fumagalli, M., Fossati, M., Hau, G. K. T., Gavazzi, G., Bower, R., Sun, M. & Boselli, A. 2014, MNRAS, 445, 4335
Gallagher, J. S., Faber, S. M. & Balick, B. 1975, ApJ, 202, 7G
Gavazzi, G. 1989, ApJ, 346, 59
Gavazzi, G., & Boselli, A. 1999, A&A, 343, 93
Gavazzi, G., & Jaffe, W. 1986, ApJ, 310, 53
Gießübel, R. 2012, PhD Thesis, University of Cologne

Giovannini, G., Feretti, L., Venturi, T., Kim, K.-T., & Kronberg, P. P. 1993, ApJ, 406, 399
Giraud, E. 1986, A&A, 167, 25
Gómez, G. C. & Cox, D. 2002, ApJ, 580, 235
Gómez, P. L., Nichol, R. C., Miller, C. J., et al. 2003, ApJ, 584, 210
Govoni, F., & Feretti, L. 2004, International Journal of Modern Physics D, 13, 1549
Govoni, F., Dolag, K., Murgia, M., et al. 2010, A&A, 522, A105
Graham, A. W. in *Planets, Stars and Stellar Systems. Volume 6: Extragalactic Astronomy and Cosmology* 2013, eds Oswalt T. D., Keel W. C., Springer Science+Business Media. Dordrecht, p. 91
Graham, A. W., & de Blok, W. J. G. 2001, ApJ, 556, 177
Graham, A. W., & Prieto, M. 1999, Ap&SS, 269, 653
Graham, A. W., & Worley, C. C. 2008, MNRAS, 388, 1708
Greaves, J. S., Holland, W. S., Jenness, T., & Hawarden, T. G. 2000, Nature, 404, 732
Gunn, J. E. & Gott, J. R. I. 1972, ApJ, 176, 1
Haehnelt, M. G. & Rees, M. J. 1993, MNRAS, 263, 168H
Haynes, M. P. in *The Large-Scale Characteristics of the Galaxy* 1979, ed. W. B. Burton, (Dordrecht: Reidel) p. 567
Haynes, M. P., Giovanelli, R., & Chincarini, G. L. 1984, ARA&A, 22, 445
Hester, J. A., Seibert, M., Neill, J. D., Wyder, T K., Gil de Paz, A., Madore, B. F., Martin, D. C., Schiminovich, D. & Rich, R. M. 2010, ApJ, 716L, 14
Hinz, J. L., Rix, H.-W., & Bernstein, G. M. 2001, AJ, 121, 683
Hinz, J. L., Rieke, G. H., & Caldwell, N. 2003, AJ, 126, 2622
Hubble, E. P. 1926, ApJ, 64, 321
Hubble, E. P. 1930, ApJ, 71, 231
Hubble, E. P. 1936, Realm of the Nebulae, by E.P. Hubble. New Haven: Yale University Press, 1936.
Hummel, E., van der Hulst, J. M., Kennicutt, R. C., & Keel, W. C. 1990, A&A, 236, 333
Hunt, L. K., Pierini, D., & Giovanardi, C. 2004, A&A, 414, 905
Icke, V. 1985, A&A, 144, 115
Iono, D., Yun, M. S., & Mihos, J. C. 2004, ApJ, 616, 199
Jáchym, P., Combes, F., Cortese, L., Sun, M. & Kenney, J. D. P. 2014, ApJ, 792, 11
Jáchym, P., Köpen, J., Palouš, J. & Combes, F. 2009, A&A, 500, 693
Johnston E. J., Aragon-Salamanca A., Merrifield M. R. & Bedregal A. G. 2012, MNRAS, 422, 2590
Johnston E. J., Aragon-Salamanca A. & Merrifield M. R. 2014, MNRAS, 441, 333
Jones, T. J. 2000, AJ, 120, 2920
Kapferer, W., Kronberger, T., Ferrari, C., Riser, T. & Schindler, S. 2008, MNRAS, 389, 1405
Karachentseva, V. E., Karachentsev, I. D., & Melnyk, O. V. 2011, Astrophysical Bulletin, 66, 389
Katkov, I. Y., Kniazev, A. Y. & Sil'chenko, O. K. 2015, AJ, 150, 24
Keel, W. C., Kennicutt, R. C., Jr., Hummel, E., & van der Hulst, J. M. 1985, AJ, 90, 708
Kenney, J. D., & Young, J. S. 1988, ApJS, 66, 261

Kenney, J. D. P. & Koopmann, R. A. 1999, AJ, 117, 181
Kenney, J. D. P., van Gorkom, J. & Vollmer, B. 2004, AJ, 127, 3361
Kenney, J. D. P., Geha, M., Jáchym, P., Crowl, H. H., Dague, W., Chung, A., van Gorkom, J. & Vollmer, B. 2014, ApJ, 780, 119
Kennicut, R. C. 1983a, ApJ, 272, 54
Kennicutt, R. C., Jr. 1983b, AJ, 88, 483
Kennicutt, R. C., Jr., Keel, W. C., van der Hulst, J. M., Hummel, E., & Roettiger, K. A. 1987, AJ, 93, 1011
Kim, K.-T., Kronberg, P. P., Dewdney, P. E., & Landecker, T. L. 1990, ApJ, 355, 29
Kim, K.-T., Tribble, P. C., & Kronberg, P. P. 1991, ApJ, 379, 80
King, I. 1962, AJ, 67, 471
Klein, U., Weiland, H. & Brinks, E. 1991, A&A, 246, 323K
Koopmann, R. A., & Kenney, J. D. P. 1998, ApJ, 497, L75
Koopmann, R. A., & Kenney, J. D. P. 2004a, ApJ, 613, 866
Koopmann, R. A., & Kenney, J. D. P. 2004b, ApJ, 613, 851
Koopmann, R. A., Haynes, M. P., & Catinella, B. 2006, AJ, 131, 716
Kormendy, J. 1979, ApJ, 227, 714
Kormendy, J. 1982, ApJ, 257, 75
Kormendy, J., in *Secular Evolution of Galaxies*, 2013, eds., Falcon-Barroso J., Knapen J. H., XXIII Canary Islands Winter School of Astrophysics, Cambridge Univ. Press, Cambridge, p. 1
Kormendy, & Bender 2009, ApJL, 464, L119
Kormendy, J., & Kennicutt, R. C., Jr. 2004, ARA&A, 42, 603
Kronberg, P. P. in *Cosmic Magnetic Fields*, 2005, eds., Wielebinski, R. & Beck, R., Vol. 664, Berlin: Springer, p. 9
Kronberger, T., Kapferer, W., Ferrari, C., Unterguggenberger, S. & Schindler, S. 2008, A&A, 481, 337
Lacey, C. & Cole, S. 1993, MNRAS, 262, 627
Larson, R. B., Tinsley, B. M. & Caldwell, C. N. 1980, ApJ, 237, 692
Laurikainen, E., Salo, H., & Buta, R. 2005, MNRAS, 362, 1319
Laurikainen, E., Salo, H., Buta, R., et al. 2006, AJ, 132, 2634
Laurikainen, E., Salo, H., Buta, R. & Knapen, J. H. 2007, MNRAS, 381, 401
Laurikainen, E., Salo, H., Buta, R., & Knapen, J. H. 2009, ApJ, 692, L34
Laurikainen, E., Salo, H., Buta, R., Knapen, J. H. & Comerón, S. 2010, MNRAS, 405, 1089
Lewis, I., Balogh, M., De Propris, R., et al. 2002, MNRAS, 334, 673
Mathieu, A., Merrifield, M. R., & Kuijken, K. 2002, MNRAS, 330, 251
Méndez-Abreu, J., Aguerri, J. A. L., Corsini, E. M., & Simonneau, E. 2008, A&A, 478, 353
Méndez-Abreu, J., Simonneau, E., Aguerri, J. A. L., & Corsini, E. M. 2010, A&A, 521, A71
Merritt, D. 1984, ApJ, 276, 26
Mihos, J. C., Richstone, D. O., & Bothun, G. D. 1992, ApJ, 400, 153
Miley, G. 1980, ARA&A, 18, 165

Miller, R. H. 1986, A&A, 167, 41
Mohr, J. J., Mathiesen, B., & Evrard, A. E. 1999, ApJ, 517, 627
Moore, B., Katz, N., Lake, G., Dressler, A. & Oemler, A. 1996, Nat, 379, 613
Moore, B., Lake, G. & Katz, N. 1998, ApJ, 495, 139
Mouhcine, M., Baldry, I. K., & Bamford, S. P. 2007, MNRAS, 382, 801
Murgia, M., Govoni, F., Feretti, L., et al. 2004, A&A, 424, 429
Murphy, E. J., Kenney, J. D. P., Helou, G., Chung, A., & Howell, J. H. 2009, ApJ, 694, 1435
Neistein, E., Maoz, D., Rix, H.-W., & Tonry, J. L. 1999, AJ, 117, 2666
Nichol, R. C. 2004, Clusters of Galaxies: Probes of Cosmological Structure and Galaxy Evolution, 24
Niklas, S. 1995, PhD Thesis, University of Bonn
Noordermeer, E., & van der Hulst, J. M. 2007, MNRAS, 376, 1480
Noordermeer, E., Merrifield, M. R., Coccato, L., et al. 2008, MNRAS, 384, 943
Oemler, A. 1974, ApJ, 194, 10
Oemler, A., Jr. 1976, ApJ, 209, 693
Oort, J. H. 1970, A&A, 7, 381
Otmianowska-Mazur, K. & Vollmer, B. 2003, A&A, 402, 879
Pfrommer, C. & Dursi, J. 2010, Nature Physics, 6, 520
Pilyugin, L. S., Grebel, E. K., Zinchenko, I. A., Nefedyev, Y. A., & Mattsson, L. 2017, MNRAS, 465, 1358
Poggianti, B. M., Fasano, G., Omizzolo, A., Gullieuszik, M., Bettoni, D., Moretti, A., Paccagnella, A., Jaffé Y. L., Vulcani, B., Fritz, J, Couch W. & D'Onofrio, M. 2016, AJ, 151, 78P
Poggianti, B. M., Jaffé, Y. L., Moretti, A., Gullieuszik, M., Radovich, M., and Tonnesen, S., Fritz, J., Bettoni, D., Vulcani, B., Fasano, G., Bellhouse, C., Hau, G. & Omizzolo, A. 2017, Nat, 548, 304P
Poggianti, B. M., Moretti, A., Gullieuszik, M., et al. 2017, ApJ, 844, 48
Poggianti, B. M., Gullieuszik, M., Tonnesen, S., et al. 2019, MNRAS, 482, 4466
Pohlen, M., & Trujillo, I. 2006, A&A, 454, 759
Postman, M. & Geller, M. J. 1984, ApJ, 281, 95P
Prieto, M., Gottesman, S. T., Aguerri, J.-A. L., & Varela, A.-M. 1997, AJ, 114, 1413
Prieto, M., Aguerri, J. A. L., Varela, A. M., & Muñoz-Tuñón, C. 2001, A&A, 367, 405
Prochaska Chamberlain, L. C., Courteau, S., McDonald, M & Rose, J. A. 2011, MNRAS, 412, 423P
Puzia, T. H., Kissler-Patig, M., Brodie, J. P., & Schroder, L. L. 2000, AJ, 120, 777
Quilis, V., Moore, B. & Bower, R. 2000, Science, 288, 1617
Ramos-Martínez, M., Gómez, G. C. & Pérez-Villegas, A. 2018, MNRAS, 476, 3781
Rengarajan, T. N., Karnik, A. D. & Iyengar, K. V. K. 1997, MNRAS, 290, 1
Reynolds, J. H. 1913, MNRAS, 74, 132
Roediger, E. 2009, AN, 330, 888
Roediger, E. & Brüggen, M. 2006, MNRAS, 369, 567
Roediger, E. & Brüggen, M. 2007, MNRAS, 380, 1399
Roediger, E. & Brüggen, M. 2008, MNRAS, 388, 465

Roediger, E., Brüggen, M. & Hoeft, M. 2006, MNRAS, 371, 609
Roediger, E. & Hensler, G. 2005, A&A, 433, 875
Rood, H. J., Page, T. L., Kintner, E. C., & King, I. R. 1972, ApJ, 175, 627
Rudnick, L., & Blundell, K. M. 2003, ApJ, 588, 143
Ruszkowski, M., Brüggen, M., Lee, D. & Shin, M. S. 2014, ApJ, 784, 75
Ryu, D., Schleicher, D. R. G., Treumann, R. A., Tsagas, C. G., & Widrow, L. M. 2012, Space Sci. Rev., 166, 1
Sancisi, R., Fraternali, F., Oosterloo, T. & van der Hult, T. 2008, A&A Rev., 15, 189
Sandage, A., in *Galaxies and the Universe*, 1975, ed. A. Sandage, M. Sandage & G. A. Tammann (Chicago: Univ. Chicago Press) 1
Sandage, A., & Bedke, J. 1994, The Carnegie Atlas of Galaxies. Volumes I, II.
Sandage A., Tammann G. A., 1981, Revised Shapley-Ames Catalog of Bright Galaxies. Carnegie Institution, Washington
Scarrott, S. M., Ward-Thompson, D., & Warren-Smith, R. F. 1987, MNRAS, 224, 299
Schechter, P. 1976, ApJ, 203, 297

Schulz, S. & Struck, C. 2001, MNRAS, 328, 185
Scodeggio, M. & Gavazzi, G. 1993, ApJ, 409, 110
Sellwood, J. A. & Carlberg, R. G. 1984, ApJ, 282, 61
Sérsic, J. L. 1968, Córdoba, Argentina: Observatorio Astronómico.
Shields, G. A., Skillman, E. D., & Kennicutt, R. C., Jr. 1991, ApJ, 371, 82
Sil'Chenko, O. 2006, ApJ, 641, 229
Sil'chenko, O., Proshina, I. S., Shulga, A. P. & Koposov, S. E. 2012, MNRAS, 427, 790
Simien, F. & de Vaucouleurs, G. 1986, ApJ, 302, 564S
Sivanandam, S., Rieke, M. J. & Rieke, G. H. 2010, ApJ, 717, 147
Skillman, E. D., Kennicutt, R. C., Jr., Shields, G. A., & Zaritsky, D. 1996, ApJ, 462, 147
Smith, R. J., Lucey, J. R., Hammer, D., et al. 2010, MNRAS, 408, 1417.
Smith, R., Davies, J. I. & Nelson, A. H. 2010, MNRAS, 405, 1723
Smith, R., Sánchez-Janssen, R., Fellhauer, M., Puzia, T. H., Aguerri, J. A. L. & Farias, J. P. 2013, MNRAS, 429, 1066
Soida, M., Otmianowska-Mazur, K., Chyży, K. & Vollmer, B. 2006, A&A, 458, 727
Solanes, J. M., Manrique, A., García-Gómez, C., et al. 2001, ApJ, 548, 97
Spitzer, L., & Baade, W. 1951, ApJ, 113, 413
Stark, A. A., Knapp, G. R., Bally, J., et al. 1986, ApJ, 310, 660
Stein, Y., Bomans, D. J., Ferguson, A. M. N. & Dettmar, R.-J. 2017, A&A, 605, A5
Steinhauser, D., Haider, M., Kapferer, W. & Schindler, S. 2012, A&A, 544, A54
Sun, M., Donahue, M., Roediger, E., Nulsen, P. E. J., Voit, G. M., Sarazin, C., Forman, W. & Jones, C. 2010, ApJ, 708, 946
Sun, M., Donahue, M. & Voit, G. M. 2007, ApJ, 671, 190
Sun, M., Jones, C. & Forman, W. 2006, ApJ, 637, L81
Tabatabaei, F. S., Krause, M., Fletcher, A. & Beck, R. 2008, A&A, 490, 1005
Tanaka, M., Goto, T., Okamura, S., Shimasaku, K., & Brinkmann, J. 2004, AJ, 128, 2677
Tapia, T. et al. 2014, A&A, 565, 31
Tapia, T., Eliche-Moral, M. C., Aceves, H., et al. 2017, A&A, 604, A105

Taylor, G. B., & Perley, R. A. 1993, ApJ, 416, 554
Taylor, G. B., Barton, E. J., & Ge, J. 1994, AJ, 107, 1942
Taylor, G. B., Govoni, F., Allen, S. W., & Fabian, A. C. 2001, MNRAS, 326, 2
Teyssier, R. 2002, A&A, 385, 337
Tonnesen, S. & Bryan, G. L. 2009, ApJ, 694, 789
Tonnesen, S. & Bryan, G. L. 2010, ApJ, 709, 1203
Tonnesen, S. & Bryan, G. L. 2012, MNRAS, 422, 1609
Tonnesen, S. & Stone, J. 2014, ApJ, 795, 148
Toomre, A. & Toomre, J. 1972, ApJ, 178, 623
Toomre A. in *Evolution of Galaxies and Stellar Populations* 1977, eds Tinsley B. M., Larson D., Campbell R. B. G. Yale University Observatory, New Haven, p.401
Tosa, M. 1994, ApJ, 426, L81
Trinchieri, G., Fabbiano, G., & Kim, D.-W. 1997, A&A, 318, 361
Tsikoudi, V. 1980, ApJS, 43, 365
Vacca, V., Murgia, M., Govoni, F., et al. 2012, A&A, 540, A38
Vallé, J. P., MacLeod, M. J., & Broten, N. W. 1986, A&A, 156, 386
Vallée, J. P., MacLeod, J. M., & Broten, N. W. 1987, Astrophys. Lett., 25, 181
Vallee, J. P. 1997, Fund. Cosmic Phys., 19, 1
Valluri, M., & Jog, C. J. 1990, ApJ, 357, 367
van den Bergh, S. 1960, ApJ, 131, 558
van den Bergh, S. 1976, ApJ, 206, 883
van den Bergh, S. 1991, PASP, 103, 390
van Gorkom, J., & Kotanyi, C. 1985, European Southern Observatory Conference and Workshop Proceedings, 20, 61
Verdes-Montenegro, L., Sulentic, J., Lisenfeld, U., et al. 2005, A&A, 436, 443
Vijayaraghavan, R. & Sarazin, C. 2017, ApJ, 848, 63
Vikhlinin, A., Forman, W., & Jones, C. 1997, ApJ, 474, L7
Vikhlinin, A., Kravtsov, A., Forman, W., et al. 2006, ApJ, 640, 691
Völk, H. J., & Xu, C. 1994, Infrared Physics and Technology, 35, 527
Vollmer, B., Marcelin, M., Amram, P., Balkowski, C., Cayatte, V. & Garrido, O. 2000, A&A, 364, 532
Vollmer, B., Cayatte, V., Balkowski, C. & Duschl, W. J. 2001, ApJ, 561, 708
Vollmer, B., Beck, R., Kenney, J. D. P. & van Gorkom, J. H. 2004, AJ, 127, 3375
Vollmer, B., Soida, M., Otmianowska-Mazur, K., Kenney, J. D., van Gorkom, J. H. & Beck, R. 2006, A&A, 453, 883
Vollmer, B., Soida, M., Beck, R., et al. 2007, A&A, 464, L37
Vollmer, B., Braine, J., Pappalardo, C. & Hily-Blant, P. 2008, A&A, 491, 455
Vollmer, B., Soida, M., Chung, A., Beck, R., Urbanik, M., Chyży, K. T., Otmianowska-Mazur, K., & van Gorkom, J. H. 2010, A&A, 512, A36
Vollmer, B., Soida, M., Beck, R., Chung, A., Urbanik, M., Chyży, K. T., Otmianowska-Mazur, K., & Kenney, J. D. 2013, A&A, 553, A116
Vulcani, B., Poggianti, B. M., Gullieuszik, M., et al. 2018, ApJ, 866, L25
Warmels, R. H. 1988, A&AS, 72, 427
Weinzirl, T., Jogee, S., Khochfar, S., Burkert, A. and Kormendy J. 2009, ApJ, 696, 411

Werner, N., Durret, F., Ohashi, T., Schindler, S. & Wiersma, R.P.C. 2008, SSRv, 134, 337
White, D. A., Jones, C., & Forman, W. 1997, MNRAS, 292, 419
Xu, C., & Sulentic, J. W. 1991, ApJ, 374, 407
Yagi, M., Yoshida, M., Komiyama, Y., Kashikawa, N., Furusawa, H., Okamura, S., Graham, A. W., Miller, N. A., Carter, D., Mobasher, B. & Jogee, S. 2010, AJ, 140, 1814
Yagi, M., Gu, L., Fujita, Y., et al. 2013, ApJ, 778, 91
Yoshida, M., Yagi, M., Komiyama, Y., Furusawa, H., Kashikawa, N., Koyama, Y., Yamanoi, H., Hattori, T. & Okamura, S. 2008, ApJ, 688, 918-930
Zasov, A. V. 1975, Soviet Ast., 18, 426
Zhang, B., Sun, M., Ji, L., Sarazin, C., Lin, X. B., Nulsen, P. E. J., Roediger, E., Donahue, M., Forman, W., Jones, C., Voit, G. M. & Kong, X. 2013, ApJ, 777, 122